JOHANNES-GUTENBERG-UNIVERSITÄT MAINZ
INSTITUT FÜR PHYSIK

Computer simulations of slowly relaxing systems in external fields

Dissertation

zur Erlangung des Grades
„Doktor der Naturwissenschaften“
am Fachbereich Physik, Mathematik und Informatik
der Johannes-Gutenberg-Universität Mainz

verfasst und vorgelegt von

David Winter

Mainz, im Juli 2012

David Winter

Computer simulations of slowly relaxing systems in external fields

——— Abstract ———

Understanding the behavior of systems in the non-equilibrium state is one of the biggest problems in contemporary physics. For these systems a formalism comparable to the one of equilibrium statistical mechanics is not known. In this work two different slowly relaxing model systems are investigated where the influence of external forces leads to a non-linear response. The first model system is a glassforming liquid where the behavior of a single particle under the influence of a constant external force is shown. In the second system the Ising model at the critical point under shear is investigated and a method is presented how the anisotropic finite-size scaling can be accomplished in this case.

In the first investigated system one of the particles in a glassforming soft-sphere mixture is pulled with a constant external force in one direction. At low temperatures close to the glass transition a strongly increased relaxation time is found and the system can easily be driven out of the linear response regime. In dependence of the magnitude of the applied force it is found that the particle behavior shows a strongly different behavior and three distinct regions can be identified. For low forces the particle is in the linear-response region where the particle properties are given by the equilibrium properties. For higher forces the particles leave that regime and enter the regime at intermediate force. In that regime the particle shows an anisotropic behavior with a superdiffusive motion in the parallel direction. Furthermore, a universal behavior is found where the particle properties can be rescaled onto the equilibrium properties with an effective temperature. At high forces it is found that the particle motion becomes isotropic and diffusive again. As a last point in this model the behavior directly after the switch on and off is investigated which helps to understand the behavior in the glass state where the system is completely frozen.

Close to the critical temperature the shear rate influences the fluctuations in the system and thus leads to an anisotropic behavior. A result of that anisotropy is that the normal finite-size scaling is not applicable anymore as two different correlation lengths appear. In this work this problem is studied in the Ising model under shear and a way is presented how the finite-size scaling can be done in that anisotropic case. Here, with the help of the structure factor a new anisotropy exponent ω can be calculated that relates the two exponents of the correlation lengths with each other. With that exponent known the relation of the two system sizes are known and the scaling can be done. Here, the critical points are measured and they are shifted in dependence of the shear rate. Furthermore the critical exponents $\beta, \gamma, \nu_{\parallel}$ and $\nu_{\perp}$ are calculated.

David Winter

Computersimulationen von langsam relaxierenden Systemen in externen Feldern

——— Zusammenfassung ———

Eine der offenen Fragen der aktuellen Physik ist das Verständnis von Systemen im Nichtgleichgewicht. Im Gegensatz zu der Gleichgewichtsphysik ist in diesem Bereich aktuell kein Formalismus bekannt der ein systematisches Beschreiben der unterschiedlichen Systeme ermöglicht. Um das Verständnis über diese Systeme zu vergrößern werden in dieser Arbeit zwei unterschiedliche Systeme studiert, die unter einem externen Feld ein starkes nichtlineares Verhalten zeigen. Hierbei handelt es sich zum einen um das Verhalten von Teilchen unter dem Einfluss einer extern angelegten Kraft und zum anderen um das Verhalten eines Systems in der Nähe des kritischen Punktes unter Scherung.

Das Modellsystem in dem ersten Teil der Arbeit ist eine binäre Yukawa Mischung, die bei tiefen Temperaturen einen Glassübergang zeigt. Dies führt zu einer stark ansteigenden Relaxationszeit des Systems, so dass man auch bei kleinen Kräften relativ schnell ein nichtlineares Verhalten beobachtet. In Abhängigkeit der angelegten konstanten Kraft können in dieser Arbeit drei Regime, mit stark unterschiedlichem Teilchenverhalten, identifiziert werden. Bei kleinen Kräften findet sich der linear-e-Antwort Bereich, in dem das Teilchenverhalten durch die Gleichgewichtseigenschaften gegeben ist. Bei mittleren Kräften werden darüber hinaus nichtlineare Effekte sichtbar und es wird beobachtet, dass die Teilchenbewegung in Zugrichtung superdiffusiv ist. Daneben lassen sich die Eigenschaften der Teilchen durch ein universelles Verhalten mit einer effektive Temperatur beschreiben. Zu höheren Kräften hin beobachtet man einen Übergang in ein weiteres Regime. Hier verringert sich die Anisotropie der Teilchenbewegung und sie wird wieder vollständig diffusiv. Als letzter Punkt in diesem System wird das Verhalten des Teilchens direkt nach dem An- und Abschalten der Kraft untersucht welches Aufschluss über die Teilchenbewegung bei tieferen Temperaturen in der Glassphase gibt.

In dem zweiten Teil der Arbeit wird das Ising-Modell unter Scherung betrachtet. In der Nähe des kritischen Punkts kommt es in diesem Modell zu einer Beeinflussung der Fluktuationen in dem System durch das angelegte Scherfeld. Dies hat zur Folge, dass das System stark anisotrop wird und man zwei unterschiedliche Korrelationslängen vorfindet, die mit unterschiedlichen Exponenten divergieren. Infolgedessen lässt sich der normale isotrope Formalismus des ”finite-size scaling” nicht mehr auf dieses System anwenden. In dieser Arbeit wird gezeigt, wie dieser auf den anisotropen Fall zu verallgemeinern ist und wie damit die kritischen Punkte, sowie die dazu gehörenden kritischen Exponenten berechnet werden können.

Publications:

Parts of this work have already been published in the following references:

D. Winter, P. Virnau, J. Horbach and K. Binder
Finite-size scaling analysis of the anisotropic critical behavior of the two-dimensional Ising model under shear
Europhys. Lett. **91**, 60002 (2010).

D. Winter, J. Horbach, P. Virnau and K. Binder
Active nonlinear microrheology in a glass-forming Yukawa fluid
Phys. Rev. Lett. **108**, 028303 (2012).

C. Harrer, D. Winter, J. Horbach, M. Fuchs and T. Voigtmann,
Force-induced diffusion in microrheology
J. Phys.: Condens. Matter **24** (2012) accepted.

Publication in preparation:

D. Winter and J. Horbach
Universal scaling and effective temperature in nonlinear microrheology
in preparation (2012).

Publications from the Diploma thesis:

M. Schrader, P. Virnau, D. Winter, T. Zykova-Timan and K. Binder,
Methods to extract interfacial free energies of flat and curved interfaces from computer simulations
Eur. Phys. J. ST **177**, 103 (2009).

D. Winter, P. Virnau and K. Binder
Monte Carlo test of the classical theory for heterogeneous nucleation barriers.
Phys. Rev. Lett. **103**, 225703 (2009).

D. Winter, P. Virnau and K. Binder
Heterogeneous nucleation at a wall near a wetting transition: a Monte Carlo test of the classical theory
J. Phys.: Condens. Matter **21**, 464118 (2009).

K. Binder, B. Block, S. K. Das, P. Virnau and D. Winter
Monte Carlo Methods for Estimating Interfacial Free Energies and Line Tensions
J. Stat. Phys. **144**, 690 (2011).

Contents

Chapter 1

Introduction

The description of systems far away from equilibrium is one of the major challenges of contemporary physics. Since the understanding of the equilibrium systems around 100 years ago relatively slow progress has been made in that direction. Until now, only the linear-response regime is understood that describes small perturbations from the equilibrium behavior which breaks down for higher forces. At present no framework is available that describes systems in that regime. Therefore, it is of great interest to study slowly relaxing systems under the influence of external forces that can easily be driven into the non-linear response regime. In this work two different problems are investigated that show a strongly non-linear response and are of interest in the field of colloidal physics.

Fluid colloidal systems are often used systems in the study of soft matter physics [1, 2] which contain particles in the range from nanometer to micrometer size dispersed in a solvent. Well known examples of every day colloidal materials are blood, dust, milk, paint, ketchup and many more. From the experimental side these systems are interesting as they have a few advantages compared to atomistic systems. Due to the big size of the particles they are much easier accessible. Colloidal systems can be investigated with techniques that use optical light such as confocal microscopy or light scattering whereas in the case of atomistic systems much higher energies are required that lead to a bigger often not feasible effort. A second advantage are the much slower timescales involved in these systems. For colloidal systems a typical relaxation time is in the region of milliseconds or larger whereas for atomic systems it is in the range of picoseconds which complicates the investigations even more. A further big advantage of colloidal systems is the ability to tune the particle potentials. For example by varying the concentration of polymers or salt in a solution the attraction between the charged colloids can be changed. Thus, one can study the influence of certain parts of the potentials much easier and these systems can even be used as models for atomic systems [3]. One characteristic property of colloidal mixtures is that they exhibit Brownian motion which is a consequence of the solvent that leads to many collisions with the

colloidal particles and thus to a random motion.

One subfield that deals with the mechanical properties of condensed systems is the rheology [4]. There, the flow of complex liquids and deformations of soft solids under the influence of external forces is investigated. A typical (macro) rheological experiment is the shear experiment where the system is bound between two plates that are moved into opposing directions. First, this leads to a deformation and then to a flow of the whole system. This can and has been done for colloidal systems [5] where the influence and the behavior of the shear rate on the system properties can be measured. Here, interesting occurring phenomena are the effects of shear thinning or shear thickening which lead to a decreasing or increasing viscosity with increasing shear rate [6].

In recent years a newly developed method called microrheology came into the focus of the research [7, 8] as it allows to extract additional information about a system and extends the macro rheological measurements. There, the behavior of single probe particles embedded in the material is measured with the aim to receive informations about the system that are not accessible with the macro rheological experiments. In principal this method can be applied in two different versions. In the passive version the probe particles are left unperturbed inside the material. There, the formalism of equilibrium mechanics still holds and thus with the Stokes-Einstein relation the relation between the probe properties and the system properties are known and understood. The second version is the active version where an external force is applied on the probe particle. As a consequence the probe accelerates and moves in the direction of the force [9, 10, 11, 12]. Experimentally this can be done with probe particles that are pulled with magnetic fields [13] or laser tweezers [14, 15, 16]. For strong enough forces the linear-response regime [17] is left and the behavior gets non-linear. Here, no simple formalism exists that describes the non-linear behavior of the particle [18] and therefore this regime is still not well understood.

In the first part the behavior of a pulled particle in a glassforming soft-sphere mixture is investigated which is for two reasons an interesting problem to study. At low temperatures close to the glass transition one observes a strongly increased relaxation times. As a consequence one can easily drive the system out of the linear-response regime and thus study occurring non-linear effects. This is of interest in the field of microrheology where one needs to understand the non-linear behavior of the probe particles. Therefore, the aim of this work is to identify and investigate the different occurring regimes in dependence of the temperature and force parameter. Furthermore, the differences in the behavior of the particles between the liquid and the glass phase are of interest which leads to the second motivation from the side of the theoretical description of the glass transition. The glass transition is a topic that has been studied for a long time and multiple different theories have been developed to describe the appearing effects [19, 20, 21]. For example one has the theory of Adam and Gibbs [22], the free volume theory [23], kinetically constrained models [24] and the mode coupling theory of the glass transition (MCT) [25, 26]. Thus, it is interesting to study the behavior of

a pulled particle in a supercooled liquid and to compare the results with the theoretical predictions that can be made.

The second part of this work deals with a problem of anisotropic finite-size scaling in computer simulations at the critical point. This is a problem that appeared in previous simulation where the Asakura-Oosawa (AO) model [27] under shear was investigated [5, 28]. As is well known, the AO model describes colloid-polymer mixtures which undergo phase separation in a polymer-rich phase and a colloid-rich phase. Here, the critical point where these phases become indistinguishable belongs to the universality class of the Ising model. For the behavior of a liquid system under shear a few predictions are made [29, 30, 31] such as a shifted critical point, an anisotropic critical behavior with different critical exponents and a reduction of the capillary waves. These points are of interest to study in a computer simulation but unfortunately they are strongly complicated by the occurring anisotropy and finite-size effects caused by the applied shear in the region around the critical point. Thus, one can only make progress in the understanding if the behavior is understood and it is known how these systems can be treated in computer simulations. As this problem is too difficult to solve and to understand in a Molecular dynamics simulation of a continuous model a much simpler model, the sheared two dimensional Ising model, is chosen here. Close to the critical point the fluctuations in this system are also strongly anisotropic and the finite-size scaling can be studied. Here, it is shown that an anisotropic scaling is required where the different system sizes are scaled with an anisotropy exponent. That scaling exponent is crucial for the whole ansatz and it is found that it can be obtained from the static structure factor. With the help of this exponent the critical points and the corresponding critical exponents can be studied. Thus, a methodology has been developed how criticality can be studied when Ising-like systems are exposed to shear. It is hoped that this methodology will be a useful ingredient in future studies of phase separation in Ising-like systems such as colloid-polymer mixtures under shear.

This work is organized in the following way. In the second chapter an introduction to the soft sphere Yukawa system and the simulation details is given. The third chapter is a short overview of the important theoretical models that describe the behavior of the pulled particles. In the fourth chapter the characteristic properties of the pulled probe in the steady state are presented where three different regimes can be identified. In chapter five the regime at intermediate forces and in chapter six the regime at high force are investigated in detail. In chapter seven the behavior of the probe at the switch on, the switch off and in the glass is presented which is the last chapter on the topic of microrheology. Then, chapter eight treats the anisotropic finite-size scaling of the Ising model under shear.

Chapter 2

Molecular dynamics simulation and the model

In the study of classical many-body systems two simulation methods are widely employed. The first is the classical Monte Carlo method [32] which is often used in the study of equilibrium systems. There, one has access to the powerful formalism of equilibrium ensembles that allows for advanced sampling steps. Additionally it can be used in some cases for systems if the information about the microscopic dynamics is not required and the average state of the system is not much influenced by the microscopic dynamics and the chosen sampling algorithm. The second popular method is called Molecular dynamics [32, 33]. There, one integrates the equations of motion on a per particle base and therefore contains the information about the microscopic dynamics. As a consequence this method has the clear disadvantage that it is rather slow for typical system sizes and it is quite a challenge to simulate slowly relaxing processes. Here, in this work it is the aim to study the microscopic behavior of a pulled particle with the correct dynamical properties and therefore the Molecular Dynamics simulation method is chosen which is presented in the following. The basic equations that describe the behavior of classical many-particle systems are Newton's equations of motion,

$$m_i \ddot{\mathbf{r}}_i = \mathbf{F}_i = \sum_{j(\neq i)} \mathbf{F}_{ij} = -\sum_{j(\neq i)} \nabla V(|\mathbf{r}_i - \mathbf{r}_j|). \tag{2.1}$$

For a system that contains N particles one obtains $3N$ coupled differential equations of second order. Together they describe the motion of the particles interacting by a given potential $V(r)$. Here, m_i is the mass, $\mathbf{r}_i$ the position and $\ddot{\mathbf{r}}_i$ the acceleration of the i-th particle. This interaction potential $V(r)$ leads to a force $\mathbf{F}_{ij} = -\nabla V(|\mathbf{r}_i - \mathbf{r}_j|)$ acting between particles i and j.

2.1 Velocity-Verlet-algorithm

Quite a few different integration schemes have been used to solve the equations of motions (2.1). They differ in many properties as the required resource consumption during the simulation, the speed, the complexity of the algorithm, the precision of the calculated particle trajectories or the energy conservation of the whole system. For the calculation of many-particle systems the Verlet integration scheme [34, 35, 36] is often used. It is a symplectic algorithm and therefore conserves the energy of the system even over long simulation runs and it is time reversible [37]. In addition, it is in a low order of time and therefore very compact and simple to program. In this work an extended version of the Verlet integration scheme is used, the velocity Verlet version [38]. Here, new positions $\mathbf{r}_i(t+\delta t)$ and velocities $\mathbf{v}_i(t+\delta t)$ are given by

$$\begin{aligned} \mathbf{r}_i(t+\delta t) &= \mathbf{r}_i(t) + \delta t \mathbf{v}_i(t) + \frac{\delta t^2}{2m_i}\mathbf{F}_i(t) \\ \mathbf{v}_i(t+\delta t) &= \mathbf{v}_i(t) + \frac{1}{2m_i}[\mathbf{F}_i(t) + \mathbf{F}_i(t+\delta t)], \end{aligned} \tag{2.2}$$

with δt the chosen time step. This scheme is implemented in a two step way with the force calculation in between. In the first integration step one calculates the new particle positions from the old values and adds $\mathbf{F}_i(t)/2m_i$ to the velocities. After this step the new forces can be calculated from the new particle positions. In the second and last integration step the velocity calculation is completed by adding $\mathbf{F}_i(t+\delta t)/2m_i$ to the previous values. Now, the system has propagated by a time step δt and all system properties of interest can then be measured.

Compared to the original integration scheme this implementation has the advantage that it makes all particle positions, velocities and forces accessible at the same time t. Whereas in the original version [34] the velocities at time t can only be calculated with the knowledge of the positions at time $t+\delta t$ and $t-\delta t$ and therefore its use is a bit cumbersome.

2.2 DPD-thermostat

In this work one of the particles in the system shall be pulled through the system by an external force. This additional force constantly increases the energy of the system. As a consequence it will heat up. The aim of this work is to study the steady state of the pulled particle with a surrounding medium at a constant temperature and not in a system with an increasing temperature over time. Therefore, it is required to reduce the whole energy of the system by the amount that is brought into the system during the simulation. In this work the temperature and not the energy shall be

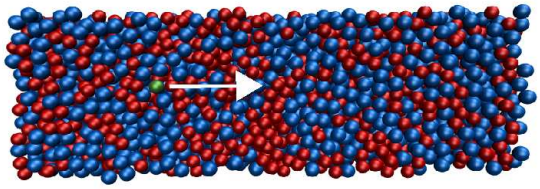

Figure 2.1 – A typical configuration of the system. The green particle highlights the single pulled particle inside the bath of A and B particles (red and blue). The white arrow gives the direction of the externally applied force.

preserved. This can be realized by coupling the system to a thermostat. Due to the external force that works on the probe particle it is required that this thermostat also conserves momentum locally and not only globally. Therefore, the thermostat should also be Galilean invariant.

The thermostat of choice, that fulfills all these requirements, is an improved dissipative particle dynamics (DPD) thermostat [39, 40, 41]. There, the equations of motion of the particles are varied in the following way

$$m_i \ddot{\mathbf{r}}_i = \mathbf{F}_i = \sum_{j(\neq i)} [\mathbf{F}_{ij} + \mathbf{F}_{ij}^D + \mathbf{F}_{ij}^R] + \mathbf{F}_i^{ext}. \tag{2.3}$$

Originally DPD was used as a method to study hydrodynamic effects as they can be strongly increased with this method. In this equation the original calculation of the forces (three terms in brackets) was extended by the external force contribution $\mathbf{F}_i^{ext}$. This force acts at one selected particle which shall be pulled through the system. For all other particles this force is zero. Beside the first contribution to the forces from (2.1), two additional contributions $\mathbf{F}_{ij}^D$ and $\mathbf{F}_{ij}^R$ act on the particle pairs. These are the contributions from the DPD thermostat [39, 40] and are given by

$$\mathbf{F}_{ij}^D = -\zeta\omega^2(r_{ij})(\hat{\mathbf{r}}_{ij} \cdot \mathbf{v}_{ij})\hat{\mathbf{r}}_{ij} \tag{2.4}$$

and

$$\mathbf{F}_{ij}^R = \sqrt{2k_B T\zeta}\,\omega(r_{ij})\theta_{ij}\hat{\mathbf{r}}_{ij}, \tag{2.5}$$

with $\mathbf{r}_{ij} = \mathbf{r}_i - \mathbf{r}_j$ and $\mathbf{v}_{ij} = \mathbf{v}_i - \mathbf{v}_j$ the relative distances and velocities, $\hat{\mathbf{r}}_{ij} = \mathbf{r}_{ij}/|\mathbf{r}_{ij}|$ the corresponding unit vector and ζ a parameter that sets the strength of the first interaction. Note, that the prefactors in (2.4) and (2.5) are determined by the fluctuation dissipation relation as was shown in [40]. The function $\omega(r_{ij})$ is a weight function which can be used to tune the strength of the DPD interactions in dependence of the relative particle distance. The following choice

$$\omega(r_{ij}) = \sqrt{1 - r_{ij}/r_{\mathrm{DPD}}^c}. \tag{2.6}$$

for $r < r^c_{\mathrm{DPD}}$ (and zero otherwise) is the standard choice for the use of soft potentials but generally a different function could also be used [42]. Here, r^c_{DPD} is a second free parameter that sets the range of the DPD interactions. The function θ_{ij} is a Gaussian white noise term with

$$\begin{aligned} \langle \theta_{ij}(t) \rangle &= 0, \\ \langle \theta_{ij}(t)\theta_{i'j'}(t') \rangle &= (\delta_{ii'}\delta_{jj'} + \delta_{ij'}\delta_{ji'})\delta(t-t'). \end{aligned} \tag{2.7}$$

The first term of the DPD interactions $\mathbf{F}^D_{ij}$ (2.4) is a friction term. It is negative and couples to the relative velocities of the particle pairs. This part leads to a decrease of the relative motion and therefore to a cooling of the system. The second term $\mathbf{F}^R_{ij}$ is a random force that leads to an acceleration of the slow particles. The consequence of these two terms is that the system energy is bound from both sides. Together they manage to keep the temperature of the system constant, even under the influence of external forces [5]. Both parts of the thermostat only act on particle pairs and therefore the thermostat works locally that is an important property for the simulation of system with external forces. Generally these forces are anisotropic and therefore a requirement for the thermostat is that it is able to manage these directed forces and does not create any unwanted anisotropic effects. An example for such a force is the shear field where the system shows a strong anisotropic behavior as can be seen in [5]. There, the DPD thermostat has proven to be a good working choice and managed to cool the system even with such strong directed forces. By changing the parameters r^c_{DPD} and ζ the range and the strength of the interaction can be tuned. The parameter ζ sets the strength of the thermostat and therefore controls how strong the Newtonian motion of the particles is disturbed by the thermostat. The radius r^c_{DPD} on the other hand tunes how long ranged the interactions of the thermostat are. By choosing $\omega^2(r_{ij})$ as a prefactor for $\mathbf{F}^D_{ij}$ and $\omega(r_{ij})$ for $\mathbf{F}^R_{ij}$ the fluctuation-dissipation theorem is automatically fulfilled [40].

2.2.1 Peters scheme

The equations (2.4) and (2.5) can be implemented in different ways. In earlier realizations of this thermostat the problem occurred that they were not time step independent and did not rigorously maintain the Maxwell-Boltzmann distribution. This was caused by the random force term (2.5) which was independent of the chosen time step δt. There, a different time step changes only the friction term of the thermostat and therefore leads to a different behavior. That problem was solved by a new integration scheme which was proposed by Peters [41] which is used in this work. According to this scheme the momenta of the particles have to be rescaled after the velocity Verlet

integration step by

$$\begin{aligned}\mathbf{p}_i &:= \mathbf{p}_i + (-a_{ij}(\mathbf{v}_{ij}\cdot\hat{\mathbf{r}}_{ij})\delta t + b_{ij}\theta_{ij})\hat{\mathbf{r}}_{ij}\\ \mathbf{p}_i &:= \mathbf{p}_i - (-a_{ij}(\mathbf{v}_{ij}\cdot\hat{\mathbf{r}}_{ij})\delta t + b_{ij}\theta_{ij})\hat{\mathbf{r}}_{ij}.\end{aligned} \tag{2.8}$$

Here, prefactors a_{ij} and b_{ij} are chosen as

$$\begin{aligned}a_{ij} &= \zeta\omega^2(r_{ij})\\ b_{ij} &= \sqrt{2kT\zeta\omega^2(r_{ij})\left(1-\frac{\zeta\omega^2(r_{ij})\delta t}{2\mu_{ij}}\right)},\end{aligned} \tag{2.9}$$

with $\mu_{ij} = (1/m_i + 1/m_j)^{-1}$ the reduced mass of the particles i and j. This choice corresponds to scheme 1, as proposed in the publication by Peters. This realization of the DPD thermostat differs from earlier implementations in the time step dependence of b_{ij}. Therefore, changing here the value of the time step also changes the effect of the random force term and thus leads to a time step independent behavior.

2.3 Neighbor list

To speed up the simulations neighbor lists of the particles are used [34, 35]. Each particle in the system has two lists of surrounding neighbors, one for each particle type. Here, surrounding means closer than a given cutoff radius r^{nlist}. The advantage of these lists is that the number of particles that are considered in the force calculation is reduced strongly. Without these lists all interactions between every single particle pair have to be calculated. This would lead to a scaling of the computational load $\propto N^2$. With the use of neighbor lists the effort can be reduced to a scaling $\propto N$. This is a drastic difference for systems with many particles. The cutoff radius of these neighbor lists r^{nlist} is given by the cutoff radius of the pair potential $r^c_{\alpha\beta}$ and an additional skin size $r^{\text{nlist}} = r^c_{\alpha\beta} + r^{\text{skin}}$ (fig. 2.2). By that choice the cutoff radius is always bigger than the interaction potential in the simulations. The skin size r^{skin} gives an additional buffer that prevents an update of the neighbor list after a particle has moved further than the interaction potential. By an appropriate choice of this size an additional speed gain is possible. In this work two slightly different implementations of neighbor lists are used.

Classical Verlet neighbor list Implementation of the original proposed version [34]. Here, all particle neighbor lists are refreshed at the same time if one of the particles moves further than $r^{\text{skin}}/2$. This leads to an effort $\propto N^2$ for the update step (all particle pairs have to be checked). If the displacements of all the

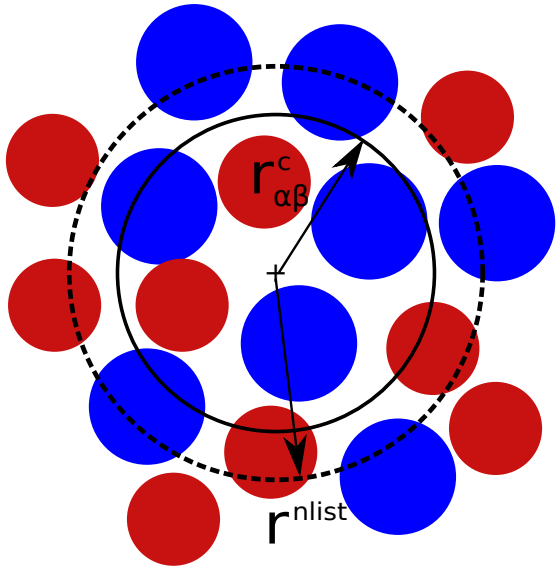

Figure 2.2 – Sketch of the neighbor list radii. The radius of the neighbor list r^{nlist} is the sum of the potential cutoff radius $r^c_{\alpha\beta}$ and a skin size r^{skin}.

particle are smaller than r^{nlist} no change at all on the list is done and therefore the effort is zero. The important parameter for the neighbor list is r^{skin} as it defines how often the whole list is updated and therefore how big the speed gain is. If this parameter is to small the list is updated to often and therefore one looses efficiency. On the other hand if that parameter is too big one has too many particles in the list and then too many forces inside the force calculation are computed.

Incremental Verlet neighbor list During the implementation it was found, that one can speed up the simulation even more by incrementally updating the neighbor list. Then, only the lists of the particles are updated that move further than $r^{\text{skin}}/2$. Additionally all the lists of the neighbor particles of these particles need to be updated. This leads to an effort that is proportional to N and reduces the work even more. A second advantage of this incremental updating is, that the skin size r^{skin} can be reduced quite a bit. As a consequence fewer particles are in each neighbor list. It is found, that this second type of neighbor list speeds up the simulation by $10-20\%$ but this speed gain comes at the cost of a more complex neighbor list code. With the help of advanced classes in c++ as the vector class that allow complex transformations of the neighbor list arrays this incremental version could be realized. One problem here is, that this implementation is not thread safe (cannot be used with multiple threads simultaneously which is required for a parallelization) and therefore it cannot be used together with a simple parallelization program called Openmp. Thus, during the equilibration phase, where Openmp is required to speed up the simulation, the classical Verlet

list had to be used.

Before the simulation runs were performed it was intensively checked, that both implementations lead to exactly the same numerical results and both list types were properly implemented. In this work both types of lists were used. The classical version was used during the long equilibration runs at the beginning to create the starting configurations. With an Openmp parallelization the equilibration time could be reduced by a factor of 6 on 8 cores. Later on during the measurements with the pulled particles, the incremental version was used. These runs are much shorter compared to the equilibration runs and therefore it is more efficient to use a trivial parallelization. There, one runs a copy of the system on every single core and just pulls a different particle of the same type. Here, the faster incremental version can be used.

2.4 Model and simulation details

The investigated model in the first part of this work is a binary soft sphere mixture. It contains two different particle types A and B that interact through a Yukawa potential which is an often used potential for describing colloidal systems. According to the Derjaguin-Landau-Verweij-Overbeek (DLVO) theory [2] this potential is obtained if charged colloidal particles are screened in a solution. Here, the counterions prevent parts of the coulomb interaction between the charged colloids and lead to a screened behavior. A further advantage is that it has been intensively investigated in previous works and the behavior in the equilibrium and under shear are known [5, 43, 44] and can be used as a reference point. The resulting screened potential is of the following type

$$V_{\alpha\beta}(r) = \varepsilon_{\alpha\beta} d_{\alpha\beta} \exp[-\kappa(r - d_{\alpha\beta})]/r. \tag{2.10}$$

Here, α and β stand for the different types of particles that are separated by a distance r. The general system properties are defined through the constant values $\varepsilon_{\alpha\beta}$, $d_{\alpha\beta}$, κ and m_α in the potential function. Here, $\varepsilon_{\alpha\beta}$ sets the energy scale, $d_{\alpha\beta}$ the length scale and m_α the scale of the masses. The inverse screening length κ is measured in units of $1/\sigma_{AA}$. With these parameters one can define the characteristic units $\sqrt{m_A d_{AA}^2/\varepsilon_{AA}}$ for the time t, ε_{AA}/k_B for the temperature T and ε_{AA}/d_{AA} for the force f, with k_B the Boltzmann constant. The potential $V_{\alpha\beta}(r)$ is truncated at a cut-off radius $r^c_{\alpha\beta}$. Here, $r^c_{\alpha\beta}$ is chosen as

$$V_{\alpha\beta}(r = r^c_{\alpha\beta}) = 10^{-7}. \tag{2.11}$$

To prevent fluctuations in the energy when particles move over this cut-off radius, the potential in the simulation is shifted by the value at $r^c_{\alpha\beta}$. The implemented potential is therefore

$$\tilde{V}_{\alpha\beta}(r) = V_{\alpha\beta}(r) - V_{\alpha\beta}(r^c_{\alpha\beta}). \tag{2.12}$$

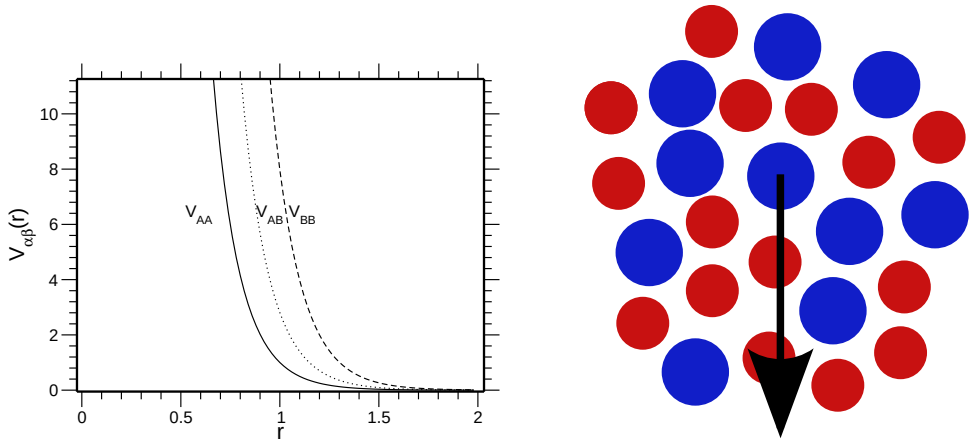

Figure 2.3 – Left) The behavior of the inter particle potential $V_{\alpha\beta}$ in dependence of r and the particle types as given in (2.10).

Technical simulation details

System properties As the obtained results in this work shall be comparable with the previous works the values of the particle potentials need to be the same. Therefore, the chosen masses of both particle types are equal and set to unity $m_A = m_B = 1$. The inverse Debye screening length is $\kappa = 6$ and the chosen time step is $\delta t = 0.0083$. With this time step the equations of motion could be integrated without problems in the previous works, even under shear. The other values of $\varepsilon_{\alpha\beta}$, $d_{\alpha\beta}$ and $r^c_{\alpha\beta}$ depend on the type of particle and are summarized in table 2.1.

With these settings two different system geometries with periodic boundary conditions are set up. A cubic one with size $L_x = L_y = L_z = 13.3 = L$ and 1600 particles with 800 A and 800 B particles. The second system geometry is 8 times larger in the x-direction and thus allows longer simulation runs at higher forces without moving the pulled particle multiple times trough the same box. The second geometry is $L_x = 8L$, $L_y = L_z = L$ with 12800 particles (6400 of each type). Both configurations have the same particle density $\rho = \frac{N}{V} = 0.68$. At the borders of these boxes periodic boundary conditions are applied that link opposing sides of the box with each other. Particles

type $\alpha\beta$	range $d_{\alpha\beta}$	energy $\varepsilon_{\alpha\beta}$	cutoff radius $r^c_{\alpha\beta}$
AA	1.0	1.0	3.48
AB	1.1	1.4	3.64
BB	1.2	2.0	3.81

Table 2.1 – Values of the potential parameters in dependence of the particle types

that leave the box through one of the system sides enter the system at the opposing side again. These boundary conditions prevent effects from hard walls at the end of the simulation box. During the calculation of the forces the minimum image convention is adopted and therefore only forces between the nearest positions of the particles are calculated.

In this work one of the particles is pulled through the system. This requires an additional external force f that acts on the selected particle. In all presented simulations that external force always directs into the positive x-direction with a constant strength during the whole simulation run. To study the dependence on the strength, $|\mathbf{F}_i^{ext}| = f$ is varied in the range $0.5 \leq f \leq 30$. This external force is not only a source of energy that needs to be taken out by the thermostat, but also a source of momenta. Due to the present periodic boundary conditions that would lead to an acceleration of the whole system over time. This effect is quite unpleasant in the later analysis of the particle motion. Therefore, this acceleration is prevented by subtracting the average directed velocity of the system from all particles after each time step. Then the system is again at rest.

Properties of the neighbor list For the classical Verlet list the skin size is chosen as $r^{\text{skin}} = 0.75$ [5]. On average this leads to an update of the whole list every 38 integration steps at the lowest equilibrium temperature $T = 0.14$. For the incremental Verlet list it is found that at the same temperature the skin size could be reduced to $r^{\text{skin}} = 0.5$.

Equilibration of the system Before the measurement runs can be started the system has to be equilibrated. Therefore, up to 100 random configurations with cubic shape $L_x = L$ and 20 with elongated shape $L_x = 8L$ have been prepared at each temperature. These initial configurations were cooled down to the required temperature. The required time for these equilibration runs can be taken from [5]. It is the time when for a given temperature the incoherent scattering function (fig. 2.5) has decayed to zero. At the lowest temperature $T = 0.14$ this can take up to 50 million integration steps. In addition to these equilibrium configurations some configurations in the glass state were prepared. Therefore, the equilibrated configurations at $T = 0.14$ were used and quenched to the lower temperatures $T = 0.10$ and $T = 0.05$. This last step was done over 2 million time steps.

To speed up the equilibration of the system, the DPD-thermostat was not used in this case as it slows down the dynamics. Instead the Andersen thermostat was used [45]. There, every 10 time steps the velocities of the particles were drawn completely new from a Maxwell-Boltzmann distribution. This thermostat destroys the correlations in the system faster and hence leads to a faster relaxation.

Properties of the DPD thermostat The DPD thermostat has two free parameters ζ and r_{DPD}^c that can be tuned. Here, r_{DPD}^c sets the range of the DPD interaction and ζ the strength of the thermostat. For low values of ζ the conservative forces from the

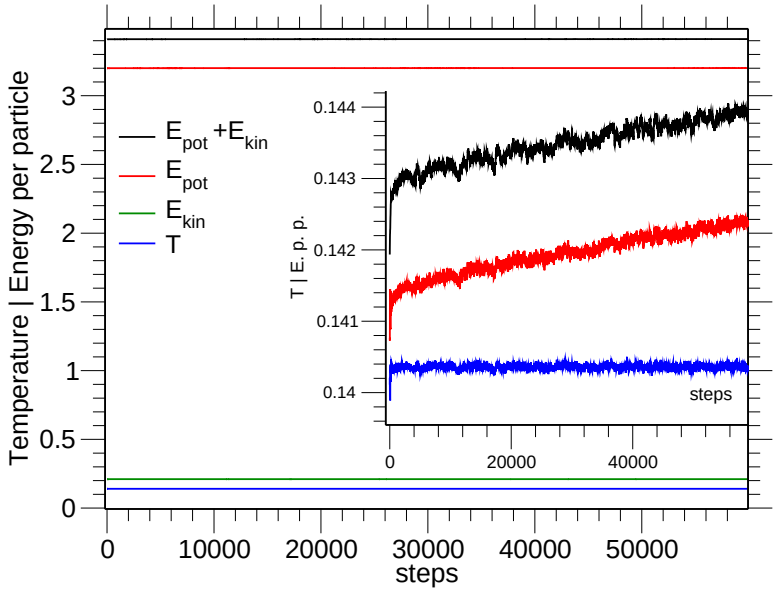

Figure 2.4 – Behavior of the energies per particle and the temperature in the system with a pulled particle. Shown system is at $T = 0.14$ and $f = 5$ for a pulled A particle. The inset shows the same curve for the temperature (not shifted) and shifted curves for the energies. Here, the whole system energy was shifted by 3.268 and the potential energy by 3.059 to fit in the same inset.

potentials dominate and one obtains a dynamic that is close to the Newtonian case. For high values of ζ the dynamics goes over to a Brownian motion. As in previous works [5, 43, 44] $\zeta = 12$ and $r^c_{\mathrm{DPD}} = 1.25$ are chosen. These choices give a dynamics that is close to the Newtonian behavior.

As this thermostat has already been successfully used in a previous study in the same system under shear, one can expect that it is also able to handle one single pulled particle with an external force. In fig. 2.4 the temperature (blue curve) and the energy behavior (other curves) for a simulation with a pulled A particle at $T = 0.14$ and $f = 5$ are shown. One sees that the thermostat manages to keep the temperature constant over the whole simulation time. Only in the strongly increased inset a small jump at the beginning can be seen. This jump results from the increased average kinetic energy in the system when the particle is pulled. In the case of the potential energy, the behavior is different. There, one observes a constant increase of the energy over the whole simulation run. This is a result of the increased disorder that is introduced in the system by the motion of the particle. At these low temperatures the relaxation time is too large to restore the lowest energy state of the equilibrium configuration and therefore the system is locally, in the region behind the particle, in a higher energy state. This leads to a steady increase of the potential energy.

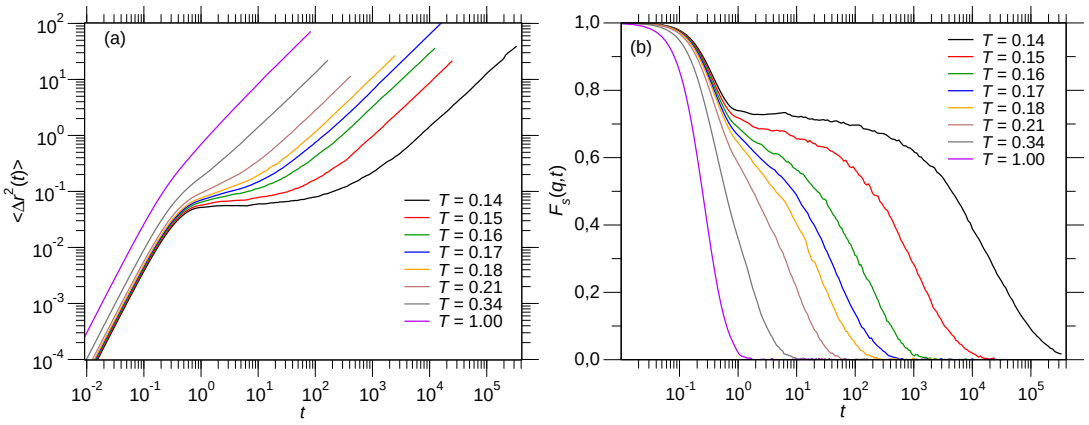

Figure 2.5 – Properties of the equilibrium system. Left plot shows mean-squared displacements $\langle \Delta r^2(t) \rangle = \langle |\mathbf{r}(t) - \mathbf{r}(0)|^2 \rangle$ and right incoherent scattering function $F_s(q,t) = \langle \exp\left(-i\mathbf{q} \cdot [\mathbf{r}(t) - \mathbf{r}(0)]\right) \rangle$ for $q = 6.0$ of A particles in dependence of the time for different temperatures. These curves were measured in a previous work by Jochen Zausch [5].

System properties in equilibrium

The equilibrium properties of this Yukawa system (2.10) are already known from previous work [5]. Therefore, the important properties of the system are summarized here quite shortly and only the important parts that are required for the understanding of this work. A complete discussion can be found in the original work of Jochen Zausch [5]. Note, the equilibrium data that is shown in this work and often used as a reference point is the original data and was not calculated again.

For this system it is found that it shows the typical behavior of a glassforming binary mixture. Above a critical temperature T_c the system is ergodic and in a fluid equilibrium phase, where on the time scales of the simulation and for the investigated temperatures no crystallization or phase separation was observed. Closer to the critical temperature one finds a strong increase of the relaxation time and of the system viscosity and a decrease of the diffusion over orders of magnitude. From the power law behavior of these properties which is predicted by the mode-coupling theory the critical temperature can be identified around $T_c = 0.14$. For temperatures below T_c the system freezes and the particle diffusion and relaxation is prevented on timescales accessible in the simulation. This is the transition to the glass state.

Fig. 2.5 shows the equilibrium curves for the mean-squared displacement

$$\left\langle \Delta r^2(t) \right\rangle = \left\langle |\mathbf{r}(t) - \mathbf{r}(0)|^2 \right\rangle \tag{2.13}$$

and the incoherent scattering function

$$F_s(q,t) = \left\langle \exp\left(-i\mathbf{q}\cdot[\mathbf{r}(t)-\mathbf{r}(0)]\right)\right\rangle \tag{2.14}$$

(with $q = 6.0$) for different temperatures T in dependence of the time t. As one can see, both curves show a strongly decreased motion by orders of magnitude at the lower temperatures. Furthermore, a pronounced plateau appears that is stretched over decades in time for the lowest temperature and indicates the glass transition. During these plateau regions the particles are trapped inside the cage of the surrounding particles and only for longer times the particles are able to leave their cages, to diffuse and relax. This second relaxation step can be divided into two different regimes. The behavior shortly after the plateau where the behavior can be described by the "von Schweidler law" that is presented in the next chapter. For the late times the behavior can be approximated by a stretched exponential function. Below T_c one observes a freezing of the system, the plateaus are stretched over the whole simulation time and the last relaxation step is missing.

Chapter 3

Theoretical models

Systems in their supercooled state show some unusual properties [19, 46]. In their liquid state the usual relaxation time τ and viscosity η are rather small in the range of picoseconds and 10^{-3} Poise. By cooling these system down to temperatures below their melting temperature T_m it is found that the values of these properties increase strongly by orders of magnitude. This can be seen in fig. 3.1 where an Angell-plot for different materials is shown. There, the viscosities are plotted against T_g/T with T_g the temperature where the viscosity of the corresponding system has reached the value of 10^{13} Poise. Here, the values of η increase by over 15 decades in a relatively small temperature window. That behavior of the dynamical quantities is in contrast to the behavior of structural quantities as well as of thermodynamic properties of the system that only show a relatively weak temperature dependence. This for example can be seen in the heat capacity C which is displayed in the inset of fig. 3.1. Empirically it is found that the behavior of the viscosities can be described by the Vogel-Fulcher(-Tammann)-law [47, 48, 49]

$$\eta(T) = \eta_0 \exp\left(A/(T - T_0)\right), \tag{3.1}$$

that has a divergence at T_0. In the study of supercooled liquids the correlation function $F(q,t)$ of the density fluctuations $\rho_{\mathbf{q}}(t) = \sum_{i=1}^{N} \exp\left(i\mathbf{q} \cdot \mathbf{r}_i(t)\right)$ is an often studied property. It has the advantage that it is accessible from the experimental side as well as from the theoretical side and contains the full time development of the particle behavior,

$$F(q,t) = \frac{1}{N}\langle \rho^*_{\mathbf{q}}(t)\rho_{\mathbf{q}}(0)\rangle. \tag{3.2}$$

Two typical scattering functions are shown in the left sketch of fig. 3.2. The left curve shows a fast decay and corresponds to a system at a higher temperatures in the liquid state far away from the glass transition. Here, one observes a ballistic regime at short times with the correlation function decays with a t^2 dependence followed by a microscopic regime at intermediate times and an exponential Debye decay at long times. At

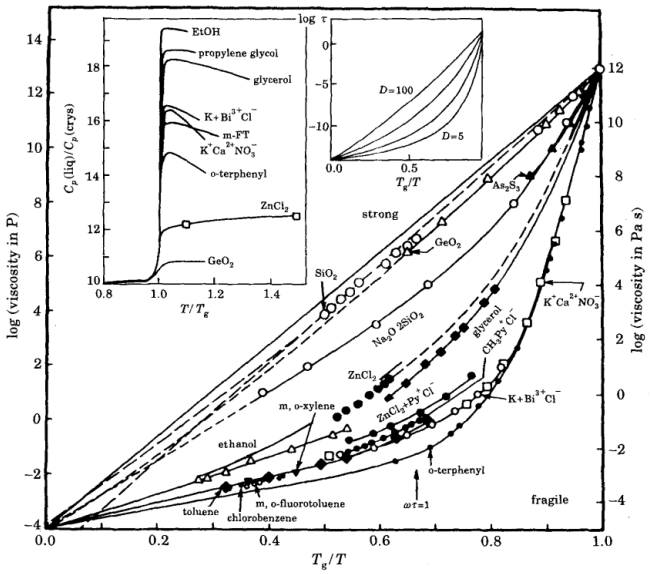

Figure 3.1 – Angell-plot of the viscosities for different systems against scaled inverse temperatures T_g/T with T_g the temperature where the viscosity has the values of 10^{13} Poise from [50].

lower temperatures $\phi_{\mathbf{q}}(t)$ shows a strongly different behavior. There, also a ballistic regime and then a microscopic regime is found but instead of a fast decay to zero a pronounced plateau is observed which is extended over decades in time. The time window where the correlation function is close to the plateau is called the β-relaxation regime. During that time the particles are trapped in the cage of the surrounding neighbors (right picture in fig. 3.2) and therefore are prevented from moving. Only for much longer times the correlation function decays to zero and thus the particles are able to leave their cages. This last regime is called the α-relaxation. Empirically it is found that the long-time behavior can be approximated by a stretched exponential function also known as "Kohlrausch-Williams-Watts" (KWW) function [51, 52]

$$\phi_{\mathbf{q}}(t) \approx A \exp\left[-(t/\tau_\alpha)^\beta\right], \tag{3.3}$$

with $\tau_\alpha(T)$ the relaxation time at temperature T. Up to now it is not completely understood where this non-Debye behavior at long times comes from and principally two different scenario are possible. In the heterogeneous case the relaxation times for each particle is different due to different surroundings and each particle shows a Debye relaxation. The stretched exponential behavior then follows from the average over all particles. In the homogeneous case all particles have the same relaxation behavior with a stretched exponential behavior. Thus, also the average shows that behavior. The reason for that long-time behavior is still a matter of research and it is not clear which of the two cases is the right one but probably both cases appear.

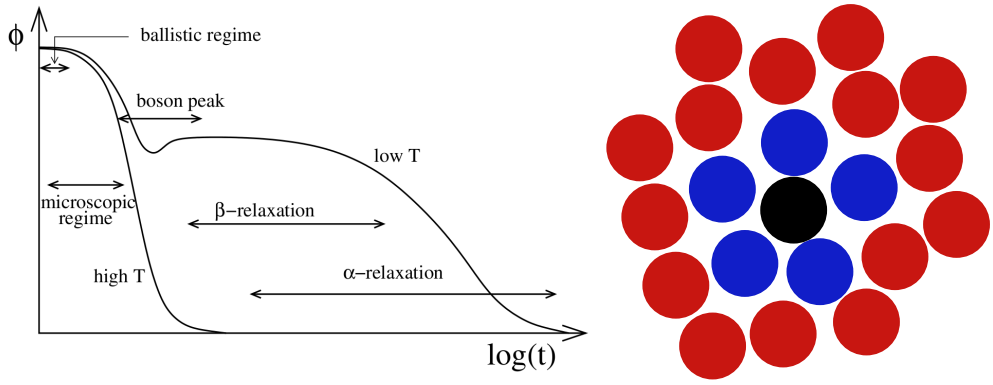

Figure 3.2 – Left) Time dependence of typical scattering function at two different temperatures. The left curve corresponds to a high temperature whereas the low curve shows a lower temperature with the typical two step relaxation process from [20]. Right) Illustration of the cage effect. The black particle is caged by the surrounding neighbor particles (blue) and therefore prevented from moving.

The second quantity which is often used to describe the motion of the particles is the mean-squared displacement $\langle \Delta r^2(t) \rangle$ (2.13). That quantity shows at short times a ballistic regime $\propto t^2$ followed by a diffusive regime $\propto t$ at high forces. In the supercooled liquid a third intermediate regime is observed for times inside the cages where that quantity also shows a pronounced plateau that can be extended over orders of magnitude in time. For the equilibrium system that behavior of the MSDs and of the incoherent scattering functions have been shown in fig. 2.5.

Up to now, no theory is available that describes all observed properties for the systems in the supercooled state although quite some progress has been made. The most successful theory at present is the mode coupling theory of the glass transition which describes many properties but not all.

For the understanding of the motion of a pulled particles in the supercooled liquid and below the glass transition temperature two quite different models are helpful. On the one hand there is a simple trap model based on a directed Langevin equation in a fixed random environment. This model shows unusual superdiffusive motion in the direction parallel to the force and a transition to a diffusive motion for higher forces. Both these predictions are also found in this work. On the other hand there is the mode coupling theory (MCT) for the glass transition. This theory can be extended to the case of a pulled particle in a supercooled liquid and gives for many properties as the mean squared displacement or the incoherent scattering function a good qualitative description for the behavior of the pulled particle close to the glass transition. But at the moment it fails at describing the superdiffusive motion of the pulled particles.

3.1 Mode coupling theory of the glass transition

The first theory described here is the mode coupling theory of the glass transition [19, 25, 26] that describes the behavior of systems in the supercooled state where the relaxation times and the viscosity of the system diverge close to a critical temperature T_c. Furthermore, it is the only theory that is based on the microscopic description of the motion of the particles and it leads to many predictions that are in a qualitative agreement with the results found in experiments and simulations. The original theory was developed to describe the unperturbed system in equilibrium or in the glass state. Only quite recently this formalism was extended to describe systems under the influence of external forces such as for sheared systems [53] or with a force acting on one single particle [54, 55, 56, 57]. Unfortunately, it requires quite some effort to solve the resulting equations of motion in this theory and often they cannot be solved at all. Therefore, a couple of approximations have to be carried out such as the restriction to only one q-value which lead to simplified versions of the original equations. These schematic models can be solved numerically but it comes at the cost of less precise or even unrealistic solutions.

3.1.1 General predictions of the theory

In this section the main predictions of the MCT shall be summarized. It is found that these properties are universally valid for many applications of the theory in quite different systems. The theory makes predictions for the time dependence of the correlation function $\phi_{\mathbf{q}}(t)$ of the density fluctuations $\rho_{\mathbf{q}}(t) = \sum_{i=1}^{N} \exp(i\mathbf{q} \cdot \mathbf{r}_i(t))$ in the system that corresponds to the coherent scattering function $F(q,t)$ (3.2)

$$\phi_{\mathbf{q}}(t) = \frac{F(q,t)}{S(q)}. \tag{3.4}$$

Here, $S(q) = F(q,0)$ is the static structure factor of the system. For this property the full mode coupling memory equation for $\phi_{\mathbf{q}}(t)$ can be written down [19, 25, 26] as

$$\ddot{\phi}_{\mathbf{q}}(t) + \Omega_{\mathbf{q}}^2 \phi_{\mathbf{q}}(t) + \Omega_{\mathbf{q}}^2 \int_0^t [M_{\mathbf{q}}^{reg}(t-t') + M_{\mathbf{q}}(t-t')]\dot{\phi}_{\mathbf{q}}(t')\mathrm{d}t' = 0, \tag{3.5}$$

where $\Omega_{\mathbf{q}}^2$ is a squared frequency and $M_{\mathbf{q}}(t)$ the memory kernel that gives the long time development of the correlator. They are given by

$$\Omega_{\mathbf{q}}^2 = \frac{\mathbf{q}^2 k_B T}{m S(q)}, \quad \text{and} \quad M_{\mathbf{q}}(t) = \int V_{\mathbf{q},\mathbf{k}}^{(2)} \phi_k(t) \phi_{|\mathbf{q}-\mathbf{k}|}(t) \mathrm{d}\mathbf{k}. \tag{3.6}$$

Here, the vertex $V_{\mathbf{q},\mathbf{k}}^{(2)}$ is a function of the static structure factor. The MCT makes several important predictions for a supercooled liquid. It predicts a dynamic phase

transition at a critical temperature T_c where the system changes from an ergodic liquid to a non-ergodic glass state. Beyond that temperature the theory even predicts a power law behavior of the relaxation time $\tau_\alpha(T)$ and the diffusion constant $D(T)$ above the critical temperature according to

$$\tau_\alpha(T) \propto (T - T_c)^{-\gamma} \tag{3.7}$$

and

$$D(T) \propto (T - T_c)^{\gamma}. \tag{3.8}$$

with the same exponent γ. As a consequence the product $\tau_\alpha(T) \cdot D(T)$ of these two properties is constant over the whole scaling range. At T_c the behavior of the correlation function changes quite drastically. Below the glass transition $\phi_{\mathbf{q}}(t)$ decays onto a plateau value $f(\mathbf{q})$, that is called the non-ergodicity parameter,

$$\phi_{\mathbf{q}}(t \to \infty) = f(\mathbf{q}). \tag{3.9}$$

Above but close to the critical temperature in the ergodic phase the correlation functions always decays to zero in the long time limit. Close to T_c a typical two-step decay can be observed. Here, two different relaxation regimes can be identified. The first one is the β-relaxation regime where the correlation function decays on intermediate times onto a plateau value. The interpretation of this behavior is that the particles are trapped at intermediate times inside a cage which is formed by the neighboring particles. In this regime the theory makes the prediction that the behavior of the correlation function can be written as

$$\phi_{\mathbf{q}}(t) = \tilde{f}_{\mathbf{q}} + h_{\mathbf{q}} G(t) \tag{3.10}$$

where the second term factorizes into a **q**-dependent and a time dependent function. This factorization property can be checked by calculating the fraction $R(t)$

$$R(t) = \frac{\phi_{\mathbf{q}}(t) - \phi_{\mathbf{q}}(t')}{\phi_{\mathbf{q}}(t'') - \phi_{\mathbf{q}}(t')}. \tag{3.11}$$

As long as the system is inside the β-relaxation regime all curves for $R(t)$ with different **q** values should collapse onto the same curve. For the late β regime the theory predicts that the correlator behaves according to

$$\phi_{\mathbf{q}}(t) = \tilde{f}_{\mathbf{q}} + h_{\mathbf{q}}^{(1)} t^b + h_{\mathbf{q}}^{(2)} t^{2b} + \ldots \tag{3.12}$$

where the first two terms are known as "von Schweidler law". For the long time behavior the particles leave the cage and enter a second relaxation regime, the α-relaxation regime. This time the correlation functions decays to zero. The theory makes no simple prediction about the exact functional behavior in this regime but empirically it is found that the long-time behavior can be well approximated by a stretched exponential function (3.3) and $\tau_\alpha(T)$ the relaxation time at temperature T can be calculated. Here,

the exponent β still shows a $\mathbf{q}$ dependence. In this regime the theory predicts that a time-temperature superposition principle (TTSP) holds:

$$\phi_{\mathbf{q}}(t,T) = \tilde{\phi}_{\mathbf{q}}(t/\tau_\alpha(T)). \tag{3.13}$$

Thus, after rescaling the time for measurements at different temperatures by the relaxation time $\tau_\alpha(T)$ it is predicted that all curves collapse onto the same universal curve.

3.1.2 MCT for a forced particle

Recently the MCT was extended to describe systems under the influence of external forces such as a shear field or a single particle under the influence of an external force. In the case of a pulled particle one is interested in the behavior of single particle properties. There, the correlator is the single particle correlator of the pulled particle $\phi^s_\alpha(t)$ that corresponds to the incoherent intermediate scattering function

$$\phi^s(t) = \langle \rho^{s*}(t)\rho^s(0)\rangle, \tag{3.14}$$

with $\rho^s(t) = \exp(i\mathbf{q}\cdot\mathbf{r}_i(t))$. Instead of only one memory equation for the bath particles multiple coupled memory equations have to be solved now. Due to the high complexity of these equations only simple schematic models have been solved up to now. These simple models reduce the full memory equations with the whole q-dependence to equations with only one or a few q-modes. The first solved schematic model only took one q-value in the parallel direction of the whole q-space into account [54, 55, 57]. Due to this strong simplification it fails in describing some important properties of the particle as a plateau in the friction coefficient at high forces. Therefore, this model was extended to a schematic model that depends on two different q-values, one parallel $\parallel$ and one perpendicular $\perp$ to the force direction [56, 57]. Therefore, it is based on three memory equations for $\phi(t)$, $\phi^s_\parallel(t)$ and $\phi^s_\perp(t)$. The first equation for the bath particles only depends on $\phi(t)$

$$\dot{\phi}(t) + \Gamma\left[\phi(t) + \int_0^t m(t-t')\dot{\phi}(t')\mathrm{d}t'\right] = 0, \tag{3.15}$$

with a a bilinear memory kernel $m(t)$

$$m(t) = \nu_1\phi(t) + \nu_2[\phi(t)]^2. \tag{3.16}$$

The other two equations are coupled and they describe the behavior of the pulled particle in both directions,

$$\dot{\phi}^s_\alpha(t) + \omega^s_\alpha\left[\phi^s_\alpha(t) + \int_0^t m^s_\alpha(t-t')\dot{\phi}^s_\alpha(t')\mathrm{d}t'\right] = 0, \tag{3.17}$$

where the index $\alpha \in \{\|, \perp\}$ stands for the directions parallel and perpendicular to the force. The external forces are brought into the model by the prefactors $\omega^s_\| = \Gamma_s(1 - ik_0 F^{\text{ex}})$ and $\omega^s_\perp = \Gamma_s$ with $\Gamma_s = 1$. The coupling between both directions of the probe and the bath correlator only happens inside the two memory kernels $m^s_\|(t)$ and $m^s_\perp(t)$,

$$m^s_\|(t) = \left[\nu^s_1 \phi^{s*}_\|(t)\phi(t) + \nu^s_2 \phi^s_\perp(t)\phi(t)\right] / (1 - ik_\| F_{ex}), \tag{3.18}$$

$$m^s_\perp(t) = \left[\nu^s_1 \phi^s_\perp(t)\phi(t) + \nu^s_2 Re[\phi^s_\|(t)]\phi(t)\right] / (1 + (k_\perp F_{ex})^2). \tag{3.19}$$

Here, ν^s_i and ν_i are real coupling parameters that define how strong the probe and the host liquid interact and k_α are parameters that allow to fine-tune the force scale (here $k_0 = k_\|$ was chosen). From the symmetry in the perpendicular directions follows that the perpendicular correlator is always a real quantity. Therefore only the real part of the parallel direction can contribute in that direction. With the calculated solutions of these equations one has access to additional properties of the particle as the friction coefficient ξ,

$$\xi = \xi^s_0 + \xi^s_0 \int_0^\infty (\mu_\| \text{Re}\phi^s_\|(t), + \mu_\perp \phi^s_\perp(t))\phi(t)\, dt\,. \tag{3.20}$$

the displacement in force direction $\delta z(t)$,

$$\xi^s_0 \partial_t \delta z(t) + \int_0^t \hat{m}^s_\|(t - t')\partial_{t'}\delta z(t')\, dt', = \kappa_\| F_{ex}\,, \tag{3.21}$$

the mean squared displacement in force direction $\delta z^2(t)$,

$$\begin{aligned} &\xi^s_0 \partial_t \delta z^2(t) + \int_0^t \hat{m}^s_\|(t - t')\partial_{t'}\delta z^2(t')\, dt', \\ =&2 + 2\kappa_\| F_{ex}\, \delta z(t) - 2\int_0^t K^s_\|(t - t')\partial_{t'}\delta z(t')\, dt'\,, \end{aligned} \tag{3.22}$$

and the mean squared displacement in perpendicular direction $\delta x^2(t)$,

$$\xi^s_0 \partial_t \delta x^2(t) + \int_0^t \hat{m}^s_\perp(t - t')\partial_{t'}\delta x^2(t')\, dt' = 2\,. \tag{3.23}$$

Here, ξ_0 is the friction coefficient of the bath particle. The memory kernels $\hat{m}^s_\alpha(t)$ and $K^s_\|(t)$ are given by

$$\hat{m}^s_\|(t) = \mu((1 - \mu_{\text{rel}})\text{Re}\phi^s_\|(t), + \mu_{\text{rel}}\phi^s_\perp(t))\phi(t)\,, \tag{3.24}$$

$$\hat{m}^s_\perp(t) = \mu((1 - \mu'_{\text{rel}})\text{Re}\phi^s_\|(t), + \mu'_{\text{rel}}\phi^s_\perp(t))\phi(t)\,, \tag{3.25}$$

$$K^s_{\parallel}(t) = -\mu\mu_B \mathrm{Im}\phi^s_{\parallel}(t) \ . \tag{3.26}$$

From these equations it is possible to calculate properties of interest in the long time limit, such as the diffusion constant in both directions or the steady state velocity. These predictions then can be directly compared to the simulation results.

In the liquid state this model predicts that the diffusion and relaxation of the probe particle is accelerated under the influence of the force. Here, in contrast to the simple trap model the motion stays completely diffusive in both directions for all forces. Below the critical glass temperature the motion completely freezes and the particle is trapped. At these temperatures the theory predicts a critical threshold forces that needs to be overcome to set the particle in motion.

3.2 Simple trap model

The second model is a simple one-dimensional trap model [58, 59] that tries to mimic the behavior of a pulled particle by a Brownian particle motion inside a force landscape. This potential is declining on average in one direction and therefore the particle feels a force in that direction. The original Langevin equation reads

$$\frac{dx}{dt} = \frac{1}{\gamma}F[x(t)] + \eta(t) \tag{3.27}$$

where x is the position of the particle at time t, γ is the friction coefficient of the particle, F the resulting force and η the thermal noise that leads to the motion inside the potential landscape. In this model η is a random variable with the following properties that define the temperature scale k_BT

$$\overline{\eta(t)} = 0, \quad \overline{\eta(t)\eta(t')} = 2\frac{k_BT}{\gamma}\delta(t-t'). \tag{3.28}$$

The first term in (3.27) is the force resulting from the potential landscape. In this model the force is also realized by a Gaussian white noise but now with a nonzero average force F_0

$$\langle F(x)\rangle = F_0, \qquad \langle F(x)F(x')\rangle - F_0^2 = \sigma\delta(x-x'). \tag{3.29}$$

It is found that the motion of the particle depends only on one control parameter μ and not explicitly on the values of F_0, D_0 or σ that is given by

$$\mu = \frac{2F_0D_0}{\sigma}, \tag{3.30}$$

with $D_0 = \frac{k_BT}{\gamma}$ the equilibrium diffusion constant. In [58, 59] it is shown that the physics of this driven particle in the long time limit is given by the long trapping times

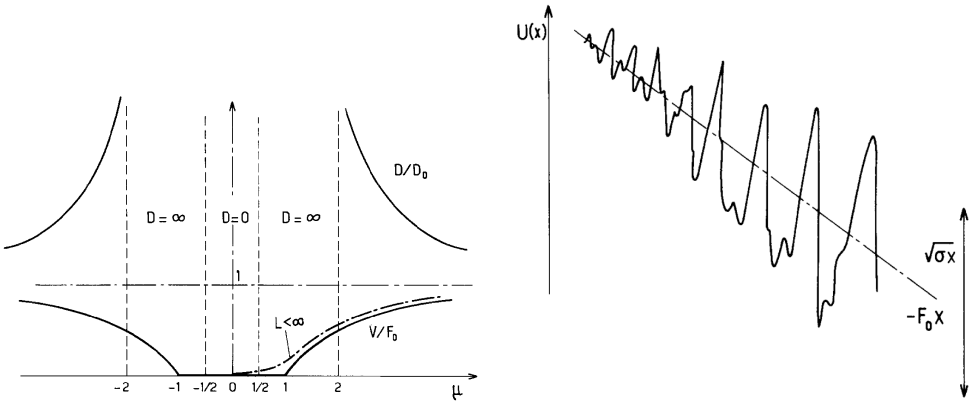

Figure 3.3 – Left) The behavior of the diffusion constant and of the velocity in dependence of the parameter μ. Right) Sketch of the potential landscape of the simple trap model. Both pictures are from [59].

in the deep valleys. It is found that these deep local minima have a broad probability distribution and therefore the particle behavior is well captured by a directed walk among traps with a broad distribution of release times $\Psi(\mathrm{W})$. Thus, the system can be described with a directed master equation

$$\frac{\mathrm{d}P_n}{\mathrm{d}t} = \mathrm{W}_n P_{n-1} - \mathrm{W}_{n+1} P_n, \tag{3.31}$$

with P_n is the probability of finding the system in state n and W_{n+1} the transition rate for the jump from state n to $n+1$. Here, the release times W are distributed according to the broad distribution $\Psi(\mathrm{W})$ for short W

$$\Psi(\mathrm{W}) \sim \mathrm{W}^{\mu-1}, \qquad \mathrm{W} \to 0. \tag{3.32}$$

This leads to a broad distribution for the waiting times τ that behaves as $\tau^{-(1+\mu)}$ at long times. This model has the advantage, that it can be solved exactly. In dependence of the strength of the external force one can identify three different regimes of that model (shown in the left picture of fig 3.3).

$0 < \mu < 1$: For small values of μ a creep motion is found. There, the displacement of the particle increases with a value of less than one in the long time limit and the mean squared displacement shows a behavior proportional to 2μ:

$$\langle\overline{x(t)}\rangle \propto t^{\mu}, \qquad \langle\overline{x(t)^2}\rangle - \langle\overline{x(t)}\rangle^2 \propto t^{2\mu}. \tag{3.33}$$

$1 < \mu < 2$: At intermediate forces the particles are trapped only a fraction of the time in deep local traps and otherwise they move untrapped through the system. This leads to a displacement that is proportional to the time. In this region the MSD shows a superdiffusive behavior:

$$\langle\overline{x(t)}\rangle \propto t, \qquad \langle\overline{x(t)^2}\rangle - \langle\overline{x(t)}\rangle^2 \propto t^{2/\mu}. \tag{3.34}$$

$2 < \mu$: For even higher forces the behavior of the particles is completely diffusive:

$$\langle\overline{x(t)}\rangle \propto t, \qquad \langle\overline{x(t)^2}\rangle - \langle\overline{x(t)}\rangle^2 \propto t. \tag{3.35}$$

Of course, the applicability and the predictions of this simple model are quite limited for a realistic model where a particle is pulled through a supercooled liquid or a glass. One property that is not contained in this model is the equilibrium dynamic of the system that should be restored for small forces. There, the model predicts a creep motion of the particle whereas in the supercooled liquid one would observe a linear response regime. Without an average force $F_0 = 0$ the diffusive motion in this model follows a logarithmic behavior (Sinai diffusion [60]) which is different from the normal diffusive motion in the equilibrium liquid. Nevertheless, it is at the moment the only model that predicts a superdiffusive behavior (second regime) and a transition to a diffusive regime at even higher forces (third regime) for a pulled particle.

Chapter 4

Overview of the steady-state behavior

After the equilibrium configurations were prepared at each temperature the measurement simulation runs can be started. At time $t = 0$ a start configuration is loaded and the external force is switched on for one of the particles. This force is kept constant for the rest of the simulation. After a short acceleration phase the pulled particle reaches a steady state with a constant average velocity. In this chapter the general characteristics of the particles in the steady state shall be determined and the important quantities that are used for this classification are introduced. In the steady state it is found that the behavior of the probe depends strongly on the strength of the applied external force. Beyond that, three different regimes can be identified that classify the particle motion in dependence of the force. For small forces a linear response regime is found, where the particle motion is given by the equilibrium properties. At intermediate forces one observes a non-linear regime where the particle motion is highly anisotropic. In the parallel direction a superdiffusive behavior is found whereas the motion in the perpendicular direction is strongly accelerated but still diffusive. Pulling with even higher forces leads to third regime. There, at high forces, one observes that the motion in both directions is again completely diffusive. In this chapter these three regimes shall be differentiated and an overview is given. Then, in the following two chapters these regimes are investigated closer.

4.1 Simulation details

The main part of the simulation took place on the Juropa cluster in Jülich. A typical simulation run was done on 160-640 cpu cores over 24 hours (which was the run time limit on the cluster). During such a simulation run typically around 1000-10000 particle trajectories were recorded. Here, the trajectories have a length of around 1-4 million time steps in the small system sizes and 100-400 thousand time steps in the big systems. These boundaries to the simulation results from the maximum job time on the

one hand and the system size on the other hand. Here, the particle is only allowed to move once and not multiple times through the whole box. As the speed of the particles is a function of the temperature in the system but also of the applied external force, the maximum runtime and the number of possible simulation runs is different for every single measurement.

One problem with these simulations is that one likes to gather as much information as possible about the particles in the system. To gain enough statistics of the pulled particles it is required to repeat the simulations for around 1000 different particles of the same type. With only a single pulled particle in the system one has compared to a normal equilibrium simulation the clear disadvantage that one cannot average over all the particles in the simulation box. This leads to a reduction of the statistics by a factor of 800 to 6400. As a consequence a much higher computational effort is required in this case and the produced amount of information is much higher. For example the required size of one system snapshot for a system with $L_x = 8L$ is around 1MB in size. The complete output of one simulation trajectory of 100k steps would therefore lead to an output of around 100GB. For only one single trajectory this amount is clearly orders of magnitude too big and a complete simulation with more than 1000 trajectories is thus completely unrealistic. As a consequence only partial informations of the systems can be written out and one has to chose in advance the properties and the precision of the measurement. As this work concentrates mainly on the behavior of the particle under the influence of the external force, the properties of that particle are of greatest interest and should be recorded. But even only the trajectories and the velocities of these pulled particles require too much space to easily write out at every time step. Therefore, only parts of the trajectories can be recorded. Here, different properties of the particles shall be investigated that are calculated on completely different timescales and on different time distances. Therefore, the particle trajectories were recorded in two different ways. The first one is a normal linear way where the position and velocities are recorded at equidistant times, typically every 40 or 80 time steps. From these measurements properties such as the average velocity, van Hove correlation functions or the jump and waiting time distributions can be calculated. Additionally the trajectories were recorded on a logarithmic time scale where the distance between measurements increases with time. From these measurements properties such as the incoherent scattering function or the mean squared displacement that are measured over the whole simulation run can be calculated without requiring too much disc space. To increase the statistics of these logarithmic measurements 10 trajectories with a shifted starting point of $1/10$ of the simulation time were recorded from the same particle trajectory.

In addition to these measurements some properties such as the pair correlation function were calculated directly during the simulation and only the results of these measurements were stored. Of course, these measurements have the clear disadvantage that one has to repeat the whole simulation if one wants to measure the property in a slightly dif-

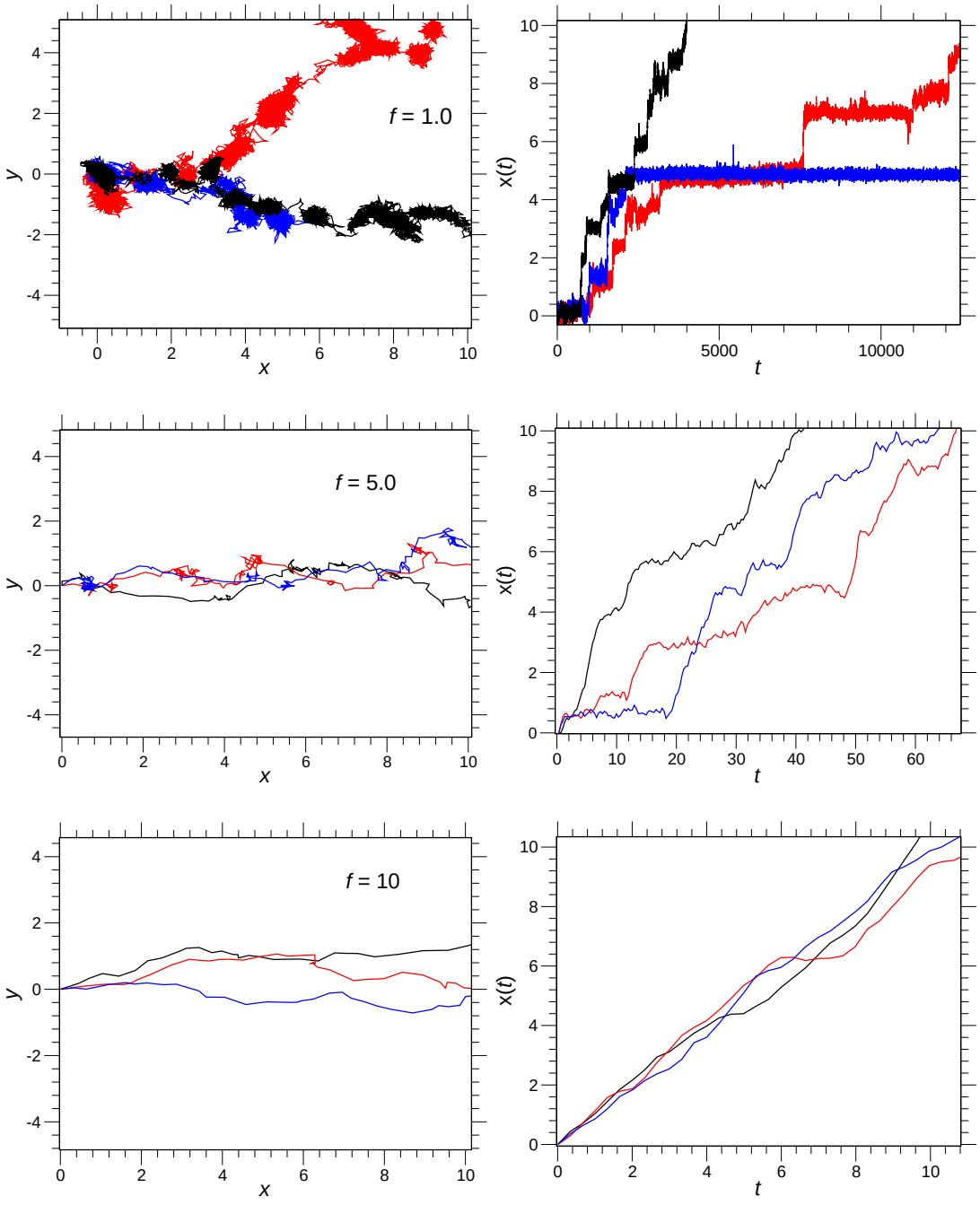

Figure 4.1 – Typical trajectories of A particles with forces $f = 1.0, 5.0, 10$ at the temperature $T = 0.14$. Left plots show trajectories in the x-y-plane with the starting point at $(0|0)$ and the endpoint at the right end of the plots. Right plots show the same trajectories, but now only the x-coordinate in dependence of the time.

ferent way or a completely different quantity. From all these data the important system properties can be calculated. After the switch on of the force at $t = 0$ one observes a transition to the steady state first which could influence the steady-state measurements. There, it is required to discard some of the data at the beginning of the simulation until the particle has reached the steady state. Therefore, the measurements were started first after the velocity of the probe was constant. In the case of the logarithmic timescale it was found that the second starting point after $1/10$ of the simulation was in all cases in the steady state and only the first measurement with the first starting point was discarded.

4.2 Velocity and friction coefficient

To get a first impression of the behavior of the probe particle it is quite useful to have a closer look at single particle trajectories. One finds that the motion of these pulled particles shows a strongly different behavior for varying external force. In fig. 4.1 some typical trajectories for pulled A particles at $T = 0.14$ with different external forces are shown. At each force, left and right plots show the same trajectories. Here, left plots show the trajectories in the x-y-plane whereas the right ones only show the x coordinates in dependence of the time. At low forces one observes that the particle trajectories show a jump motion. There, the particles are trapped most of the time in the cages of the surrounding particles and only rarely jump to the next cage. The average jump time is much shorter than the average cage time. By increasing the external force f one observes that the localization time decreases at intermediate forces (here $f = 5$) and the jumps occur with a much higher frequency. With even higher forces the trapping of the particles disappears and they move through the system without longer trapping times inside the cages. Note that all the plots show the same area in the x-y-plane on the left and the same distance $x(t)$ on the right but over different times. Hence one can see that with increasing force the particle motion is accelerated drastically. At $f = 1.0$ the time to move the distance to $x = 10$ takes until $t = 10000$ whereas at $f = 10$ it takes only until $t = 10$. This is two decades less in time compared to an increase of only one decade in the force. That is a first hint of a nonlinear behavior taking place at these forces. As a first property to quantify the particle motion, the velocities of the particles in the steady state is displayed in fig. 4.2. One finds that A and B particles show qualitatively the same force and temperature dependence but with slightly higher velocities for the A particles. It is an expected result due to the smaller particle diameter of the A particles. These lead to less friction from interactions with the surroundings during the motion and therefore to a higher average velocity. For small forces the velocity of the particles is proportional to the force. Here, the particle motion is still in the linear response regime. For forces inside this regime the friction from the bath is constant and therefore the velocity is proportional to the external force. With increasing forces the particles leave the linear response regime and

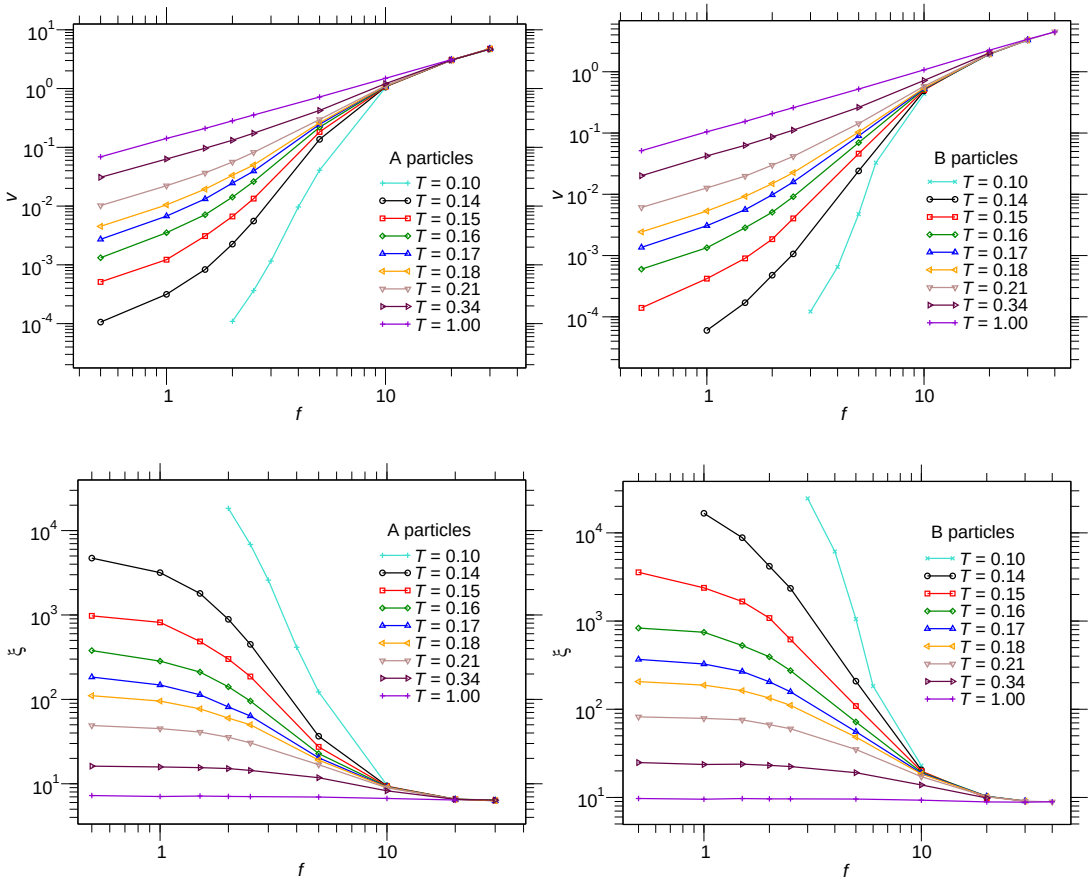

Figure 4.2 – Upper plots show steady state velocities of the pulled particle for different temperatures T in dependence of the external force. Lower plots show the resulting friction coefficients $\xi = f/v$. Left plots show A particles and right plots B particles.

enter the nonlinear regime. There, the velocity increases stronger than linear. In this region one observes a drastic increase of the velocities. This behavior strongly depends on the temperature and increases for lower temperatures. At the lowest equilibrium temperature $T = 0.14$ one finds an increase of the velocities from $v = 3.15 \cdot 10^{-3}$ at $f = 1.0$ to $v = 1.06$ at $f = 10$. This is an increase over nearly three decades in the velocity compared to only one decade in the force. For even higher forces the velocity dependence is again linear and converges against the behavior at $T = 1.0$. For that temperature the velocities of the particles are always in the linear response regime. For the highest forces the velocity curves at different temperatures collapse and therefore the particle motion is temperature independent. As a second quantity the friction coefficient ξ can be calculated from these measurements by

$$\xi = \frac{f}{v}. \tag{4.1}$$

The calculated values of ξ for both particle types are pictured in the corresponding lower plots of fig. 4.2. For small forces the friction coefficient is constant with a value given by the equilibrium system properties. There, the Einstein relation is still valid and one has $k_B T = \xi D_{\text{eq}}$, with D_{eq} the diffusion constant in equilibrium. This plateau corresponds to the linear response region of the velocity. At intermediate forces one finds a strong drop over up to 3 decades at the lowest temperature from the linear response plateau to a second plateau at high forces. In this regime all curves for different temperatures collapse onto the same plateau with values $\xi_\infty \approx 6.3$ for A and $\xi_\infty \approx 9.8$ for B particles. Note that this collapse has not yet been observed. In earlier Brownian dynamics simulations [54, 56] in a quasi-hard-sphere liquid the control parameter was the density of the system and not the temperature. There, one observes a density-dependent high force plateau value and not a collapse of the curves onto the same plateau.

4.3 Local structure

Under the influence of the force one can expect that the structure around the particle deforms. Hence, it is interesting to see what influence the pulled particle on the surrounding bath particles has. Therefore, the particle distribution function $g(\mathbf{r})$ is calculated which measures to what extent the structure around a particle deviates from a completely random structure with a constant density. This quantity is often used in the study of liquids as it gives informations about the average local structure even without a long range symmetry present in the system. Here, in the case of the pulled particle only the closer surrounding is of interest. In this case the particle distribution function [61] is given by

$$g(\mathbf{r}) = \frac{L^3}{N} \Big\langle \sum_{i \neq n} \delta(\mathbf{r}_i - \mathbf{r}) \Big\rangle, \tag{4.2}$$

and can be interpreted as the probability of finding a surrounding bath particle at distance $\mathbf{r}$ if the probe particle is located a zero. In the equilibrium case without external fields one has a spherical symmetry and therefore $g(r)$ depends only on the distance $r = |\mathbf{r}|$. In the case of the pulled particles the motion of the probe is anisotropic and therefore the full angular dependence needs to be recorded. In fig. 4.3 and fig. 4.4 the calculated pair distribution functions of the pulled particles at $T = 0.14$ for different external forces are displayed. In both figures upper plots show the behavior in the parallel direction and lower plots in the perpendicular direction. In the parallel direction it is required to measure the probability distribution over a small cylinder if one wants to gain enough statistics. Here, the radius of this cylinder was chosen as $r = 0.5$. In the perpendicular direction $g(\mathbf{r})$ is recorded in dependence of the radius r due to the rotational symmetry. As can be seen in the plots, the distribution function shows a strong anisotropic behavior that depends on the particle type and the external force.

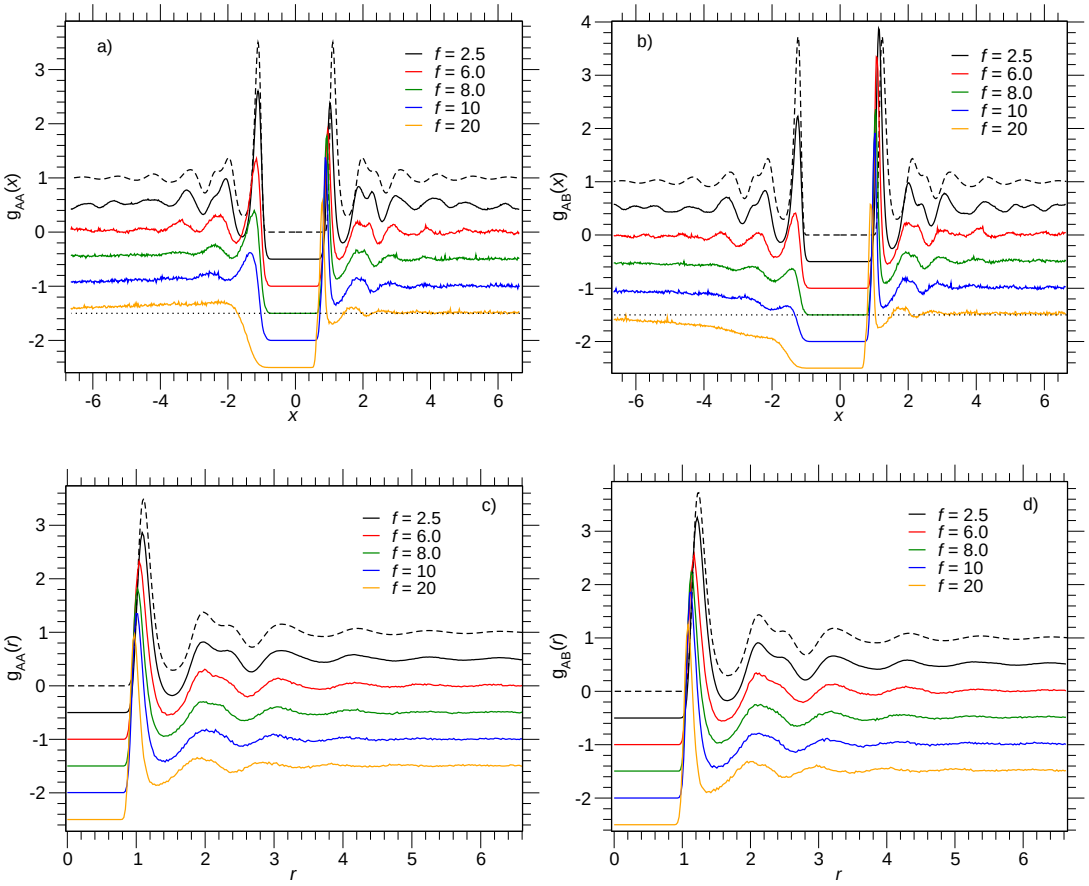

Figure 4.3 – Change of the local structure $g(\mathbf{r})$ around a pulled A particle at $T = 0.14$ for different forces f. Upper plots show pair correlation functions parallel to the force $g(x)$ and lower plots in the perpendicular direction $g(r)$. Left plots show surrounding A particles and right plots B particles. Dashed black line is the equilibrium behavior from [5].

The structure around the pulled particle at low forces is quite close to the equilibrium structure of the system (black dashed lines from [5]). For high forces ($f = 20$) the structure changes drastically especially in the force direction. There, it loses nearly all information of the equilibrium structure. At these forces the system around the pulled particle has not enough time to relax and the equilibrium structure cannot emerge. Additionally one has a strong dependence on the surrounding particle type. For surrounding A particles an increased probability behind the probe is found whereas for B particles this probability is reduced. That effect is highlighted with the horizontal dotted lines at the highest force. This dependence can be explained with the higher mobility of the smaller particles that can fill the free space faster which is left behind the moving probe particle. For the nearest neighbor peak in front of the particle one finds a slight shift to the probe particle with increasing force. There, the particles are pushed

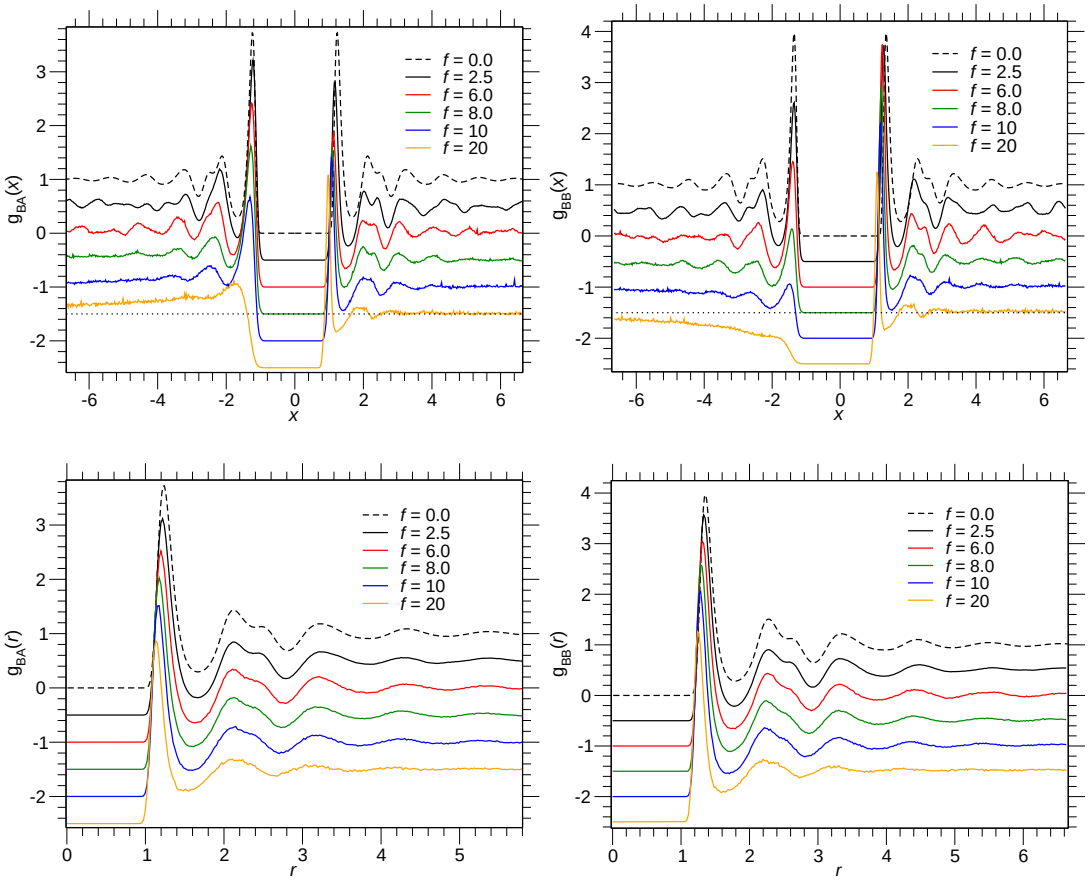

Figure 4.4 – Plots of $g(\mathbf{r})$ with the same system properties as in fig. 4.3 but now for pulled B particles.

closer together by the applied force. Behind the probe the nearest neighbor peak loses much of its height until it completely disappears at the highest forces. The behavior in the perpendicular direction is influenced as well. Also in this direction the peak of the first neighbor shell shows a dependence on the external force. With increasing f the position of the first peak changes. It moves closer to the probe. Under the influence of the force the probe moves closer to the neighboring particles. For higher distances the structure reduces more and more with increased force. At the highest forces the maxima and minima are much less pronounced although the reduction is not as strong as in the perpendicular direction. Here, again the system is not able to relax on these timescales.

The behavior at the highest forces is roughly in agreement with predictions of the dynamic density functional theory that were made for a polymer solution [62]. There, also an enrichment of the particles in front of the probe and and a hole behind the probe is found. Note, that although the structure at high forces changes drastically, for forces up to $f = 2.5$ the structure is nearly the same as in equilibrium. This is

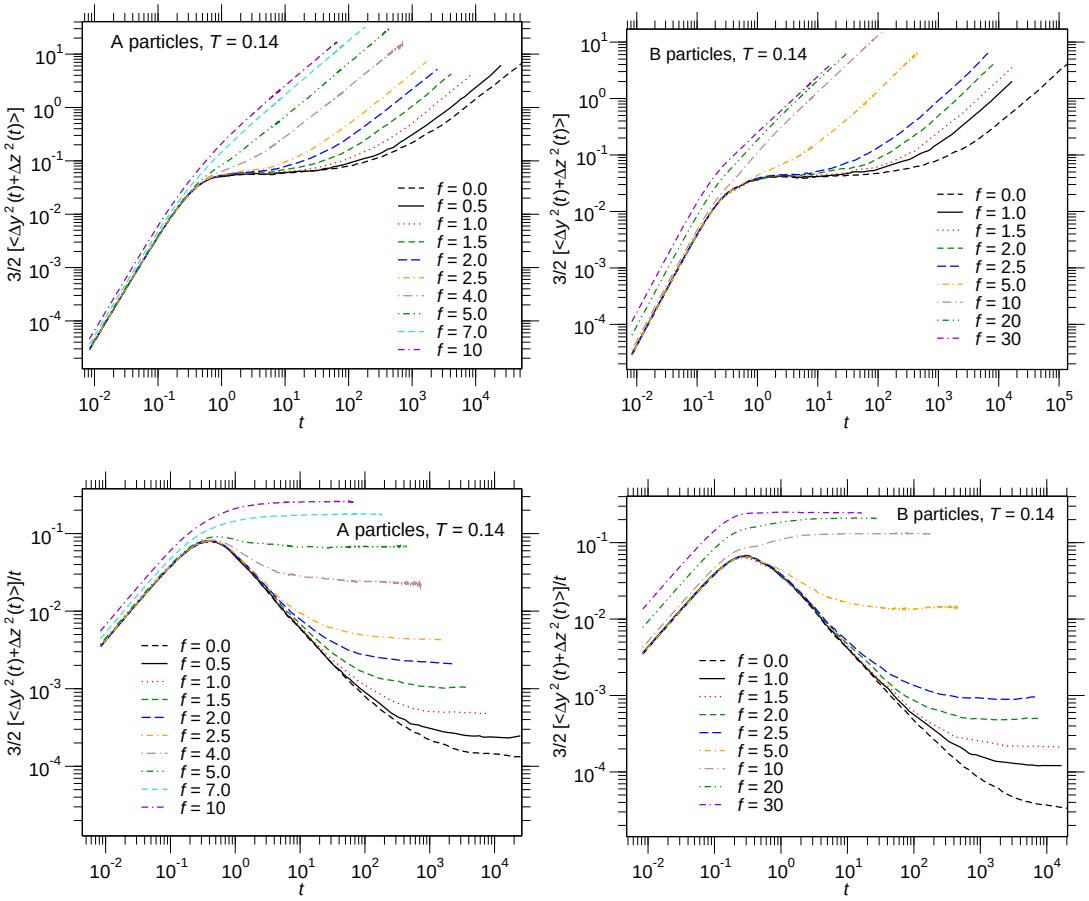

Figure 4.5 – Mean-squared displacement for pulled particles in the direction orthogonal to the force at $T = 0.14$ for different f. Upper plots show MSDs in dependence of the time t and lower plots the same curves divided trough t to highlight the long time behavior. Both for A (left) and B (right) particles.

in contrast to the strongly influenced behavior of other dynamical quantities in the region $0.5 \leq f \leq 2.5$ which are presented in the following. That is a quite often found phenomenon in the dynamics of glassy systems where the dynamic quantities can change drastically but the static properties, as the pair correlation function or the structure factor, show barely any difference.

4.4 Mean squared displacement

The static properties of the system already showed some interesting behavior, but the main focus of this work lies on the dynamic quantities of the probe particle. As a property the mean-squared displacement is determined. It gives information about the deviation from the average position for the particles and their long time diffusive

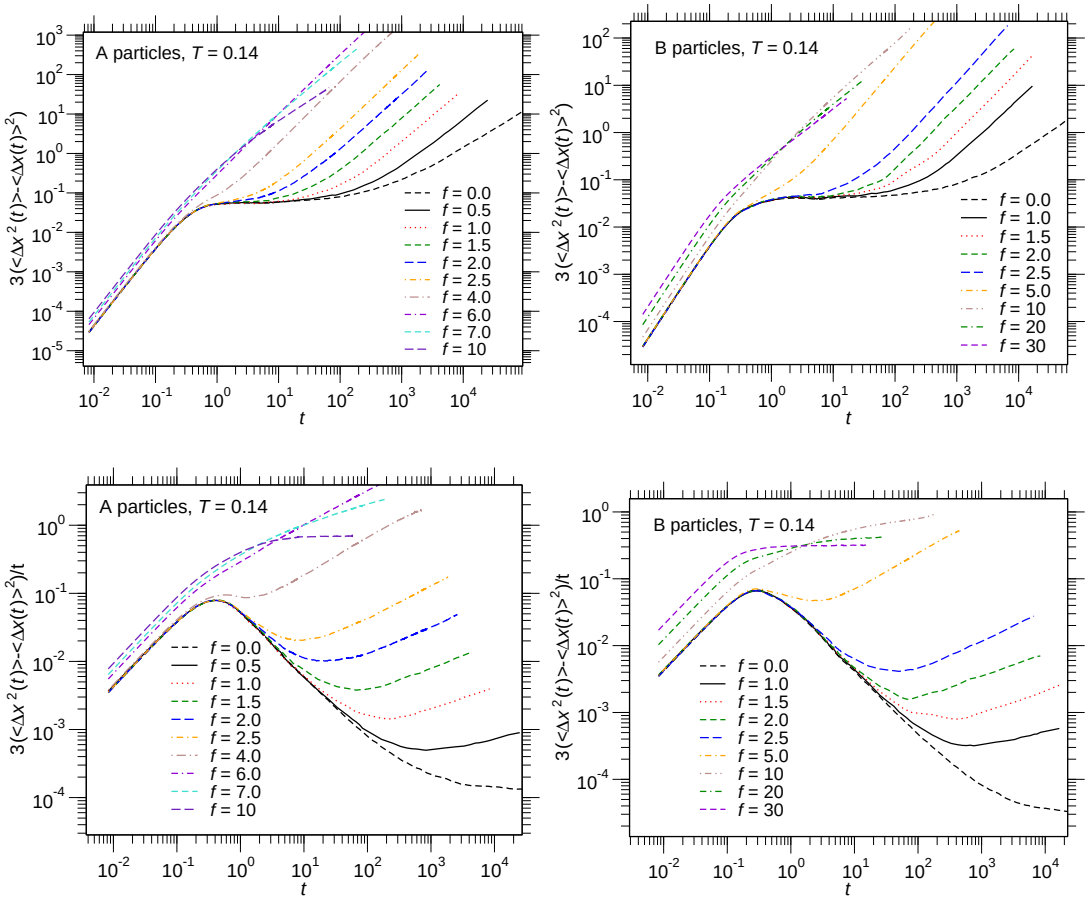

Figure 4.6 – Mean-squared displacement for pulled particles in the force direction at $T = 0.14$ for different f. Upper plots show MSDs in dependence of the time t and lower plots the same curves divided trough t to highlight the long time behavior. Both for A (left) and B (right) particles.

behavior. The usual equilibrium definition of that quantity is

$$\left\langle \Delta r^2(t) \right\rangle = \left\langle |\mathbf{r}(t) - \mathbf{r}(0)|^2 \right\rangle. \tag{4.3}$$

For the pulled probe that quantity needs to be slightly modified. In the orthogonal direction it is the same as in the equilibrium case

$$\left\langle \Delta y^2(t) + \Delta z^2(t) \right\rangle = \left\langle [y(t) - y(0)]^2 + [z(t) - z(0)]^2 \right\rangle. \tag{4.4}$$

Due to the drift of the pulled particle the definition (4.4) is not applicable in the force direction. There, one has to subtract the drift motion first and one obtains

$$\left\langle \Delta x^2(t) \right\rangle = \left\langle [x(t) - x(0)]^2 \right\rangle - \left\langle [x(t) - x(0)] \right\rangle^2. \tag{4.5}$$

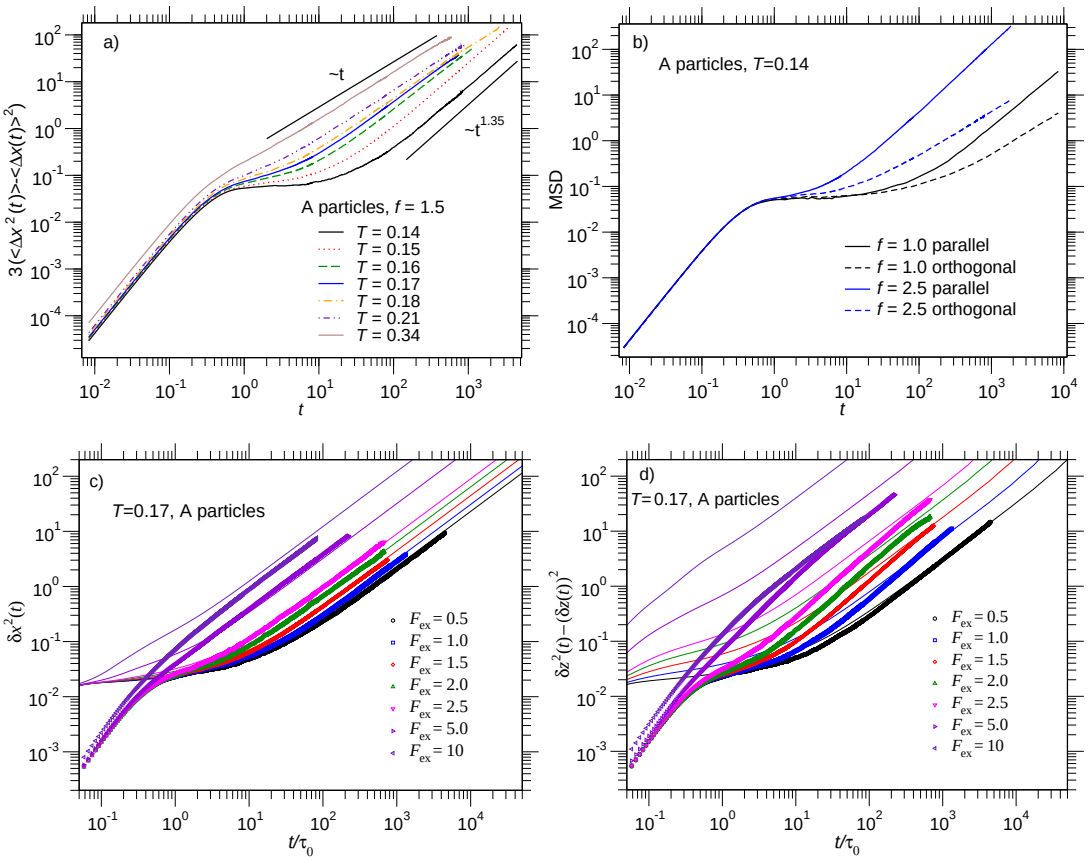

Figure 4.7 – a) Mean-squared displacement in the force direction for different temperatures at force $f = 1.5$. b) Direct comparison of the two mean-squared displacement directions for A particles with forces $f = 1.0$ and $f = 2.5$ at $T = 0.14$. Straight lines show MSDs in parallel and dashed lines in orthogonal direction. Lower plots show a comparison of simulation results (symbols) with the prediction from the schematic model (straight lines) in c) perpendicular and d) parallel direction from [63].

By that definition the MSD in the parallel direction measures the average squared deviation from the mean position at time t. Thus, this quantity gives a closer picture of the time dependent diffusion behavior of the particles under the influence of the external force. In the steady state the mean-squared displacement of the probe particles shows a strong dependence on the external force. In fig. 4.5 MSDs are shown on a logarithmic scale in the perpendicular direction at the lowest temperature $T = 0.14$ for different forces. Also shown here is the equilibrium curve (dashed line, from [5]). At low forces one finds that the MSDs behave quite similar to the equilibrium case. There, one can clearly distinguish three different parts. For short times one finds a ballistic regime. Here, the particles move freely without the influence of the surrounding particles with a constant velocity. This leads to a displacement proportional to t. Thus, the MSDs for short times $\langle \Delta r^2(t) \rangle \sim t^2$ in the case of the Newtonian dynamics. After some

time the particles feel the influence of the potentials of the surrounding particles and the curves deviate from this motion. In the case of supercooled liquids a pronounced plateau at intermediate times is observed. There, the particles are trapped inside the cage of the neighboring particles. The probe particle is localized. For the lowest forces and in equilibrium one finds that the intermediate plateau shows a strong temperature dependence and it is extended over 2-3 decades in time for both particle types. This is a typical behavior for a glass forming liquid close to the critical temperature. Due to the applied force the particles manage to escape their cages earlier. Therefore, with increasing force the length of the plateau decreases until it completely vanishes for forces $f > 5$. From there on the cage structure does not influence the motion of the particles anymore. Even at low forces the particles can leave their cages and diffuse through the system at long times. As a consequence, the MSD is linear $\langle \Delta r^2(t) \rangle \sim t$ at late times in the diffusive regime. To highlight the diffusive behavior in the long time limit the same MSDs divided by the time t are shown in the lower plots of fig. 4.5. At long times a convergence towards a constant plateau value that corresponds to twice the value of the diffusion constant of the curves can be seen. For the direction parallel to the force the picture is a bit different. In fig. 4.6 the same plots for the direction parallel to the force are shown. There, one finds for short and intermediate times an identical behavior of the MSDs. Only for long times the curves differ as the motion is not diffusive. Here, the slope of the long time limit is bigger than one and therefore shows superdiffusive behavior ($\langle \Delta x^2(t) \rangle \sim t^\alpha$ with $\alpha > 1$). This can best be seen in the lower plots, where the curves divided by t do not converge against a constant plateau value for long times. Instead one observes a power law increase. This shows that the motion of the pulled particles is superdiffusive on time scales accessible in the simulations. At high forces, where the particle motion shows no sign of the cage anymore, the superdiffusive regime disappears and the motion in the parallel direction becomes diffusive again. The superdiffusivity not only depends on the applied force but also on the temperature of the system. With lower temperatures one finds an increase of α. This is shown in fig. 4.7 where MSDs in parallel direction for A particles with $f = 1.5$ at different temperatures can be seen. The exponent α at long times steadily increases from $\alpha = 1$ at $T = 0.34$ to $\alpha \approx 1.35$ at $T = 0.14$.

In both directions one finds that with increasing force the ballistic regime is shifted to higher values (fig. 4.5 and fig. 4.6). For smaller forces, as long as the curves show a pronounced plateau, the regime collapses onto the same curve. Only for high forces ($f > 5$ for A particles and $f \geq 10$ for B particles) they differ. This can be understood as the slope of the ballistic regime at short times corresponds directly to the temperature of the pulled particles. Obviously for high forces the DPD thermostat has problems to locally cool the system to the bath temperature. Note that the temperature of the bath particles in the system is still constant at the equilibrium temperature and only the temperature of the probe and the close surrounding is slightly increased. For a comparison of the behavior in both directions the parallel and perpendicular MSDs are shown together for forces $f = 1$ (black) and $f = 2.5$ (blue) in fig. 4.7. Both directions show

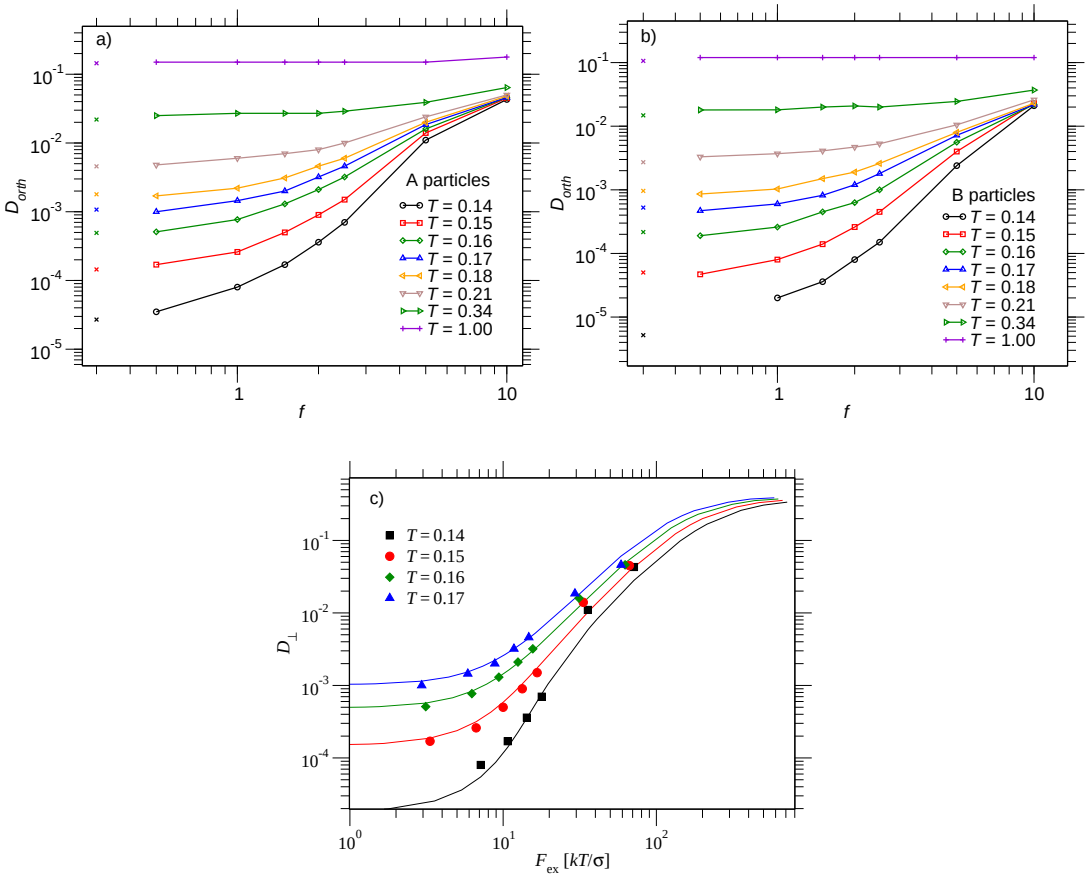

Figure 4.8 – Diffusion constant D_{orth} for the pulled particles in the direction perpendicular to the force for a) A and b) B particles in dependence of f at different temperatures. Crosses mark the values of the equilibrium diffusion constant calculated in [5]. c) Comparison of the orthogonal diffusion coefficient from the simulations (symbols) with the predictions from the schematic model (straight line) (3.17) from [63].

an identical behavior during the ballistic regime. Even for the time in the plateau both curves match over a long time. Only at late times, when the particle leaves the cage, both curves start to diverge with a linear long time behavior for the orthogonal and a superlinear behavior in the parallel direction. This indicates that the particle motion at short times and inside the cage is isotropic. But outside the cage where the jump motion from cage to cage takes place the motion gets anisotropic. These measured MSDs can be directly compared to calculations in the schematic model. In fig. 4.7 some plots from [63] are shown for A particles at $T = 0.17$ and different forces. In the direction perpendicular to the force one finds a good agreement for the long time diffusive regime and even the plateau value for the lower forces agrees with the theoretical predictions. Only for the short time behavior one finds a strong deviation which is caused by the different types of the microscopic motion. The schematic models are

based on the Brownian motion which shows a diffusive motion at short times whereas the simulations solve the Newtonian equations and thus show a Newtonian dynamics. For the direction parallel to the force a different picture emerges. There, the behavior of theory and simulation differs quite drastically as the theory shows no superdiffusive behavior and at the moment the theory is not able to explain that part of the behavior in the force direction.

The mean-squared displacement in the orthogonal direction is linear in time. Hence, it is possible to calculate the diffusion constant of the probe particles and have a look at the force dependence. D_{orth} is given by the Einstein relation [64]

$$D_{\text{orth}} = \lim_{t\to\infty} \langle \Delta y^2(t) + \Delta z^2(t) \rangle / (4t). \tag{4.6}$$

The calculated values for the different temperatures in dependence of the applied force are shown in fig. 4.8. In the linear response region the value of the diffusion constant is constant and equal to the equilibrium diffusion. For better visualization the equilibrium values calculated in [5] are marked with crosses. With increasing forces the diffusion increases drastically in the perpendicular direction over up to 3 orders of magnitude at the lowest temperature $T = 0.14$. For high forces D_{orth} converges against another plateau and in contrast to the behavior of the friction coefficient the plateau value this time still depends on the temperature. As the MCT makes predictions for the diffusion constant a direct comparison is possible. Except for the lowest temperatures the values of the MCT are in agreement with the simulated ones which can be seen in fig. 4.8 c).

4.5 Correlation functions

In chapter 3.1.1 a few of the predictions from the MCT were presented. There, the basic observable in this theory is the correlation function $\phi_{\mathbf{q}}(t)$ (3.4) and it is therefore of great interest to calculate this quantity in the simulation and compare it with the theoretical predictions. Here, the correlation function corresponds to the incoherent intermediate scattering function $F_s(q,t)$ of the probe particle which is defined in the bulk as

$$F_s^{\alpha}(\mathbf{q},t) = \frac{1}{N_\alpha} \sum_i^{N_\alpha} \Big\langle \rho_i(\mathbf{q},0)\rho_i(\mathbf{q},t) \Big\rangle, \tag{4.7}$$

with N_α the number of particles of type α and $\rho_i(\mathbf{q},t) = \exp(i\mathbf{q}\cdot\mathbf{r}_i(t))$ the density fluctuation of particle i. For bulk measurements this quantity usually is averaged over all particles in the system. With the external force only one particle is pulled through the system and therefore the expression reduces to

$$F_s(\mathbf{q},t) = \Big\langle \rho(\mathbf{q},0)\rho(\mathbf{q},t) \Big\rangle = \Big\langle \exp\left(-i\mathbf{q}\cdot[\mathbf{r}(t)-\mathbf{r}(0)]\right) \Big\rangle. \tag{4.8}$$

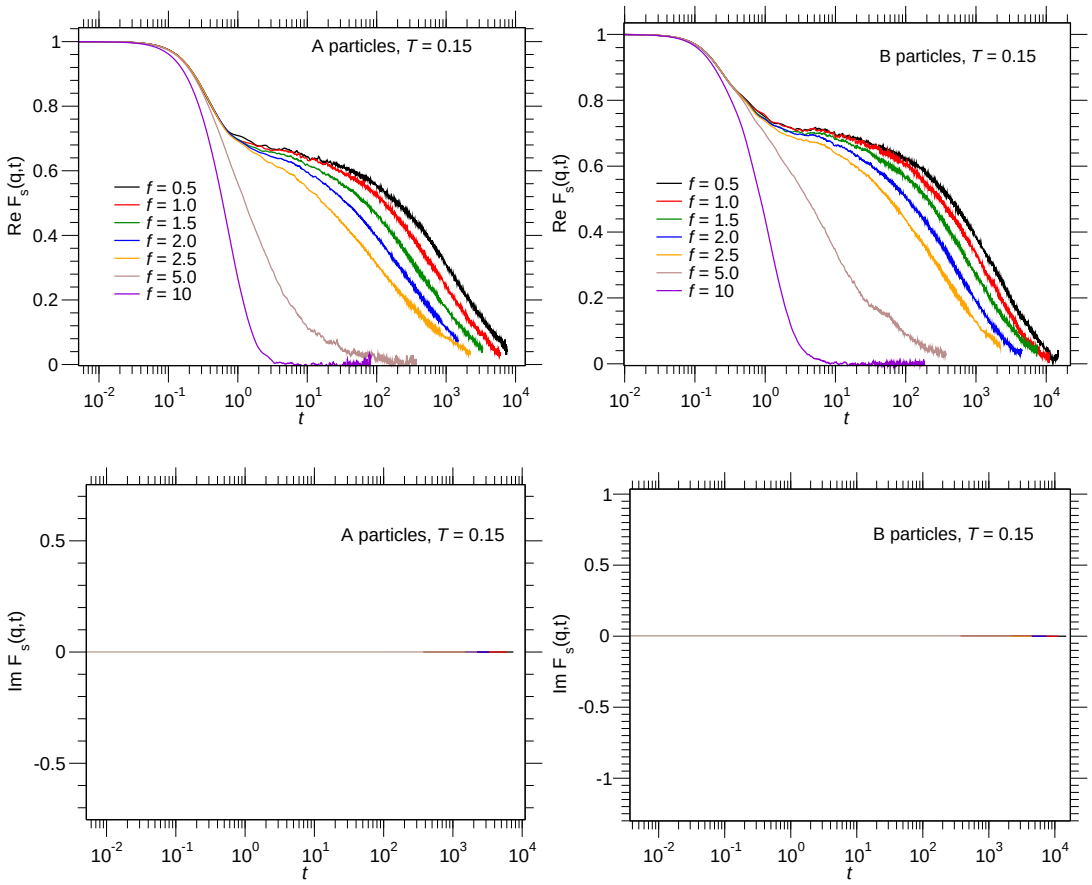

Figure 4.9 – Incoherent scattering function $F_s(q,t)$ of the pulled particle at $T = 0.14$ and $q = 6.14$ for different forces orthogonal to the force direction. First plots show real part and lower plots imaginary parts of the scattering function for A (left) and B (right) particles. Imaginary part in the perpendicular direction is zero for all forces.

In fig. 4.9 and 4.10 $F_s(q,t)$ for A and B particles at $T = 0.15$ and $q = 6.14$ with different applied forces are shown. Compared to the equilibrium case (fig. 2.5), the behavior of the incoherent scattering function for the pulled particle is more complex. As the other quantities of the pulled particle also $F_s(q,t)$ shows a strong anisotropic behavior. In the direction perpendicular the general behavior of $F_s(q,t)$ is quite similar to the equilibrium case. At short times during the ballistic regime one has a fast decay to a plateau. At long times one finds a decay from this plateau with a stretched exponential behavior in the α-regime. In this case higher applied forces lead to a reduced plateau and a faster decay. In that direction the behavior under the influence of the force is comparable to the equilibrium decay at higher temperatures. For the parallel direction two strong differences appear. The first is that at high forces the correlation function shows oscillatory behavior with even negative values. The second difference is the occurring imaginary part which is zero in the perpendicular direction and in equilibrium.

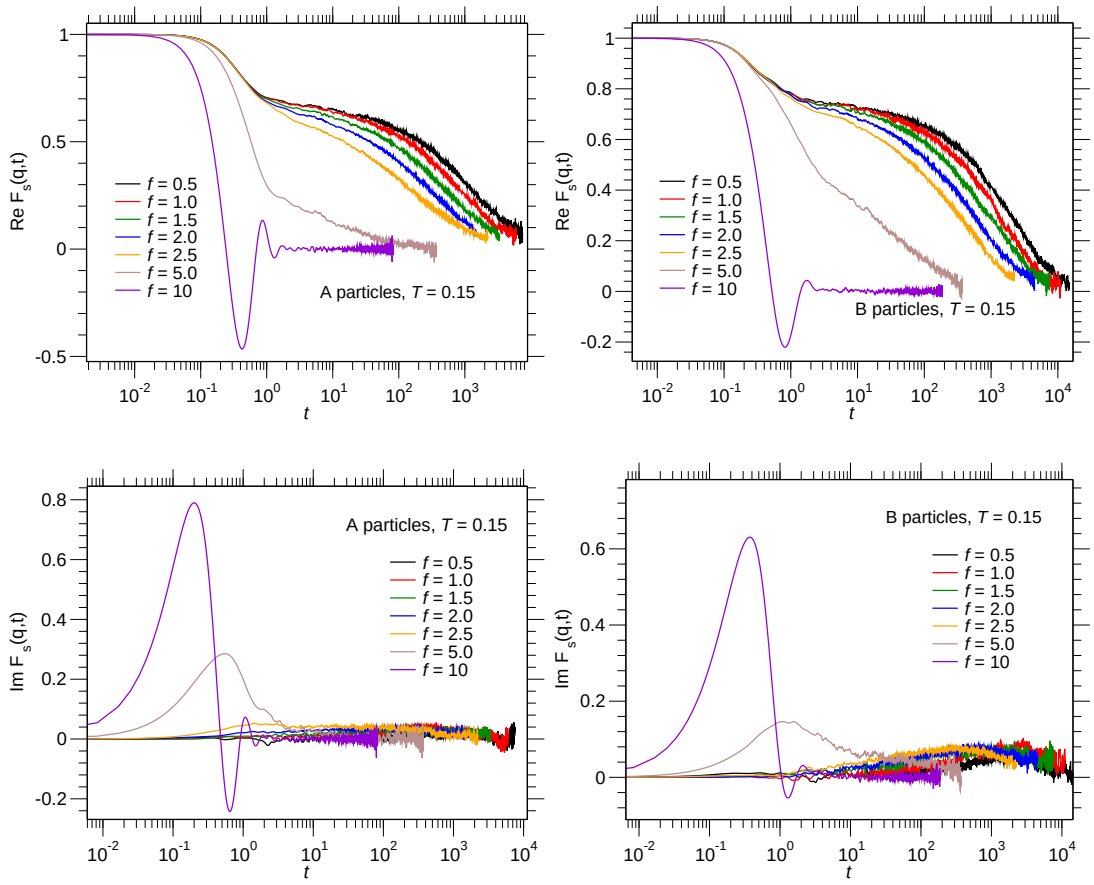

Figure 4.10 – Incoherent scattering function $F_s(q,t)$ of the pulled particle at $T = 0.14$ and $q = 6.14$ for different forces in the force direction. First plots show real part and lower plots imaginary parts of the scattering function for A (left) and B (right) particles.

Both points are the result of the drift motion that is not subtracted here as it leads to a prefactor of $\exp(-ivt)$ in the scattering function. This term oscillates with time and introduces the imaginary behavior.

The last quantity introduced here is the self part of the van Hove function $G_s(r,t)$ [61] given in the equilibrium case by

$$G_s^\alpha(\mathbf{r},t) = \frac{1}{N_\alpha}\left\langle \sum_{i=1}^{N_\alpha} \delta(\mathbf{r} - |\mathbf{r}_i^\alpha(t) - \mathbf{r}_i^\alpha(0)|)\right\rangle. \tag{4.9}$$

Again, only the motion of the probe is of interest and therefore the above expression reduces to

$$G_s(\mathbf{r},t) = \left\langle \delta(r - |\mathbf{r}(t) - \mathbf{r}(0)|)\right\rangle, \tag{4.10}$$

with $\mathbf{r}(t)$ the coordinate of the pulled particle at time t. That quantity gives the probability of finding the probe at time t on the position $\mathbf{r}(t)$ if it was at $t = 0$ at $\mathbf{r}(0)$. This

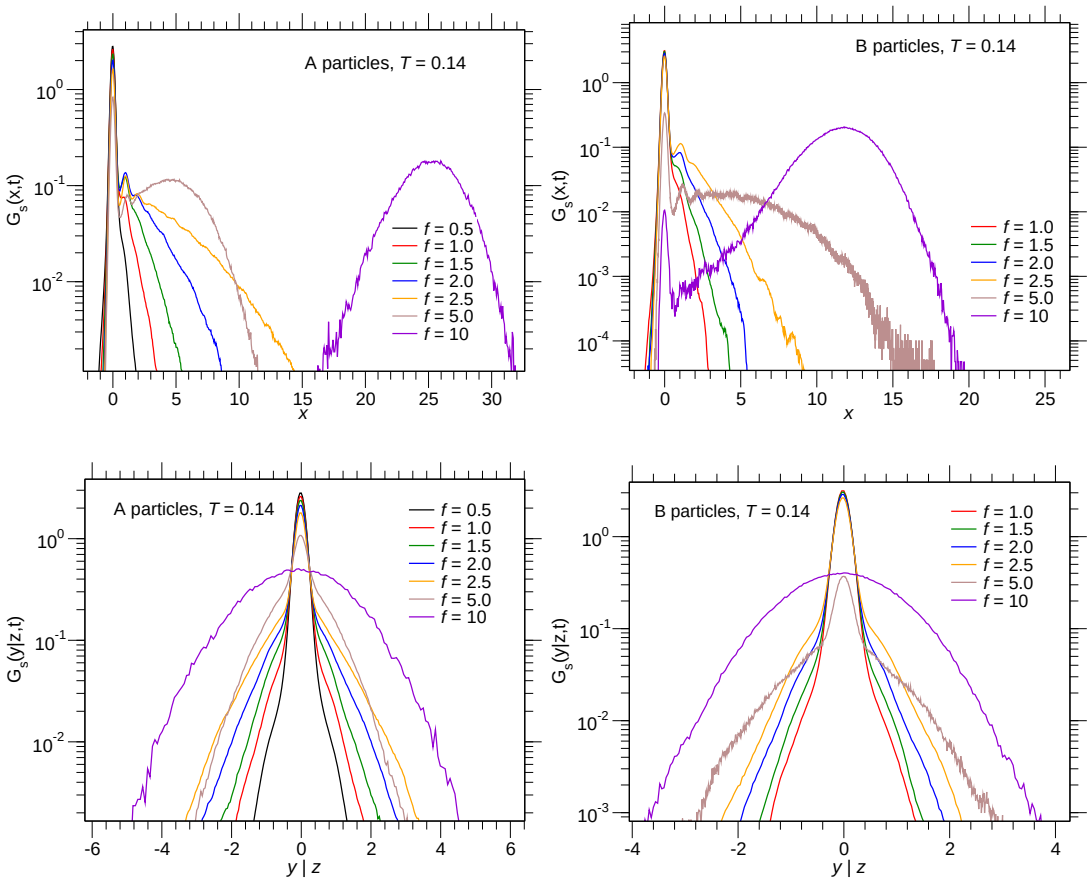

Figure 4.11 – Steady state van Hove correlation functions $G_s(r,t)$ for a (left) and B (right) particles with different forces f at times $t = 249$ for forces $f = 5.0, 10$ and $t = 664$ else. Upper plots show $G_s(r,t)$ measured in the force direction and lower in perpendicular directions.

quantity is also calculated independently in both directions. Displayed in fig.4.11 are the obtained results at $T = 0.14$ in dependence of the force. There, the upper plots show $G_s(r,t)$ in parallel and lower in the perpendicular direction. In parallel direction for low and intermediate forces up to $f = 5.0$ the van Hove correlation functions show a pronounced peak at $x = 0$. This is a result of the strong caging of the surrounding particles at low temperatures which prevent the particle from leaving the initial position. Only a fraction of the particles manages to move further than the initial cage. The strength of that effect reduces with increased force until it disappears for high forces ($f \geq 10$ for A and $f > 10$ for B particles). Then, the particles move without being trapped inside the cages and the shape of the van Hove correlation function is Gaussian. At low forces $G_s(\mathbf{r},t)$ has a long tail in the force direction. In the perpendicular direction the symmetry is not broken by the force and $G_s(\mathbf{r},t)$ is symmetric at all forces. At low and intermediate forces one finds strong exponential tails as in the

equilibrium state [5] and a strong peak at the initial position that results from the trapping in the cages. For higher forces a transition to a Gaussian shape can be observed and the pronounced localization peak at zero disappears.

4.6 Summary

In this section the general behavior of the probe particle under the influence of an external force was characterized. It is found that the particle motion strongly depends on the strength of the applied forces and three different regimes can be identified.

Small forces: For small external forces the particle motion is given by the equilibrium properties of the system. Here, the linear response theory is still valid and can be used to predict the behavior of the pulled probe. In this region the behavior of the particle is still isotropic and only shifted in the force direction by the drift.

Intermediate forces: For intermediate forces one observes a strong anisotropic motion and with increasing forces a strong decrease of the friction coefficient takes place. Parallel to the force a pronounced superdiffusive regime in the mean-squared displacements is observed whereas in the perpendicular direction the behavior is still diffusive but it is strongly accelerated.

High forces: At high forces the friction coefficient shows a second plateau and the velocity increases again linear with the applied force. In this region the superdiffusive behavior disappears and a transition to a diffusive behavior in the parallel direction takes place. Here, the anisotropy of the motion reduces again.

Furthermore, a comparison with calculations from the MCT showed that the data for the perpendicular MSDs and the diffusion coefficients are in agreement with the measured values. But the superdiffusive regime in the parallel direction is completely missing in the schematic model. In the following chapters these regimes are investigated in detail and it is checked how good these measurements can be understood with the theoretical models.

Chapter 5

Scaling regime at intermediate forces

5.1 Universal behavior

In the last chapter the behavior of the particle in the steady state was classified and three different regimes were identified. The second regime, the regime at intermediate forces, is investigated in detail in this chapter. In this regime the particle motion is strongly affected by the surrounding cages. As was seen in fig. 4.7 b) the motion of the particle is highly anisotropic in the long time limit where the particle has left the cage and one observes superdiffusive motion. Here, it is found that with a constant applied force the probe shows a universal behavior in dependence of the temperature. This leads to a description of the particle motion with an effective temperature. Furthermore, it is checked in this chapter how far the classical MCT predictions can describe the behavior of the pulled probe particle in the steady state.

5.1.1 Peclet number

In order to quantify the effect of the external force on the particle in the non-linear response region the Peclet number Pe^* can be used. This quantity relates $\tau_D = \sigma^2/D_{\text{eq}}$ the typical timescale of the equilibrium diffusion with $\tau_f = \sigma/v = \sigma\xi/f$ the timescale introduced by the drift motion of the pulled particle. Here, σ is the diameter of the particle and D_{eq} the diffusion constant in equilibrium,

$$Pe^* = \frac{\tau_D}{\tau_f} = \frac{\xi_0 f_{\text{scal}}}{\xi}. \tag{5.1}$$

In addition the friction coefficient of the bath ξ_0 and the scaled forces f_{scal} are given by $\xi_0 = k_B T/D_{\text{eq}}$ and $f_{\text{scal}} = f\sigma/\xi$. This choice of the scaled force has the advantage that in the linear response region, where $\xi = \xi_0$ holds Pe^* is equal to f_{scal} and then in

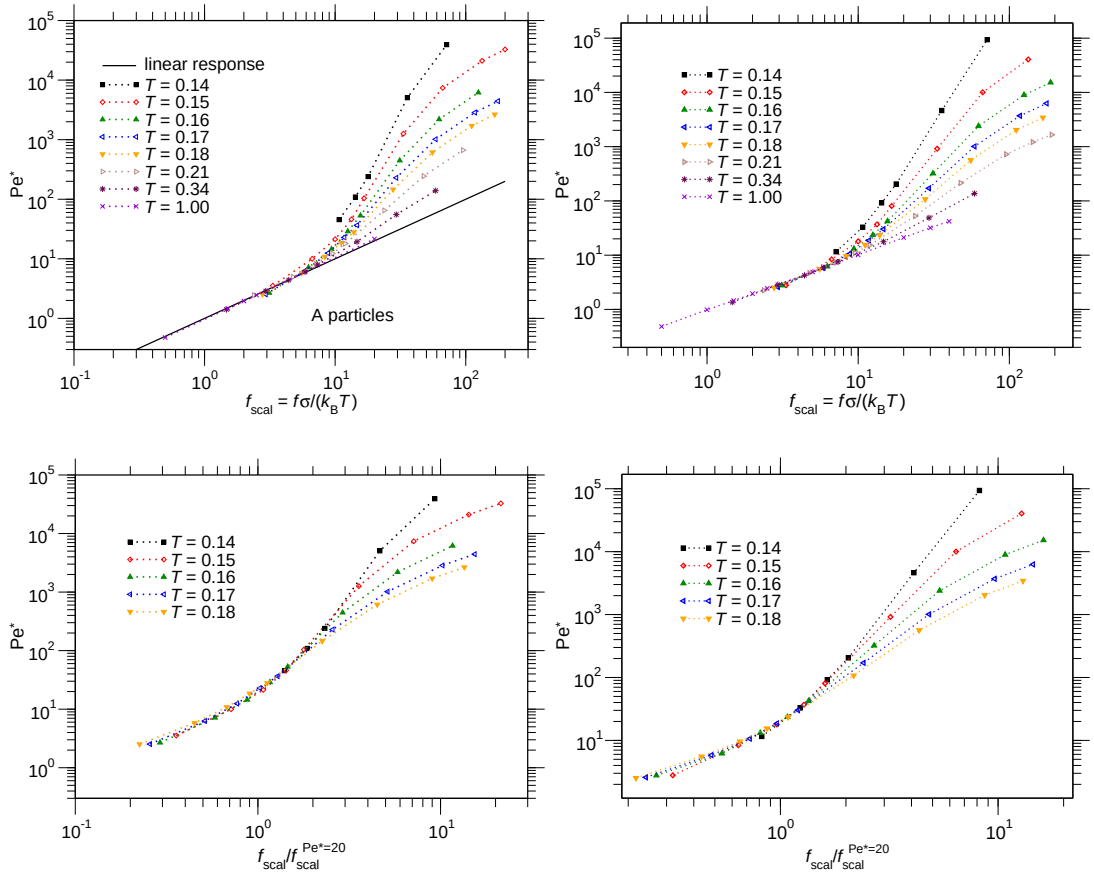

Figure 5.1 – Upper plots show Peclet numbers Pe^* against scaled forces f_{scal} for different temperatures T in dependence of the external force. Lower plots show the same data against rescaled forces $f_{\text{scal}}/f_{\text{scal}}^{Pe^*=20}$ to highlight the universal behavior. Left plots show A particles an right B particles.

the linear response region Pe^* in dependence of f_{scal} is just a straight line. In fig. 5.1 in the upper plots the calculated Peclet values against the scaled forces for both particle types are shown. At the highest temperature $T = 1.00$ the resulting curve is in good agreement with the linear response values for all forces and both particle types. But already for the next lower temperature one observes a slight deviation from the linear response values where the Peclet numbers increase superlinear at high forces. This effect increases with decreasing temperatures and shifts the linear response region to lower values. At the lowest temperature $T = 0.14$ the system completely falls out of the linear response region and therefore always shows a nonlinear behavior at the measured forces. It is found that the curves at intermediate forces can be rescaled and one finds a universal behavior of the Peclet numbers in the non-linear regime. To show this the forces were rescaled to $f_{\text{scal}}/f_{\text{scal}}^{Pe^*=20}$ with $f_{\text{scal}}^{Pe^*=20}$ the value of the force where $Pe^* = 20$ for the given temperature. This scaling is shown in the lower plots of fig. 5.1 for A and B particles separately and in fig. 5.2 for both together. In the

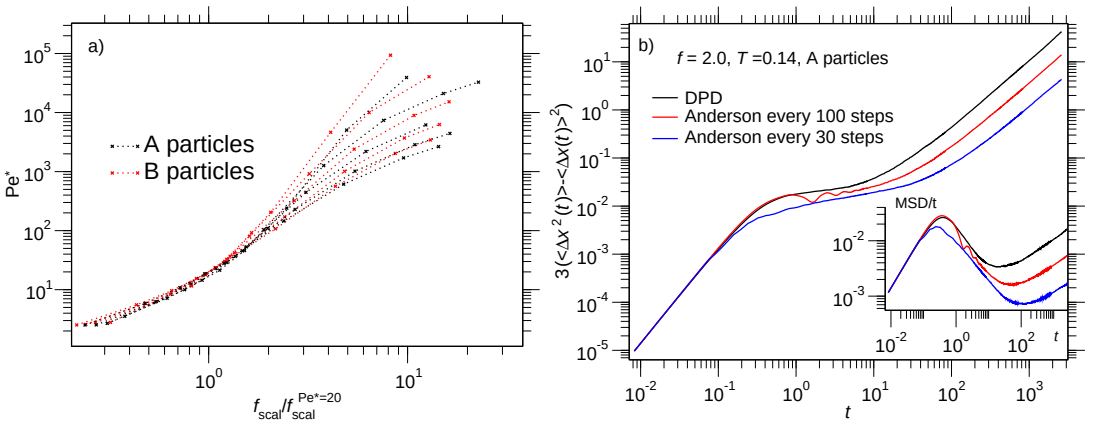

Figure 5.2 – a) Combined Peclet numbers Pe^* of A and B particles against rescaled forces $f_{\text{scal}}/f_{\text{scal}}^{Pe^*=20}$. b) Comparison of mean-squared displacement in force direction of A particles at $T = 0.14$ and $f = 2.0$. Black curves shows measurement with system cooled via the DPD thermostat, red curve via the Anderson thermostat every 100 steps and blue curve via the Anderson thermostat every 30 steps. Inset shows same curves divided through t.

region behind the linear response one finds a collapse of the scaled curves onto the same universal curve. The region over which the curves show this behavior increases with lower temperatures and therefore the scaling region increases in dependence of the temperature. At higher forces it is found that the curves deviate again from this scaling curve and show a strong temperature and force dependent behavior.

5.1.2 Diffusion behavior

In fig 4.6 of the previous chapter it was seen that in the parallel direction the motion of the pulled particles is superdiffusive for long times. There, the mean-squared displacement behaves as $\langle \Delta x^2(t) \rangle - \langle \Delta x(t) \rangle^2 \sim t^\alpha$ with an exponent $\alpha > 1$. One question that naturally arises from this observation is whether or not this behavior is the long time limit of the particle motion. One possibility is that the motion stays superdiffusive for all times which is predicted by the simple trap model. The other is that one observes a transition to a normal diffusive behavior for long times and the superdiffusive motion only occurs at intermediate times. That one would expect if the particle motion reaches the time scales of the bath diffusion. In fig 5.3 displayed are the mean squared displacements in the parallel direction at $T = 0.17$ and different forces for both particle types. Here, eventually a crossover to a diffusive behavior can be seen in the long time limit. Although this question cannot be answered with certainty. To highlight the long time behavior also the MSDs divided through the time are shown. These show even at long times a curvature and might converge against a constant plateau. Unfortunately, it is not easily possible to answer this question with certainty. Due

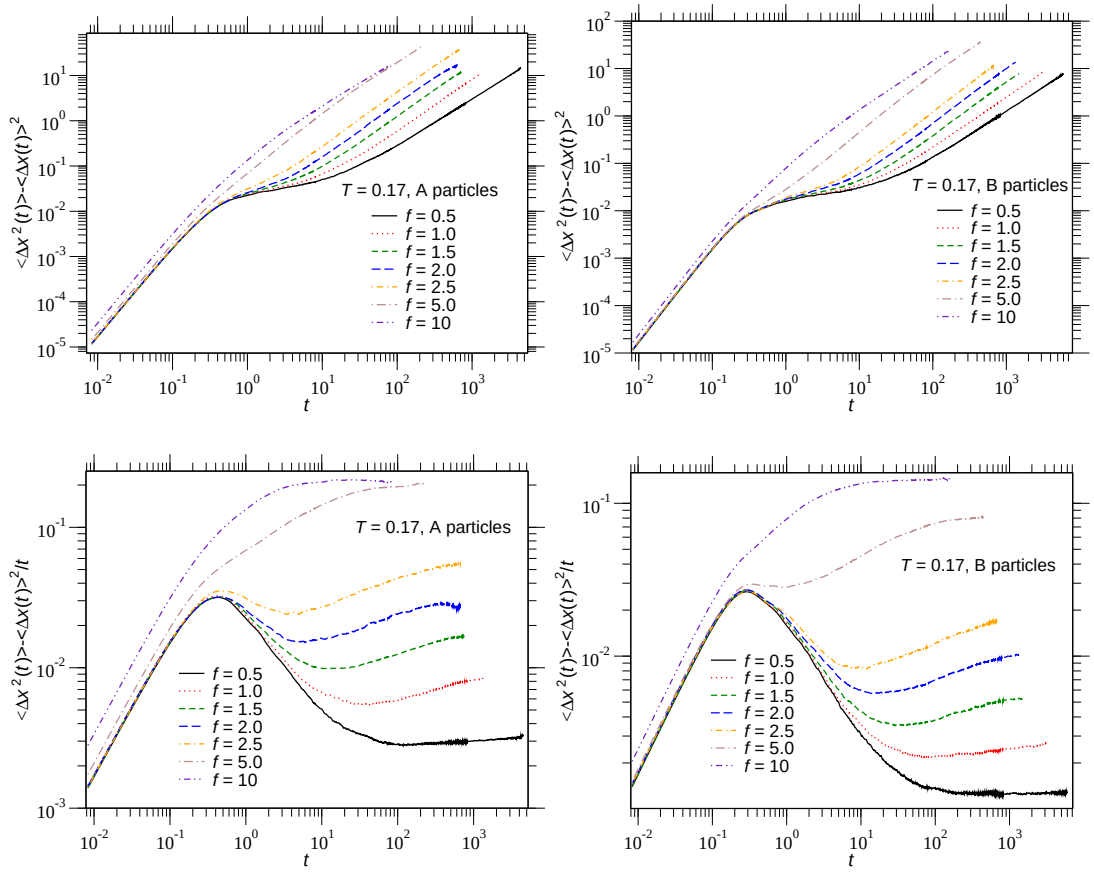

Figure 5.3 – Mean-squared displacement for the pulled particle in the force direction. Shown curves are for A (left) and B (right) particles for different forces at $T = 0.17$.

to the restrictions in the simulation time that result from the box length one cannot simply increase the observation time. An increase of the box sizes by an amount that would make a difference would result in an enormous additional computational effort. A second problem is the required statistics at these temperatures. The small deviations of the exponent α from unity lead to a bad signal to noise ratio. Therefore, it is difficult to differentiate the superdiffusive behavior in the long time limit from a normal diffusive behavior. It is also not practical to go to even lower temperatures that show a stronger superdiffusive behavior. There, it is found that the region over which the particles show superdiffusive motion at $T = 0.14$ is extended over up to 2 decades in time and even up to 3 decades in time in the glass at $T = 0.12$. Therefore, the possible transition to the diffusive regime is shifted to much later times and even longer simulations are required here. To check whether this long time behavior is influenced by hydrodynamic effects, which are increased by the DPD thermostat, some additional simulations were run with the Anderson thermostat. Due to the strong randomness introduced by this method hydrodynamic effects are suppressed. In fig. 5.2 b) a direct

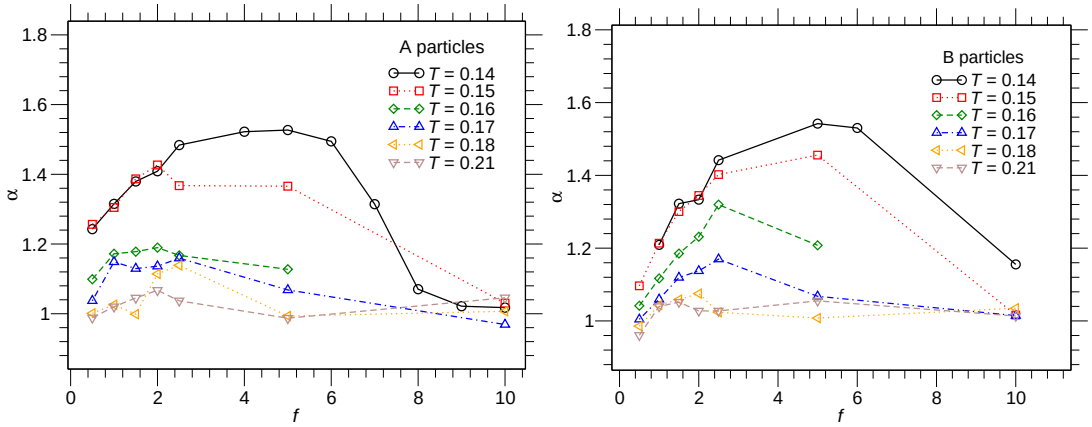

Figure 5.4 – Effective exponents α of the mean-squared displacements in the force direction with $\langle \Delta x^2(t) \rangle - \langle \Delta x(t) \rangle^2 \sim t^\alpha$ at different temperatures T in dependence of the external force f. Left plot shows A particles and right plot B particles.

comparison is shown and one finds that the long time behavior does not depend on the thermostat. Hence, one can conclude that the long time superdiffusive behavior is not influenced by hydrodynamic effects. From these simulation data it is possible to measure the exponent α in dependence of the force at different temperatures. This is done by fitting power laws against the long time limit of the MSDs. The obtained exponents are presented in fig.5.4 for both particle types. As one sees α deviates only slightly from unity at high temperatures up to $T = 0.18$ and only in the region of $f = 2$ where $\alpha \approx 1.1$. These small deviations make it hard to measure the effect of super-diffusion as the statistical fluctuations are quite large. By lowering the temperature closer to the glass transition one finds a steady increase of the exponents and a shift of the maximum of the curves to higher forces. At these temperatures one finds a steady, nearly linear, increase of α at small and intermediate forces, which corresponds to the universal behavior found in fig. 5.1. For higher forces these curves reach a plateau value, followed by a strong decrease to unity at even higher forces. Here, the transition to the diffusive regime takes place. For both particle types one observes that at the lowest temperatures the temperature dependence decreases and the curves seem too converge against a temperature independent behavior (especially at low forces) with a maximum at $f \approx 4-5$ with $\alpha \approx 1.5-1.6$. Although the simple trap model presented in chapter 3.2 showed a superdiffusive regime, the qualitative behavior differs from the one observed in the simulations. At low forces (3.33) predicts a linear increase with the force. This is in agreement with the simulation results presented here, although the statistics are not good enough and the slope of the increase is not 2. A clear difference in that region is the displacement behavior of the probe where the model predicts a creep motion with a power law behavior whereas here a normal linear displacement with constant velocity is observed. At higher forces a second regime is predicted (3.34) where the exponent α behaves as $2/\mu$. This could possibly describe the behavior found here although the

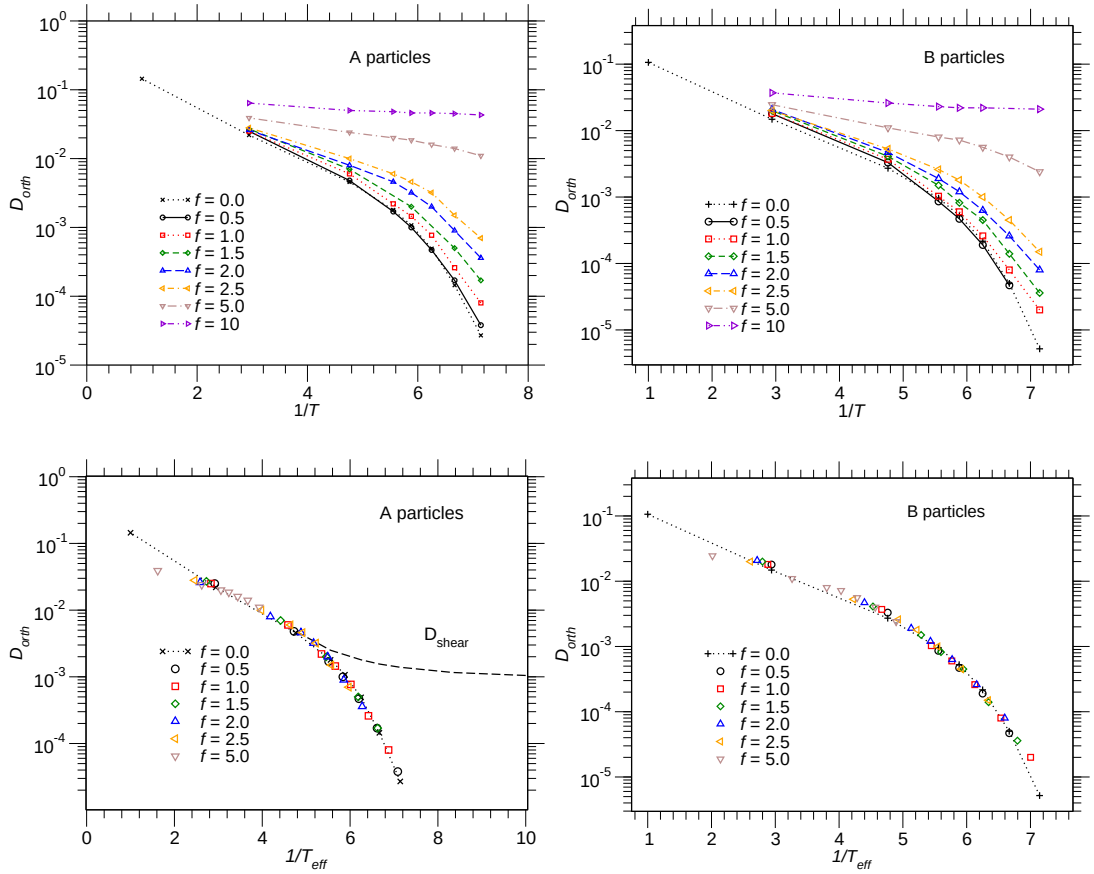

Figure 5.5 – Diffusion constant in the perpendicular direction D_{orth} of the pulled particles for different external forces. Upper plots show D_{orth} against inverse temperature $1/T$ and lower against inverse effective temperature $1/T_{\text{eff}}$ to highlight the collapse onto the equilibrium behavior. Left plots show A particles and right B particles.

statistic and the number of data points is definitely not good enough in that region. Then, at high forces the behavior agrees with the theoretical predictions (3.35) where one has a diffusive motion and a linear increasing displacement. Of course this simple model is only a rough description of the investigated system and therefore the comparison should not be overstretched. For a realistic description a more sophisticated model is required.

Although the diffusion constants in the force direction are not accessible in these simulation they can still be calculated in the perpendicular direction which was already shown in the previous chapter. For a better comparison with the equilibrium values and to highlight the effect of the external forces in fig 5.5 the diffusion constants for different f are plotted against the inverse temperature. As one can see, the equilibrium diffusion reduces drastically by orders of magnitude at lower temperatures close to T_c

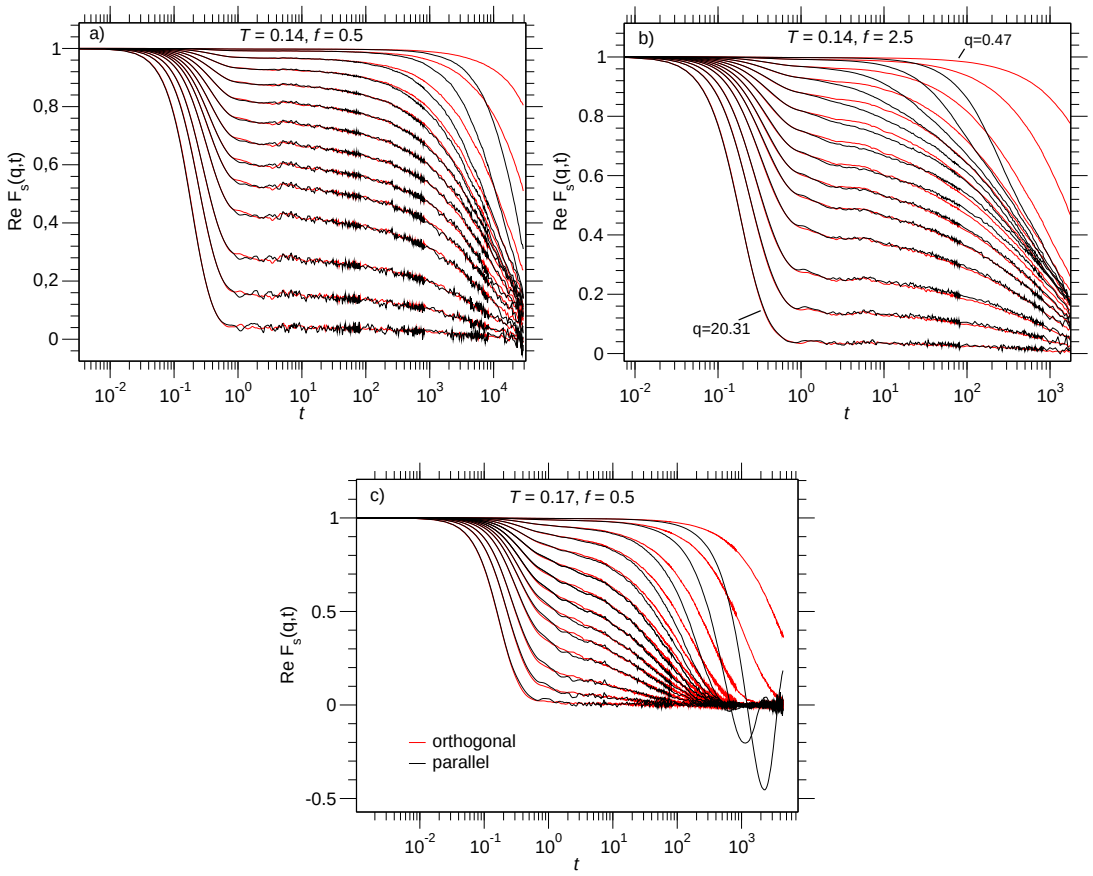

Figure 5.6 – Comparison of the real part of $F_s(q,t)$ for both directions at different temperatures and forces. Black curves show parallel and red curves perpendicular direction. Upper plots are at $T = 0.14$ with a) $f = 0.5$ and b) $f = 2.5$ for A particles, c) shows Re $F_s(q,t)$ at $T = 0.17$ and $f = 0.5$ for A particles. All plots show curves with $q = 0.47, 0.94, 1.89, 2.83, 3.78, 4.72, 5.67, 6.61, 7.56, 8.50, 9.92, 12.28, 15.12, 20.31$.

which is also predicted by the MCT (3.8). By applying an external force the diffusion increases and still shows the same strong temperature behavior as in equilibrium, but now with a shifted T_c. The particles behave as if they were at equilibrium but at another temperature. This observation directly leads to a definition of an effective temperature $T_{\text{eff}} = c(f)T$ which describes the behavior of the pulled particles. Here, T_{eff} only depends on a force dependent prefactor $c(f)$ and the system temperature T. That prefactor $c(f)$ can be calculated by superimposing the curves for the particles with external force onto the equilibrium curve which is shown in the lower plots of fig 5.5 where the same diffusion constants are plotted against these inverse effective temperatures. Here, one observes that for the lower temperatures all curves collapse nicely onto the equilibrium curve of the system. Only far away from T_c, at temperatures around $T_{\text{eff}} = 0.34 - 1.0$, a deviation for the highest forces can be observed.

This is in agreement with the previous results of the Peclet number where the scaling also broke down for high forces and temperatures. It corresponds to the absence of the super-diffusive motion and the influence of the cage structure on the particle motion.

Such a description with an effective temperature and the general temperature dependence of the diffusion differs drastically from the behavior under shear as was found in [5, 43]. To highlight the difference also the diffusive behavior of the particles in the same system under shear is shown (dashed line, data from [5]). In the sheared case only a slight temperature dependence is found. There, at high temperatures the system is in the linear-response region and the diffusion coefficient agrees with the equilibrium values. Then, at lower temperatures the system enters the non-linear region and one observes a converging behavior against a constant plateau. In the sheared case the whole system is deformed and the cages break up by the shear rate which leads to a nearly constant diffusion even far below T_c. There, the diffusive behavior is dominated by the timescale $1/\dot{\gamma}$ introduced by the shear rate $\dot{\gamma}$ whereas for a single pulled particle the surrounding does not change and one observes a motion of a particle in a frozen surrounding.

5.1.3 Incoherent scattering functions and relaxation times

The next system property under closer investigation for scaling relations and universal behavior is the incoherent scattering function $F_s(q,t)$ of the pulled particle. From the theoretical side it is an interesting property to study due to the many predictions the MCT makes about the typical behavior inside the different relaxation regimes. To study the anisotropic behavior of $F_s(q,t)$, both directions together for different forces and temperatures are shown in fig. 5.6. Here, the middle plots show $F_s(q,t)$ at $T = 0.14$ for $f = 0.5$ a) and $f = 2.5$ b). It is found that for high values of q the incoherent scattering function shows an identical behavior in both directions. Only for small q-values one observes a different behavior at intermediate and late times with a much faster decaying correlation function parallel to the force. In c) one sees, that at $T = 0.17$ and $f = 0.5$ for long times the correlation function in the parallel direction even starts to oscillate between positive and negative values at the lowest q values and has an imaginary part (not shown here). It seems that the difference between both directions starts to emerge with the onset of the α-relaxation. This can be checked by calculating the relation $R(t)$ (3.11) for the shown curves which was done in fig. 5.7 where $R(t)$ for $T = 0.14$ and $T = 0.17$ with $f = 0.5$ is shown. In both directions all curves collapse nicely onto each other during the β-relaxation regime. Only for long times, where the α-relaxation sets in, the curves deviate from each other. Here, the orthogonal direction shows a monotonous decrease whereas the parallel direction shows oscillatory behavior for low q and higher T values. Therefore, one can conclude that the factorization property predicted by the MCT (3.10) holds even under the influence of the external force in the scaling regime at low forces.

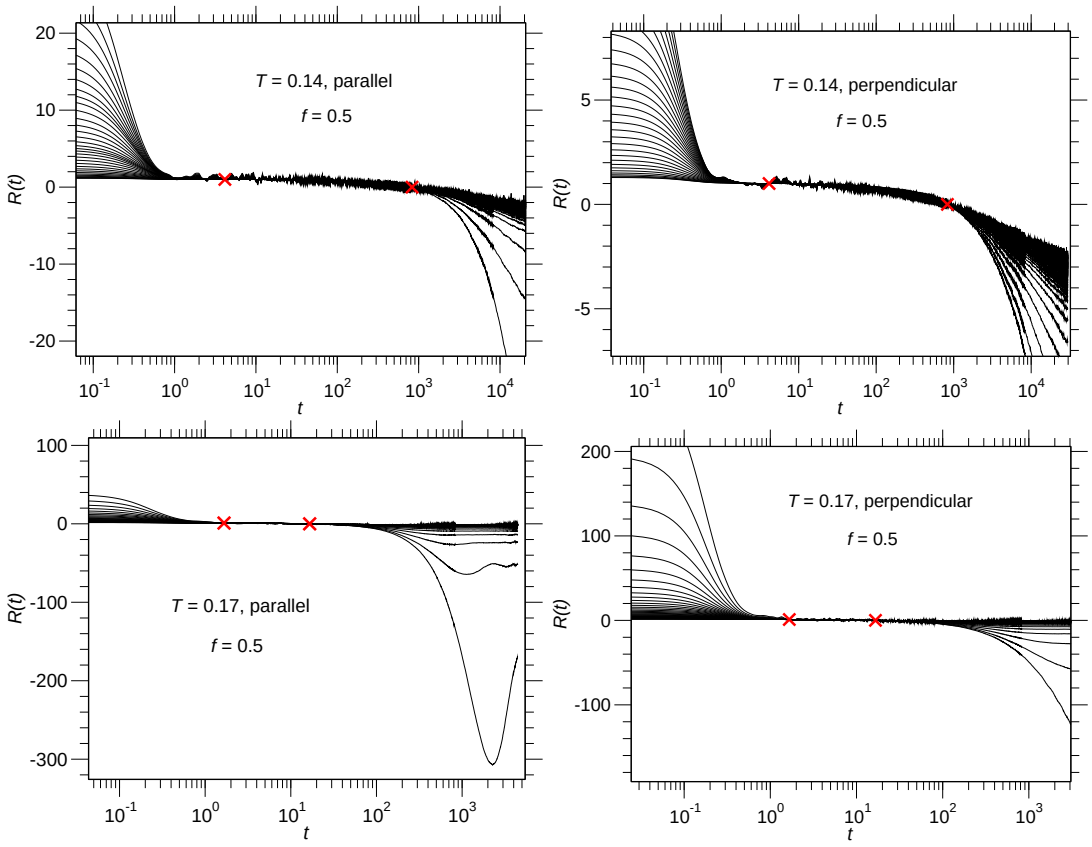

Figure 5.7 – Relation $R(t)$ of the incoherent scattering functions (shown in fig. 5.6) in dependence of the time for different values of q. Upper plots show $R(t)$ for $T = 0.14$ and $f = 0.5$, lower plots for $T = 0.17$ and $f = 0.5$, both for A particles. Left plots show direction parallel and right perpendicular to the force. On intermediate times, in the β-relaxation regime, a collapse onto the q-independent curve is observed.

The MCT predicts that $F_s(q,t)$ should behave according to (3.12) in the β-relaxation regime. From this behavior the non-ergodicity parameter $\tilde{f}_{\mathbf{q}}$ can be obtained after fitting (3.12) to the measured curves. Pictured in fig. 5.8 are the values of $\tilde{f}_{\mathbf{q}}$ in dependence of q where all these curves nicely collapse onto each other. This is an interesting observation as one can calculate a localization length $\bar{r}_{\mathrm{loc}}$ from them in the Gaussian approximation of the incoherent scattering function $F_s(q,t)$ [5]. There, the non-ergodicity parameter behaves as $\tilde{f}_{\mathbf{q}} = \exp\left(-\frac{1}{6}q^2\bar{r}^2_{\mathrm{loc}}\right)$. From the collapse of the curves with different external forces onto the equilibrium curve follows that $\bar{r}_{\mathrm{loc}}$ is the same under the influence of the external forces and agree with the calculated equilibrium values from [5] $\bar{r}^A_{\mathrm{loc}} = 0.22$ and $\bar{r}^B_{\mathrm{loc}} = 0.19$. Hence, the cage structure of the trapped particles is the same as in equilibrium and it is not strongly deformed by the force. Moreover the cages are still isotropic for the pulled particles. This is in agreement with the previous observations that the particle motion is nearly identical as long

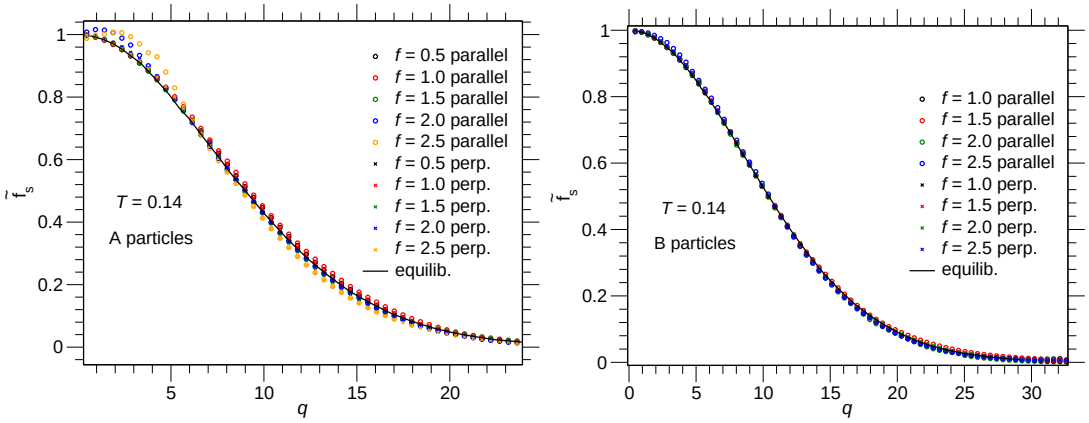

Figure 5.8 – Wave vector dependence of the non-ergodicy parameter $\tilde{f}_s$ of the pulled particles for A (left) and B (right) particles at $T = 0.14$ as obtained from the van Schweidler fits to the incoherent scattering functions. Different symbols correspond to the different directions and different colors to the different forces. Black straight lines are the equilibrium values from [5].

as the particles are trapped and differs only for the times after the particle has left the cage as was seen in fig.4.7 where the MSDs were compared.

For long times the second type of relaxation takes place, the α-relaxation. In the case of glassforming systems one usually finds a stretched exponential behavior (3.3) of the incoherent scattering functions. In this regime usually a universal time-temperature superposition principle holds. In the first plots of fig. 5.6 incoherent scattering functions of the probe for $f = 1.0$ and $q = 6.0$ at different temperatures in the range of $T = 0.34$ to $T = 0.14$ for the perpendicular direction are shown. For all except the lowest two temperatures the incoherent scattering function completely decays to zero during the time of the simulation. It is now predicted that the different curves should collapse onto each other for the late time regime after rescaling by the typical relaxation time τ_α. For each temperature this relaxation time is defined by

$$F_s(q, t = \tau_\alpha) = 0.2. \tag{5.2}$$

Thus, the relaxation time τ_α is the time where the incoherent scattering function has decayed to 0.2. Here, the chosen point is one of the lowest available values of $F_s(q,t)$ at $T = 0.14$. Note that due to the universality each point inside the scaling region is a valid rescaling point and therefore the relaxation time has no unique definition. In the right plot in the first row of fig. 5.6 this scaling for the discussed scattering functions has been carried through. As one can see the time-temperature superposition principle holds at low temperatures even with small and intermediate applied external forces as long as the particle is inside the scaling regime. It is found that the lowest temperature $T = 0.14$ already shows a small but systematic deviation from the time-temperature superposition principle. This is a first hint of other processes that take place close to

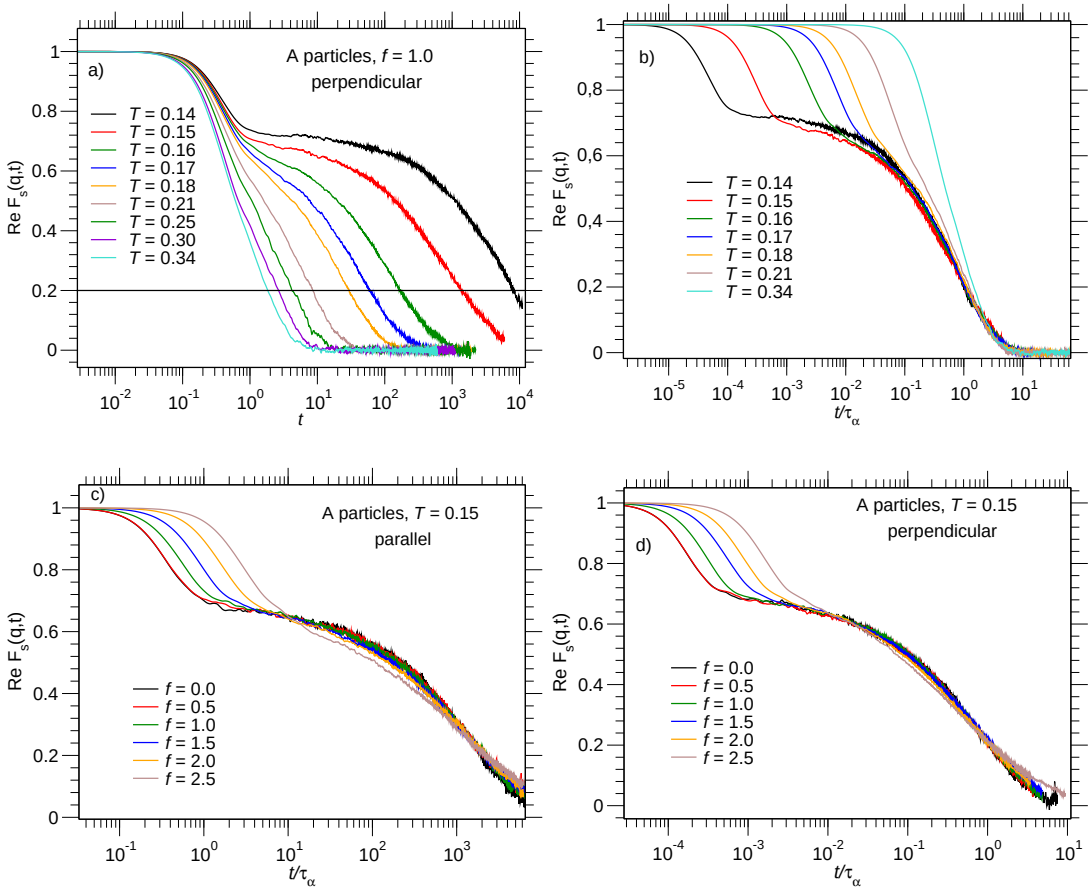

Figure 5.9 – Test of the scaling relations of the incoherent scattering functions $F_s(q,t)$. a) Shows incoherent scattering function $F_s(q,t)$ in perpendicular direction with $f = 1.0$ and $q = 6.0$ for different temperatures T. b) Shows same curves against rescaled time t/τ_α to illustrate the time temperature superposition principle around T_c. c) Illustration of the force time superposition principle in the parallel direction and d) in the perpendicular direction.

and below the critical temperature that are called hopping processes [19, 20]. Close to T_c these additional relaxation processes lead to deviations in the behavior from the MCT predictions. In the case of the pulled particle one has with the force f an additional free parameter and therefore one can check if a second superposition principle holds, the force time superposition principle. In fig. 5.6 c) and d) the scattering functions at $T = 0.15$ and different forces are scaled onto each other (unscaled data is shown in fig. 4.9 and 4.10). In both directions one finds that for small forces the curves collapse nicely onto each other during the α-relaxation regime. Only for the highest force $f = 2.5$ a slight deviation can be observed which comes from the oscillatory behavior in the parallel direction. Therefore, one can conclude that such a superposition principle holds. Thus, the exponents β of the stretched exponential decay (3.3) with

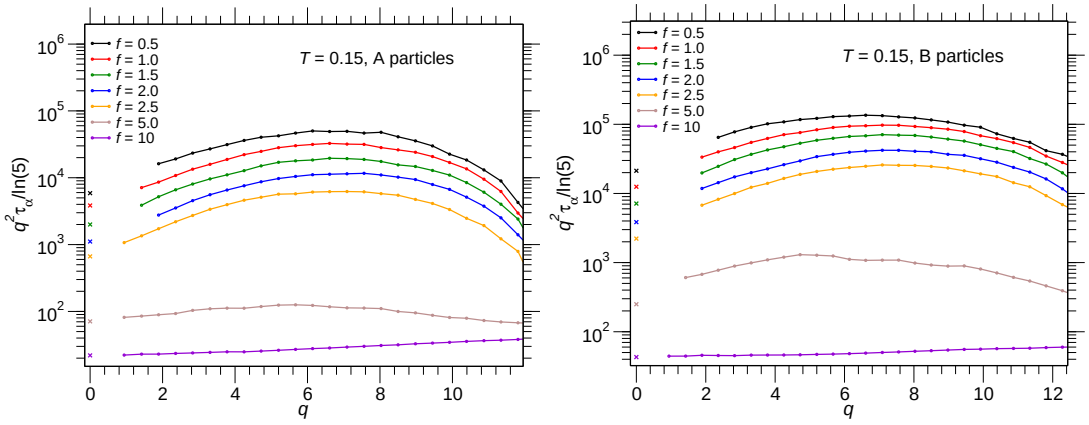

Figure 5.10 – Product of relaxation time τ_α and q^2 of the pulled particles for different external forces f at $T = 0.15$ in dependence of q. Left plot shows A and right plot B particles. Crosses at $x = 0$ mark the value of the inverse diffusion constants $1/D_{\text{orth}}$ ($\ln(5)$ as scaling factor is required for this comparison).

the applied force are the same as in equilibrium.

The last investigated property of the incoherent scattering shall be the relaxation time itself in the orthogonal direction. For different force at $T = 0.15$ in dependence of q the product of $q^2\tau_\alpha$ is shown in fig. 5.10. These curves increase with q until they reach a maximum around $q \approx 6-9$ with a decrease at higher q. With increasing forces one observes a strong decrease over orders of magnitude and a pronounced curved shape until the q dependence is only a linear increase at high forces. As in the equilibrium case [5] these curves can be compared to the diffusion constant D_{orth} as $F(q,t) = \exp\left(-D_{\text{orth}}q^2\tau_\alpha\right)$ holds in the hydrodynamic limit for small q. With $F_s(q, t = \tau_\alpha) = 0.2$ follows that $\tau_\alpha q^2/\ln 5 = 1/D_{\text{orth}}$. These values are marked with crosses in fig. 5.10 and one finds a good agreement with the extrapolated values. As a second point it is interesting to study the temperature dependence of τ_α. Here, one can check if a similar scaling relation with an effective temperature T_{eff} as for the diffusion constant (fig. 5.5) is found. Displayed in fig. 5.11 are the values of τ_α for $q = 6.0$ and different external forces in dependence of the temperature (upper plots). All curves show a diverging behavior in the region around T_c. Again, as in the diffusion case, the curves for higher forces diverge at lower temperatures. Thus, one can also scale these curves onto the equilibrium curve that was done in the lower plots. Here, in contrast to the scaling of the diffusion constant a systematic deviation from the scaling at low temperatures is observed. Therefore, this deviation might again be a result of additional relaxation processes that occur close to the critical temperature and lead to a deviation of the power law behavior. This effect was also observed in the equilibrium simulations in [5] where they lead to a stronger than predicted decrease of the relaxation time at the lowest temperature $T = 0.14$.

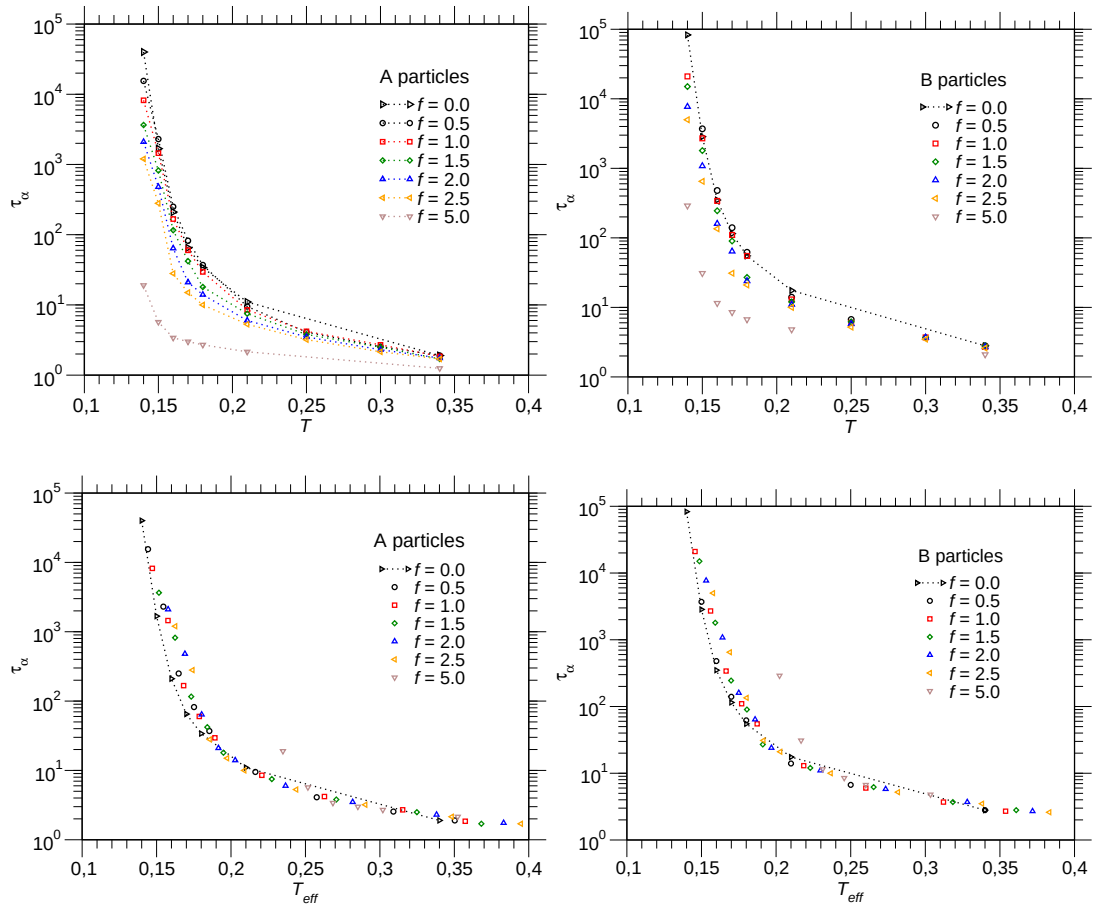

Figure 5.11 – Relaxation time τ_α of the pulled particles with different external forces for $q = 6.0$. Upper plots show τ_α against temperature T and lower against effective temperature T_{eff} to highlight the collapse onto the equilibrium behavior at higher temperatures. Left plots show A particles and right B particles.

5.1.4 Friction coefficient and effective temperature

Until now only the temperature dependence of two quantities in the perpendicular direction were investigated. Therefore, it is interesting to have a closer look at a quantity that also depends on the parallel direction, the friction coefficient. Displayed in fig. 5.12 is the temperature dependence of the friction coefficient ξ for a constant force. Close to T_c one observes a strong increase over orders of magnitude of ξ. As in the cases of the diffusion and relaxation constants the critical temperature for the curves with external forces is shifted to lower values of T and therefore these curves are all below the equilibrium curve. As can be seen in the middle plots of fig. 5.12, it is again possible to scale them onto the equilibrium curve by shifting. There, one finds a good agreement and a universal behavior over up to 3 decades in ξ for the scaled

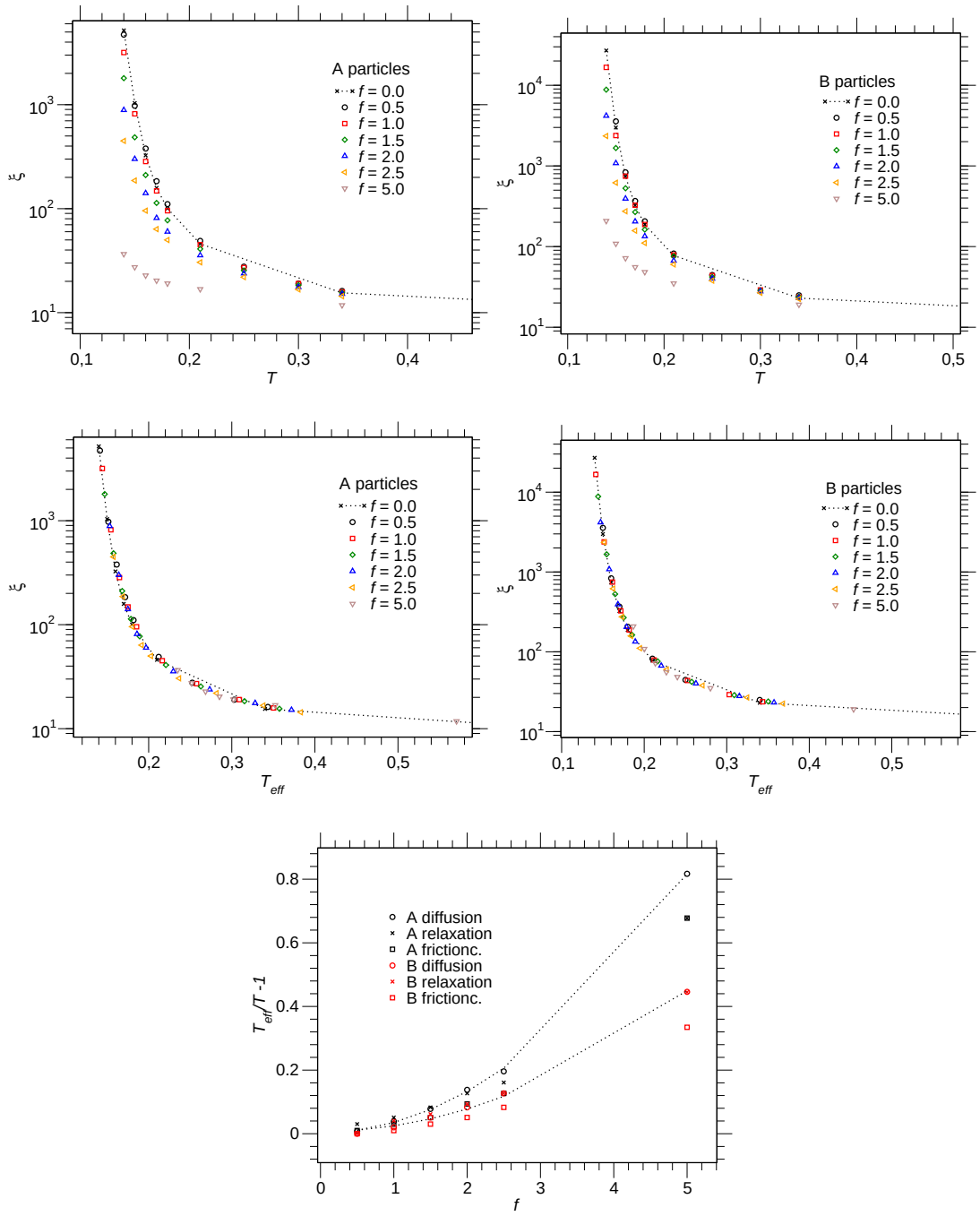

Figure 5.12 – Upper and middle plots show friction coefficient ξ of the pulled particles for different external forces. Upper plots show ξ against temperature T and middle plots against effective temperature T_{eff} to highlight the collapse onto the equilibrium behavior. Left plots show A particles and right B particles. Lowest plot shows obtained effective temperatures T_{eff} from the scaling plots for both particles types together. Here, the deviation in percentage $T_{\text{eff}}/T - 1$ is shown. Dotted lines show fit with $y = a + bf^2$ to the diffusion constant.

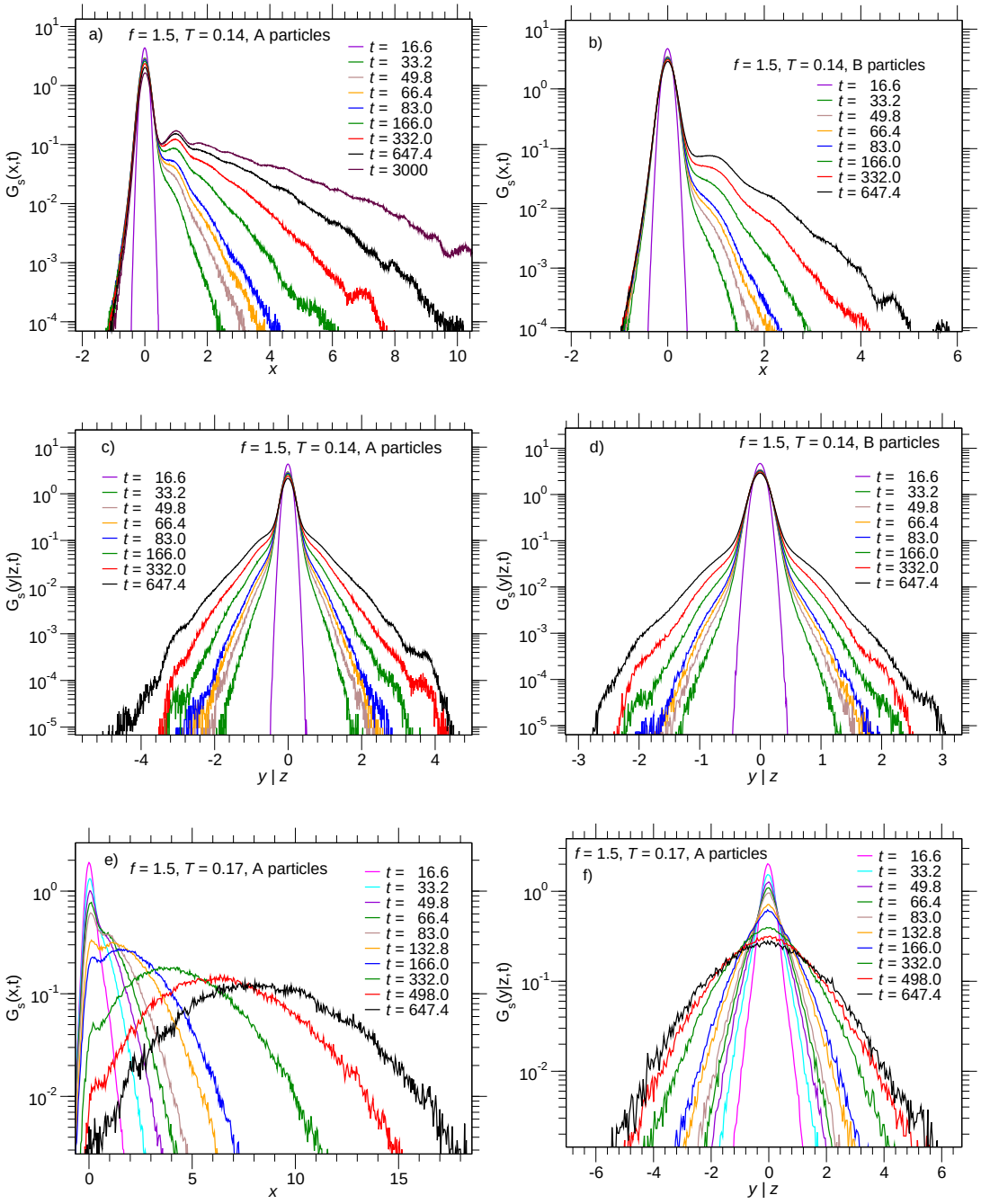

Figure 5.13 – Van Hove correlation functions of the pulled particles. Upper and middle plots show $G_s(\mathbf{r},t)$ at $T = 0.14$ and $f = 1.5$. Upper plots show parallel and lower perpendicular direction to the force for A (left) and B (right) particles. Lowest plots show $G_s(\mathbf{r},t)$ for A particles at $T = 0.17$ and $f = 1.5$ (left parallel and right perpendicular direction).

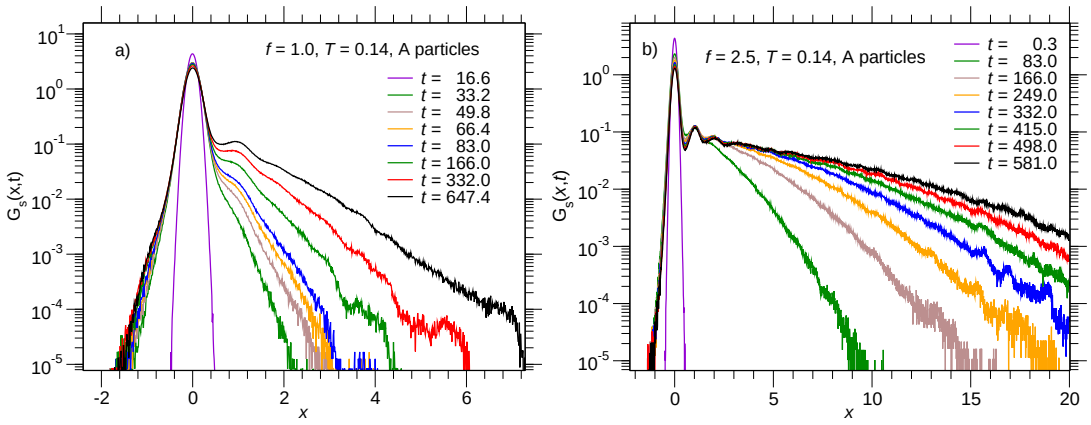

Figure 5.14 – Van Hove correlation functions in the parallel direction for pulled A particles at $T = 0.14$ for a) $f = 1.0$ and b) $f = 2.5$. Here, even a small third peak is visible.

curves against the effective temperature. Here, the quality of the scaling is again comparable with the diffusion scaling and thus the particle motion in both directions can universally be described with an effective temperature. From all these scaled plots it is directly possible to obtain the values of the effective temperatures. This leads to the interesting question if all these effective temperatures for the different properties are the same for the different quantities. To answer that question in the lowest plot of fig. 5.12 $T_{\text{eff}}/T - 1$ for all three measurements is shown. One finds that in all measurements the effect on the A particles is stronger and the values for the effective temperature lie therefore above the values of the B particles. For both particle types it is found that the values for the friction and the relaxation constant are in quite good agreement with each other except for the highest force of the A particles. But at this force it is questionable whether this scaling is still applicable. The values for the friction coefficient seem to lie all a bit below the values of the other quantities. But there the statistics is clearly not good enough to make any further statements about differences between these properties. It is found that the behavior of the diffusion constant can be described quite well with a simple $y = a + bf^2$ behavior as is shown with the dotted fit to both curves. This is in agreement with the predictions made in [65] from a mean-field theory for a Brownian particle with a strong external field where also a quadratic behavior was found.

5.2 Particle motion

In the last part of this chapter the movement of the particle shall be analyzed directly in the real space. Here, the first investigated property is the van Hove correlation function of the probe particle. In fig. 5.13 some van Hove correlation functions of the probe

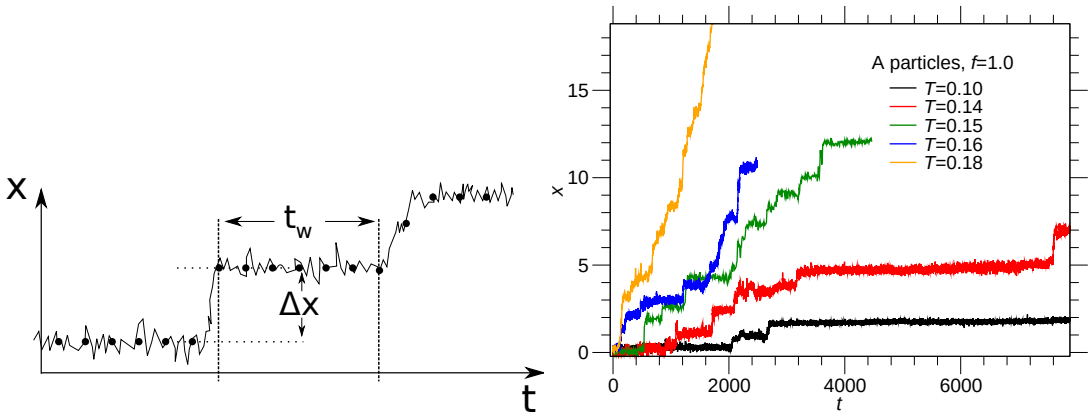

Figure 5.15 – Right) Schematic sketch of a typical pulled particle trajectory at low temperatures and forces. Here, t_w defines the time the particle is trapped inside the cage and Δx the jump distance of a single jump. Left figure shows typical trajectories for particles with $f = 1.0$ at different temperatures T.

particle are shown. In the direction perpendicular to the force one finds the typical behavior for a glassforming liquid where one has a symmetric distribution with a small Gaussian peak around $y, z = 0$. It indicates the trapped particles inside the cages and the broad exponential tails result from the non-diffusive motion on intermediate timescales. In the parallel direction the symmetry of the distribution is broken. There, also a Gaussian peak at $x = 0$ is found but only with a small exponential tail in the negative direction. In the positive direction one observes a smaller second peak followed by a broad and slowly decaying tails at longer times. As can be seen in a) this behavior can be observed for long times, where even at $t = 3000$ a strong peak at the initial position can be observed. At this time the average probe particle has moved $\approx 3\sigma$ at $T = 0.14$. Only for higher temperatures one can reach the regime where the peak disappears. This is shown in e) at $T = 0.17$ with $f = 1.5$. Here, one finds that the van Hove correlation function is nearly symmetric with a Gaussian shape around the average position at the longest times. This corresponds to the times where possibly a transition to a diffusive behavior can be observed in the MSDs of fig. 5.3. At the lower temperatures one has a motion of a particle in a frozen environment that can be seen from the peak structure in the force direction in fig. 5.14. The second small peak is at $x \approx 1$ that corresponds to the distance of the neighbor peak in the equilibrium pair correlation function. There, the particle moves with a high probability to the position of the nearest neighbor. For higher forces (here $f = 2.5$) even a third peak appears that indicates the next nearest neighbor positions.

At the lowest temperatures the particle motion is a nearly discrete motion with two separated parts. On the one hand one has long times at rest, where the particle is trapped inside the cage and on the other hand short jump moves from cage to cage. This beha-

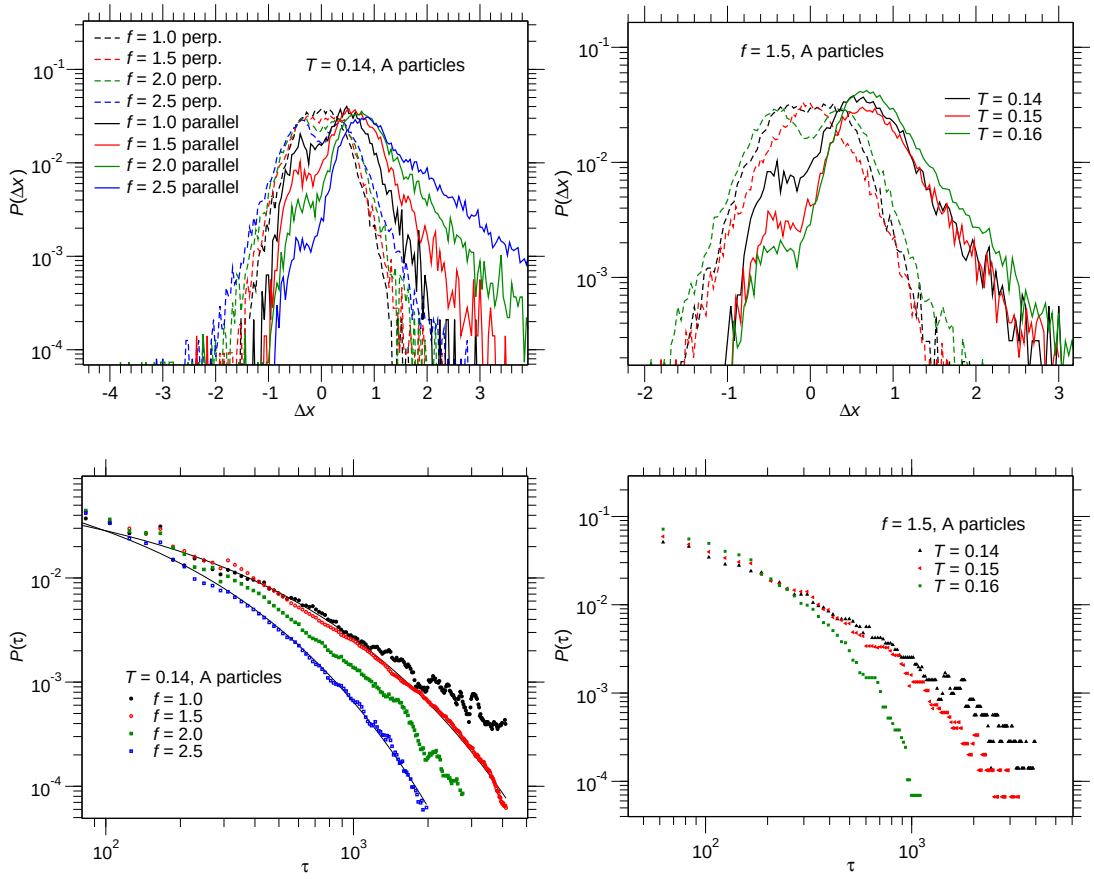

Figure 5.16 – Distribution of the jump distances $P(\Delta x)$ and the waiting times $P(\tau_w)$ of the particle motions for A particles. Left plots show distributions at $T = 0.14$ for different forces and left plots for $f = 1.5$ and different temperatures.

vior gets more and more pronounced for lower temperatures. In fig. 5.15 some typical trajectories (x-direction) at different temperatures with $f = 1.0$ are shown that highlight this behavior. Even at $T = 0.18$ one already sees that the particle gets slowed down from time to time by energy barriers in the system. With decreasing temperature the height of these barriers increases and the particles are trapped longer and more often. There, it is easy to differentiate between a trapped particle and a particle that jumps to the next cage. At the lowest temperature one has a nearly perfect separation between these two states. Hence one can study the probability distributions of the waiting times τ_w inside the cages and of the jump distances Δx from cage to cage. Here, this was done with the method that was used in [66]. There, the particle motion of a binary Lennard-Jones mixture in equilibrium was studied. In the presented cases the already recorded single particle trajectories were used. There, every 40 integration steps the positions and velocities were written out which were averaged over 20 con-

secutive steps to reduce the fluctuations. Only then it is possible to identify the single jumps and waiting times. To identify particle jumps from these averaged trajectories the distance $\Delta\bar{x}_i$ between two 20 steps separated positions is calculated and the average fluctuation $\sigma_{\text{est}} = \sqrt{1/N \sum_i \Delta\bar{x}_i^2}$ of these distances are measured (N number of measurements). Note that different to [66] σ_{est} is calculated from the average over all trajectories and not separately for every particle due to the much shorter simulation runs here. It is found that a good criteria for the identification of a particle jump at the lowest temperatures is $|\Delta\bar{x}_i|^2 > 10\sigma_{\text{est}}^2$. From these jumps the start and the end were identified by the threshold criteria $|\Delta\bar{x}_i|^2 > 3\sigma_{\text{est}}^2$. With these jumps identified the waiting times and jump distances can be measured. Here, the jump distance is the difference in the position between the beginning and the end of the jump and the waiting time is the time from the end of a jump to the beginning of the next jump. The parts at the beginning and the end of the simulation were discarded as the steps are not completed (usually the particle is trapped here). In fig. 5.16 the calculated distributions of the jump distances $P(\Delta x)$ and the waiting times $P(\tau_{\text{w}})$ are shown. It is found that the distribution of the jump distances shows an exponential decay in the positive direction and that the distribution of the waiting times shows a broad behavior that can be fitted by a stretched exponential (straight line) with an exponent $\beta \approx 0.5$. This behavior with a broad distribution of waiting times is principally in agreement with the simple trap model of chapter 3.2.

5.3 Summary

In this chapter the regime at intermediate forces in the steady-state was investigated closer. In that regime the particle motion shows a strongly anisotropic behavior and in the parallel direction the motion is superdiffusive. Here, a scaling behavior is found where the properties of the pulled particles show a universal behavior. It could be seen that the diffusion constants, the relaxation times and the friction coefficients of the particle under the influence of the external force can be scaled onto the equilibrium curves of the system. This leads to a description of the particle motion with an effective temperature. Furthermore, it was checked if the general predictions that are made by the MCT still hold for the pulled particle and it was found that the incoherent scattering functions show a time temperature and a force temperature superposition principle. At the end of this chapter the jump motion of the particles was investigate and the distribution of waiting times and jump distances was measured. Here, a broad distribution of waiting times was found which is in agreement with the assumption that are made for the simple trap model.

Chapter 6

High force diffusive Regime

The second regime investigated here in detail is the one at high forces. In chapter 4 it was found that at high forces the particle motion changes again from the superdiffusive motion at intermediate forces to a completely diffusive motion in the parallel direction at high forces. In this chapter that transition is studied in detail and it is found that with increasing force the anisotropy of the particle motion is reduced until it is again completely isotropic for the highest forces. Here, the reduced interaction of the probe particle with the energy landscape of the system (especially with the deep minima) at high external forces leads to that behavior. Furthermore, it is found that still deep in the high force regime a temperature dependence of the diffusion constant exists which is in contrast to the temperature independent behavior of the velocities and friction coefficients.

6.1 Transition to the diffusive regime

In fig. 6.1 the transition from the intermediate force regime to the high force regime for the mean-squared displacement of the particle motion for A particles at $T = 0.14$ is shown. There, one finds a strong dependence on the force as long as the particle motion is influenced by the cages in the system. This effect of the cages is indicated by the onset of the plateau in the MSDs. For higher forces one first observes a disappearing plateau and then a strong reduction of the effective exponent in the long time behavior. A second observation that can be made is that as long as the plateau is visible, the short time behavior is identical for the different forces. At higher forces this regime is shifted to higher values and therefore the local temperature of the probe is increased. For both particle types it can be observed that these effects always occur at the same force. So it seems that the cooling effect of the DPD thermostat is increased by the trapping of the particles. For better visualization of the long time behavior in the lower plot of fig. 6.1 the same MSDs divided by the time are shown.

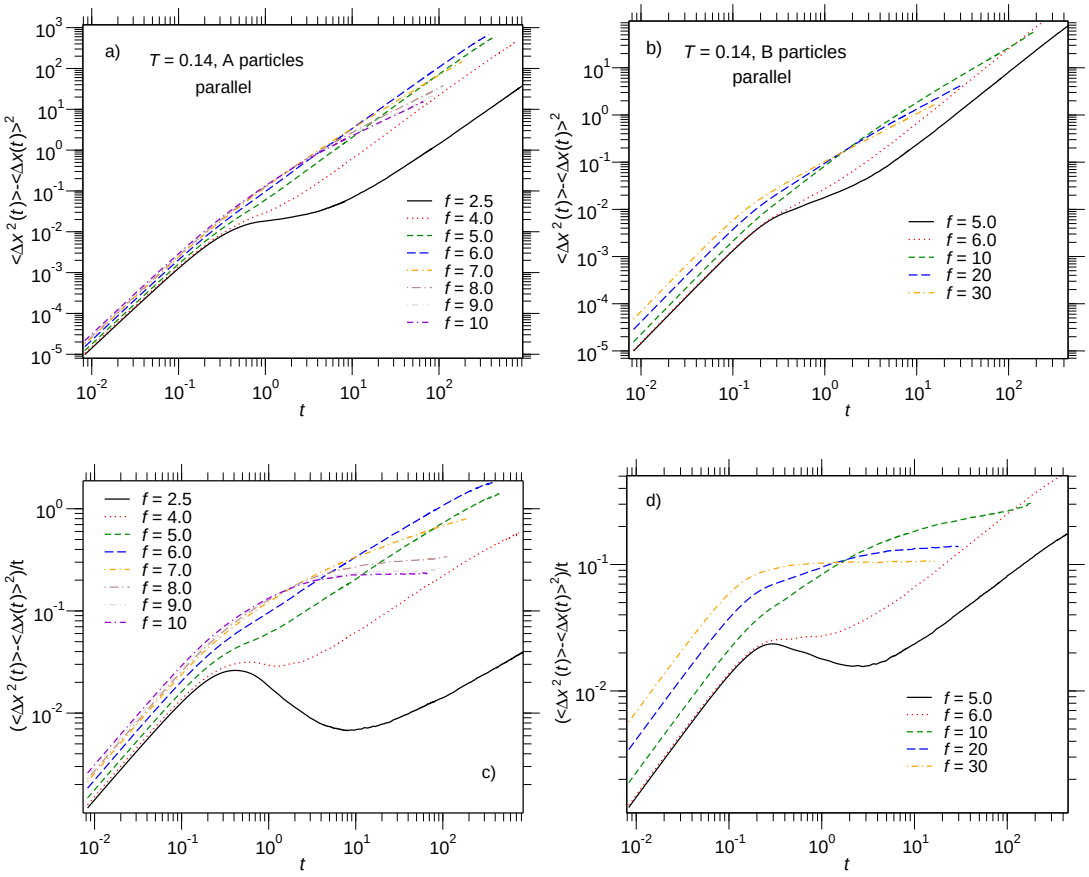

Figure 6.1 – Upper plots show mean-squared displacement at $T = 0.14$ in the parallel direction for a) A and b) B particles at intermediate and higher forces f. Lower plots show the same curves divided through t to highlight the transition to the diffusive regime at high forces.

A second property that is closely related to the MSDs is the velocity autocorrelation function $C_{\mathbf{v}}(t)$. It measures how strong the fluctuations in the velocity are correlated in time. For the pulled probe with a drift they are given by

$$C_{\mathbf{v}}(t) = \Big\langle [\mathbf{v}(0) - \overline{\mathbf{v}}][\mathbf{v}(t) - \overline{\mathbf{v}}] \Big\rangle = \Big\langle \mathbf{v}(0)\mathbf{v}(t) \Big\rangle - \overline{\mathbf{v}}^2. \tag{6.1}$$

Here, the average drift velocity $\overline{\mathbf{v}}$ is subtracted. Of course in the perpendicular directions the average velocity is zero and therefore one obtains here

$$C_{v_y}(t) = \Big\langle v_y(0)v_y(t) \Big\rangle \quad \text{and} \quad C_{v_z}(t) = \Big\langle v_z(0)v_z(t) \Big\rangle. \tag{6.2}$$

Only for the parallel direction the drift has to be taken into account

$$C_{v_x}(t) = \Big\langle v_x(0)v_x(t) \Big\rangle - \overline{v_x}^2. \tag{6.3}$$

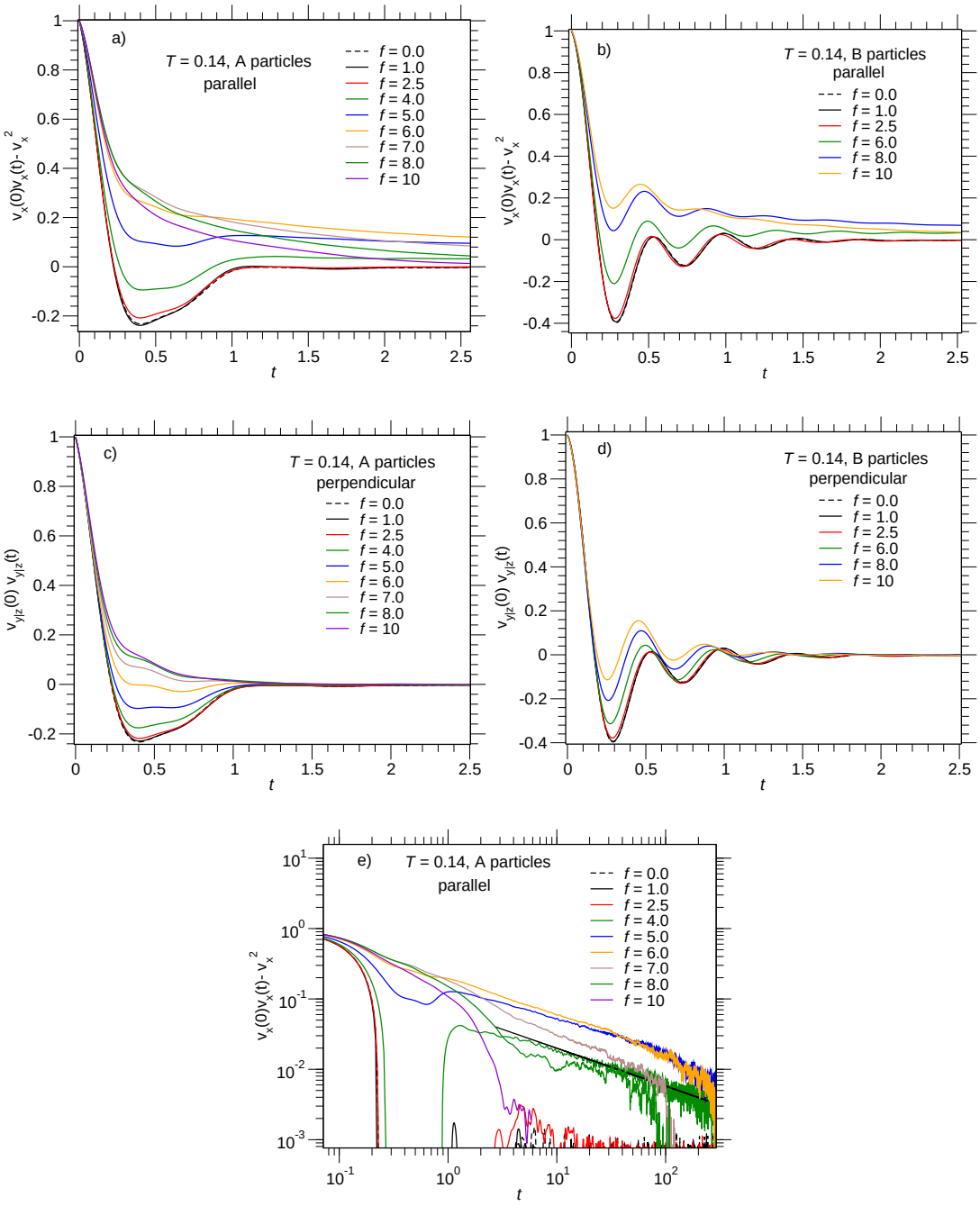

Figure 6.2 – Velocity autocorrelation functions of the pulled particles at $T = 0.14$ in dependence of the external force. Upper plots show direction parallel to the force and middle plots perpendicular direction. e) shows the same data as a) but on a log-log scale to highlight the long-time tales of the velocity autocorrelation function. Black dashed line is a power-law fit with the exponent $\alpha' = -0.53 \pm 0.05$.

In fig. 6.2 some of these correlation functions for $T = 0.14$ are shown. As one can see at the lowest forces the velocity autocorrelation function is still quite similar to the equilibrium curve (dashed black line). There, one observes a strong drop for short times of the correlation function and it even becomes negative. This the a result of the surrounding cage structure that traps the probe and acts in the opposite direction. Therefore, it comes to a reverted motion, the particle is pushed back and trapped. At higher forces the particles can detach more and more from the cage structure and the motion shows less influence of the surrounding particles. Hence, the velocity autocorrelation function is shifted to higher values and the backward motion is less pronounced. In the perpendicular direction c) and d) the decay to zero happens quite fast at all forces and for both particle types. This is in contrast to the parallel direction where at intermediate forces a long time tail can be observed which is shown in e) on a logarithmic scale. Here, one finds that for the forces in the range of $f = 4 - 8$ the velocity autocorrelation function shows a power law decay at long times over up to two decades in time. This behavior increases with the forces until it reaches a maximum at $f = 5 - 6$. For even higher forces this effect decreases again and it changes to an exponential decay at the highest forces. This power law decay is directly related to the superdiffusive motion observed in the MSDs [35] by

$$\begin{aligned}\left\langle \Delta r^2(t) \right\rangle &= \left\langle \int_0^t \tilde{\mathbf{v}}(t')\, \mathrm{d}t' \int_0^t \tilde{\mathbf{v}}(t'')\, \mathrm{d}t'' \right\rangle \\ &= 2\int_0^t \int_0^{t'} \left\langle \tilde{\mathbf{v}}(0)\tilde{\mathbf{v}}(t'-t'') \right\rangle \mathrm{d}t''\mathrm{d}t',\end{aligned} \tag{6.4}$$

with $\tilde{\mathbf{v}}(t) = \mathbf{v}(t) - \bar{\mathbf{v}}$ one has the direct relation between $\left\langle \Delta r^2(t) \right\rangle$ and $C_{\mathbf{v}}(t)$. Due to the bad statistics at long times this exponent can only be checked for the higher forces. At $f = 4.0$ the exponent $\alpha' = -0.53 \pm 0.05$ of the velocity autocorrelation function is measured which is in agreement with the obtained exponent $\alpha = \alpha' + 2 = 1.52 \pm 0.05$ of the MSD at that force.

This change in the decay behavior can also be seen in the incoherent scattering functions $F_s(q,t)$ which are shown in fig. 6.3 for A particles at $T = 0.14$. There, one observes in the perpendicular direction a transition from the decay at low forces, with a plateau at intermediate times and a stretched exponential decay at long times, to a completely Gaussian decay at high forces. In the perpendicular direction one finds that at $f = 4.0$ the curvature of $F_s(q,t)$ disappears completely and one has a behavior $F_s(q,t) \sim -log(t)$ over nearly 3 decades in time. At even higher forces the curvature changes in the opposite direction and one finds a behavior that resembles the behavior of scattering functions in the Lorentz gas as was shown in [67]. There, one first has a fast decay of the relaxation function and then a crossover to a slow decay at long times which is found for the forces $f = 5$ and $f = 6$ in the perpendicular direction. It is clear, that in the case of the pulled probe the reason for this relaxation behavior differs

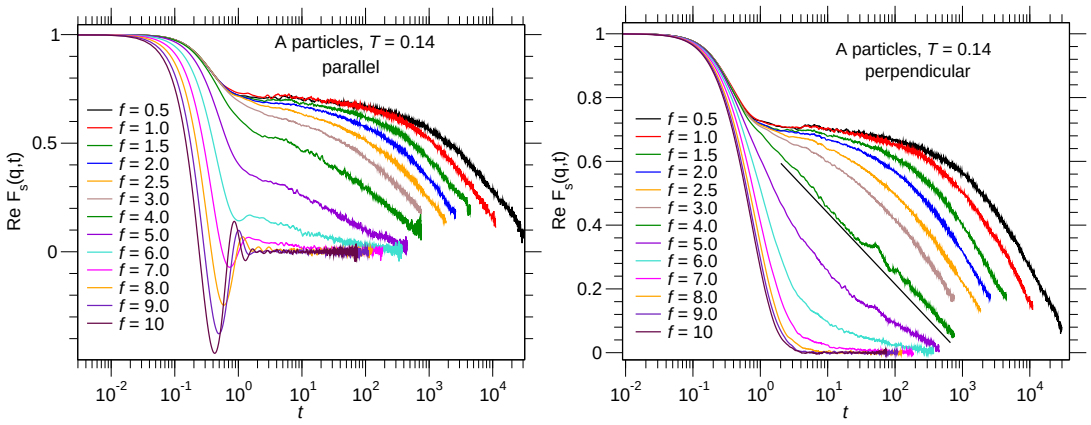

Figure 6.3 – Intermediate incoherent scattering function $F_s(q,t)$ at $T = 0.14$ and $q = 6.14$ of pulled A particles in dependence of f. a) shows parallel and b) perpendicular direction. For high forces the relaxation mechanism changes.

from the one in the Lorentz gas where the particles are localized inside pockets of a frozen structure. In the parallel direction the drift of the particles leads to an oscillatory behavior at high forces. At intermediate forces one observes a slow transition from one relaxation behavior to the other with a slowly disappearing plateau, coming from the low forces. In fig. 6.4 the q-dependence of $F_s(q,t)$ in both directions for some selected forces are shown. As one can see, the general behavior depends on the value of q. For lower forces the oscillatory behavior is shifted to lower values of q.

In fig. 6.5 the corresponding van Hove correlation functions of the probe particles for the same forces are shown. Here, one finds that in the parallel direction the shape becomes more and more Gaussian with increasing forces. At the intermediate forces the distribution of the probe probability shows a two peak structure with a narrow but strong peak at $x = 0$ and a broad second peak peak at higher x. Such a behavior was also observed for a pulled probe in a triangular lattice gas in [17, 68]. In contrast to these previous results, here a broad tail of this second peak to lower x is found and the peaks clearly deviate from a Gaussian distribution. Only at the highest forces the first peak disappears completely and the shape of the van Hove correlation function is Gaussian for all times. From a comparison with the behavior at high temperatures follows that these long tails result from the cage structure as they disappear at higher temperatures even for small forces. This can be seen in fig. 5.13 e). In the perpendicular direction one observes a transition from the typical shape with the broad exponential tails and a strong localization at $x = 0$ to a completely Gaussian behavior.

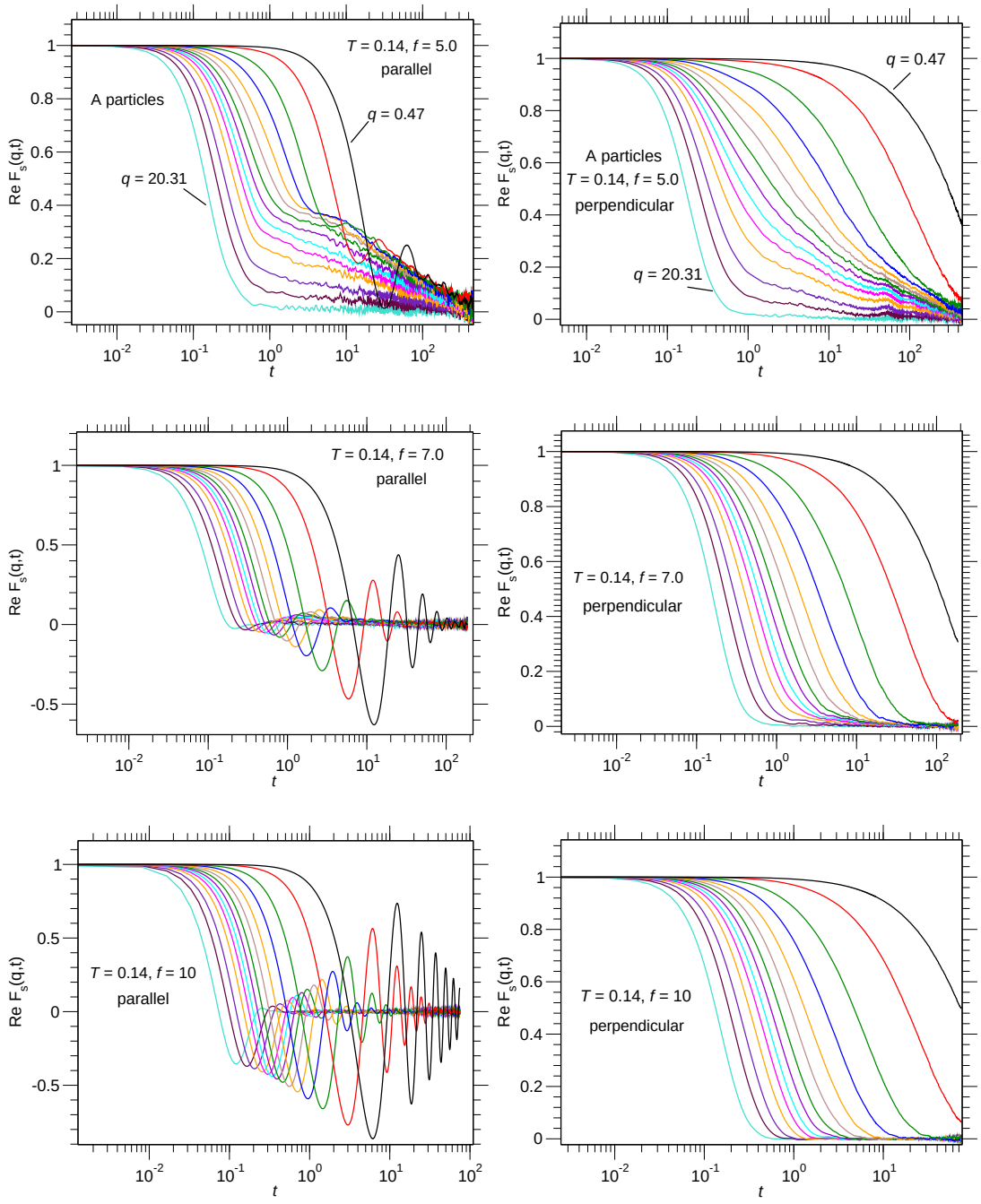

Figure 6.4 – Intermediate incoherent scattering function $F_s(q,t)$ at $T = 0.14$ of pulled A particles and different f. Left plots show parallel and right plots perpendicular direction. All plots show $F_s(q,t)$ with $q = 0.47, 0.94, 1.89, 2.83, 3.78, 4.72, 5.67, 6.61, 7.56, 8.50, 9.92, 12.28, 15.12$ and 20.31.

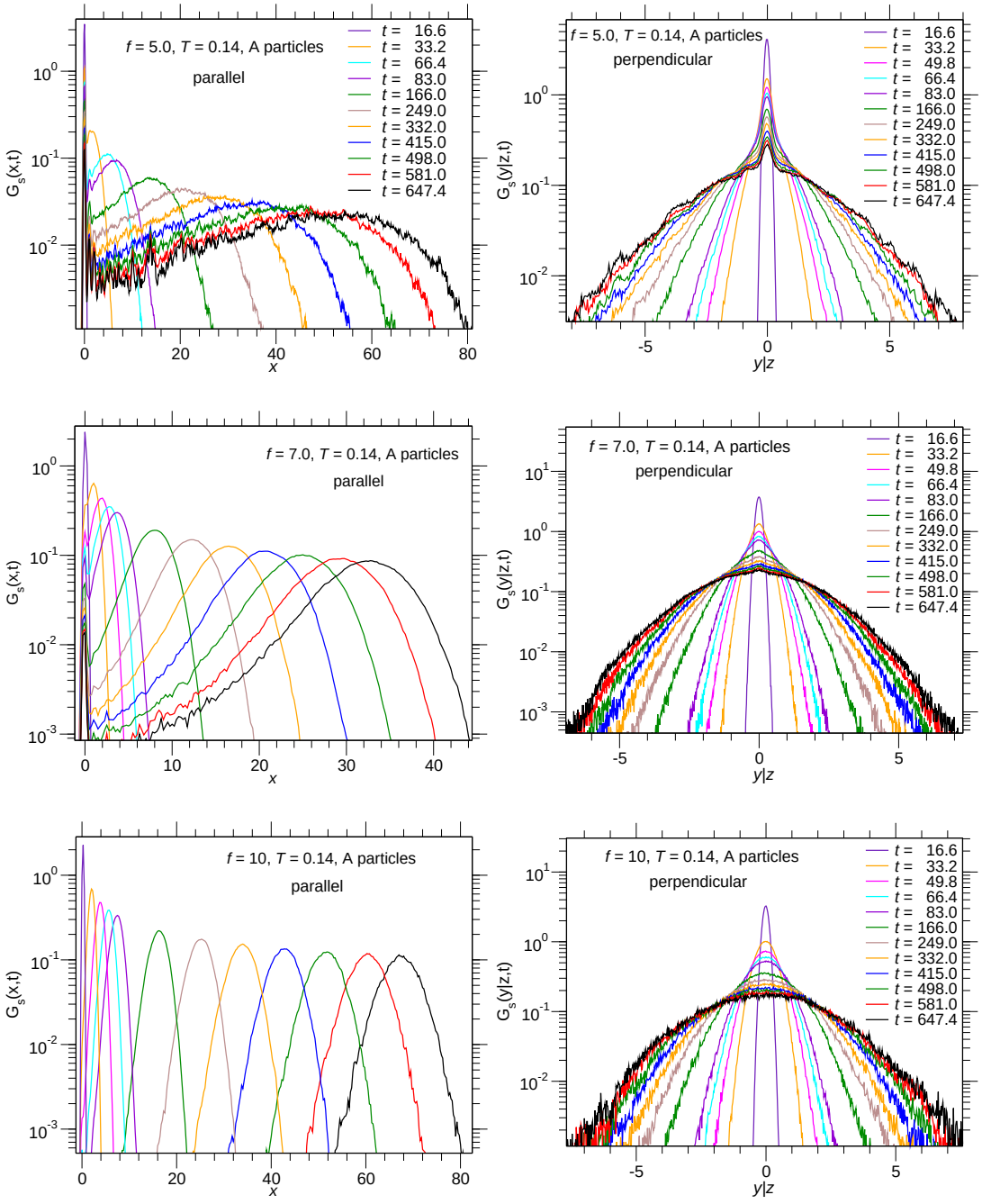

Figure 6.5 – Self-part of the van Hove correlation function $G_s(\mathbf{r}, t)$ of the probe particle at $T = 0.14$ for different external forces. Left plots show direction parallel and right perpendicular to the force at the same times t and forces f.

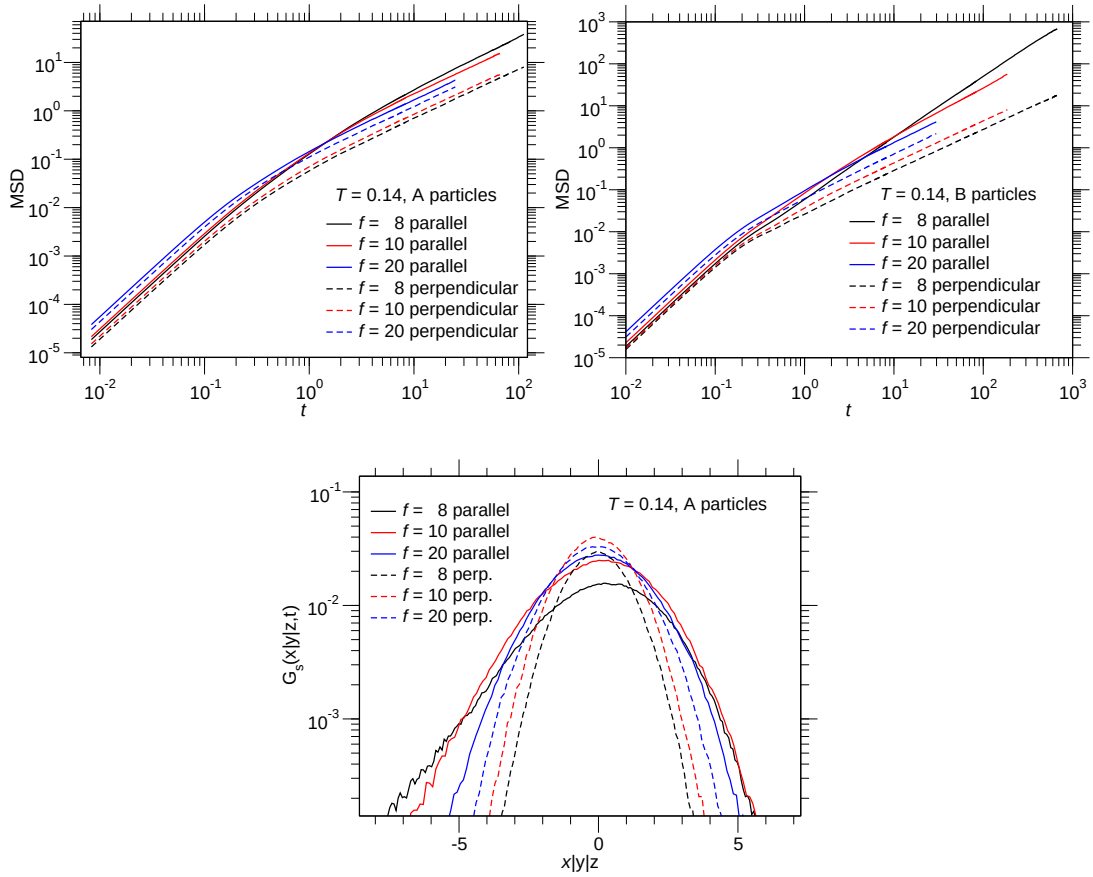

Figure 6.6 – Upper plots show the mean squared displacements of the probe in both directions at $T = 0.14$ with $f = 8, 10, 20$ for A (left) and B (right) particles. Lower plot shows the self part of the van Hove correlation function for both directions at the same forces of A particles. Here, the distribution in the parallel direction was shifted by the average value, to make both curves comparable. At high forces a strong reduction of the anisotropy of the particle motion can be observed.

6.2 The diffusive regime

For high forces the particle motion is diffusive again and the van Hove correlation function has a similar shape in both directions. Therefore, it makes sense to compare the two particle directions directly with each other and check how strong the anisotropy in this region is. Pictured in fig. 6.6 in the upper plots are the MSDs in both directions together for the highest forces at $T = 0.14$. For both particle types one finds that the direction parallel (straight lines) and the direction orthogonal (dashed lines) converge against each other with increasing forces. This can also be seen by directly comparing the van Hove correlation functions of both directions as is shown in the lowest plot of fig. 6.6. There, for reasons of better comparison $G_s(x,t)$ was shifted by the average

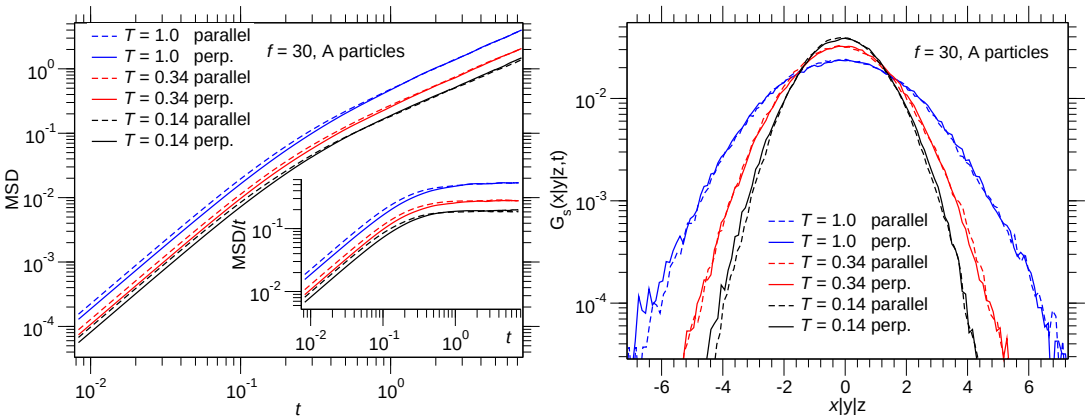

Figure 6.7 – Temperature dependence of the behavior in the high force regime. Left plot shows MSDs in both directions and right corresponding van Hove correlation functions at $T = 0.14, 0.34, 1.0$ for $f = 30$.

particle position.

The measurement of the friction coefficient showed that the particle motion in the high force regime is independent of the system temperature. Therefore, one would also expect that the diffusion shows a temperature independent behavior as well. To check this prediction in fig. 6.7 the MSDs for A particles and $f = 30$ at different temperatures are shown. At all temperatures one finds a clear difference between both directions at short times but no direction dependence in the diffusive long time limit. Surprisingly even at these extremely high forces a temperature dependence in the diffusion constant exist, as can be seen in the inset. This temperature dependence can also nicely be seen in the van Hove correlation function that is shown in the right plot of fig. 6.7. This quantity gives exactly the same picture. No anisotropy any more but still a strong temperature dependence which is a clear difference to the behavior of the friction coefficient.

One of the remaining questions that needs to be answered is to what extend the DPD thermostat influences the particle motion, especially in the high force regime. This thermostat introduces an additional friction term into the equations of motion and therefore it could be possible that the particle behavior at high forces is strongly influenced from it. Thus, some measurements were run at the lowest temperature where the thermostat was completely switched off. The resulting simulations were therefore performed completely micro-canonically. As a consequence the whole system energy during the simulations with the pulled particle was not constant as the external force constantly increases the system energy. This leads to a slowly increasing temperature with the time. In the upper plots of fig. 6.8 selected displacements and MSDs in the force direction for A particles at $T = 0.14$ are shown. For all forces one finds that the displacements with and without the thermostat are in good agreement and therefore no effect is visible. As a consequence also the friction coefficient is not influenced by the DPD thermostat. Also the comparison of the MSDs shows a good agreement with

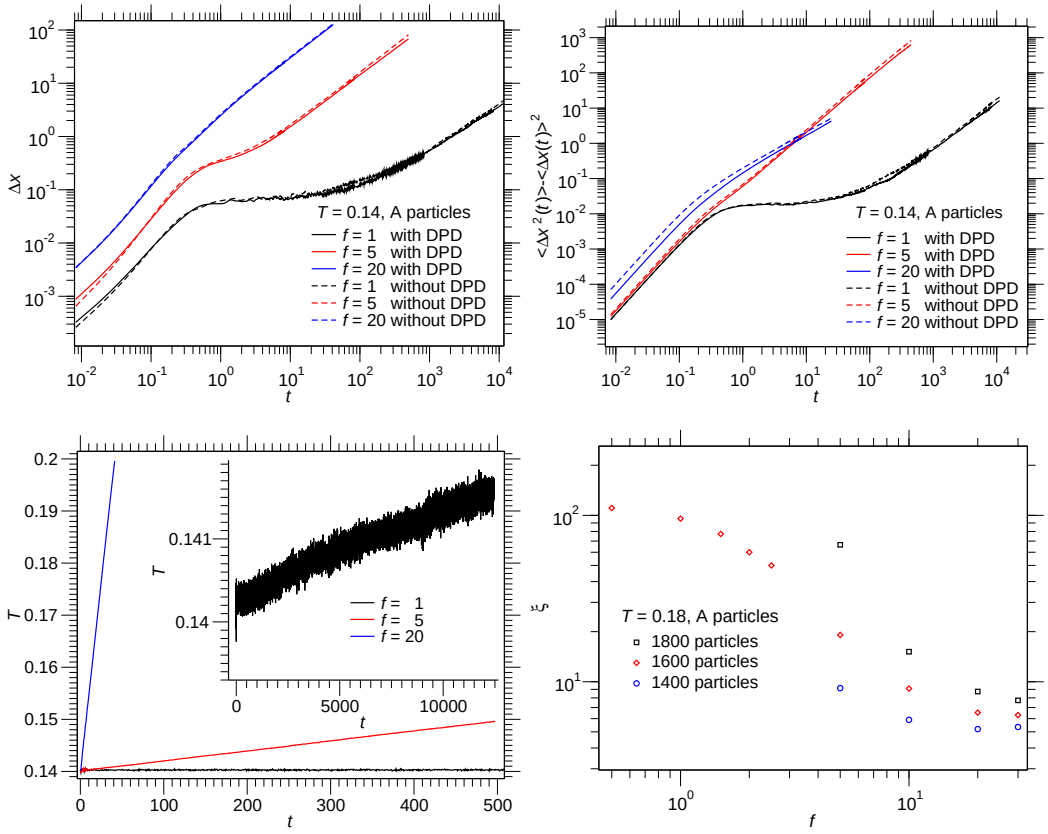

Figure 6.8 – Upper plots show direct comparison of displacements (left) and mean squared displacements in the parallel direction (right) of the probe particles with and without the DPD thermostat and lower left plot the corresponding temperatures in the systems without thermostat. Shown curves are at $T = 0.14$ with $f = 1, 5, 20$ for A particles. Lower right plot shows density dependence of the high force plateau at $T = 0.18$. There, red symbols corresponds to the mainly used density with 1600 particles in a box of geometry $L_x = L_y = L_z = L$, blue to 1400 and black to 1800 particles.

only slight deviations in the short time regime at the highest force. There, the ballistic regime from the simulations without the thermostat is shifted to slightly higher values as the local temperature of the pulled particles is increased even more without the DPD thermostat. Just to highlight the effect of the missing thermostat on the system temperature the development of the temperature with the time of these simulations without the thermostat is shown in fig. 6.8. There can be seen that the forces $f = 5$ and $f = 20$ lead to a strong increase of the system temperature whereas the drift for the smallest force $f = 1.0$ can only be seen in the inset.

As a last point in this chapter it shall be checked if the high force plateau is density dependent that has been found in previous works [54, 56]. Therefore, the number of particles were changed and new system configurations at $T = 0.18$ were equilibrated. At this temperature the relaxation times are still not too large but the system already

exhibits slow dynamics. For a better comparison systems with two different densities were used. One slightly less dense system with 1400 particles (700 of each type) and one with a slightly higher density 1800 particles (900 of each type) per subbox of size $L_x = L_y = L_z = L$. With these equilibrated configurations new measurement runs with applied external forces in the high force regime were done. The calculated friction coefficient from these simulations are pictured in the lowest plot of fig.6.8 where one can see the value of the high force plateau shows a clear density dependence and it is shifted to higher values for higher densities. This is in agreement with the results published in previous works [54, 56].

6.3 Summary

In this chapter the behavior at high forces was investigated and it was shown that the anisotropy of the particle motion reduces for higher forces where it is diffusive again on the accessible time scales. In this regime the incoherent scattering function and the van Hove correlation functions were investigated and it was found that the latter showed even for relatively high forces a double peak structure. In addition the high force regime was investigated where, in contrast to the friction coefficient, the diffusion showed still a strong temperature dependence at the highest forces. Furthermore, the influence of the DPD thermostat and the density of the system on the particle motion were analyzed. With this chapter the part on the steady-state motion in the liquid is completed. In the next section the behavior after the switch-on and switch-off is investigated and then a closer look at the behavior of the particle in the glass state is taken.

Chapter 7

Switch on, switch off and the glass state

The previous chapters concentrated on the classification of the probe particles in the different steady state regimes. Up to now all the presented results were obtained in the steady state at temperatures above T_c in the liquid phase. On the other hand the MCT presented in chapter 3.17 makes predictions for the transient dynamics. Thus, for a direct comparison with the theoretical predictions one also needs to study the transition behavior into the steady state. Furthermore, studying this case helps to understand the behavior at temperatures below the glass transition where the motion of the particles drastically slows down. At these temperatures the behavior after the switch on of the force is pronounced and influences some observables for a long time. Here, the interesting questions that arise are at what time the particle is in the steady state and furthermore for what forces does it reach a steady state with a nonzero velocity.

7.1 Switch-on and switch-off

The first investigated case is the switch-on case where the particle is initially at rest at $t = 0$. With the beginning of the simulation the constant external force f is switched on and leads to an acceleration of the probe. At low temperatures and high forces, where the particle is out of the linear response regime, one expects a non-linear response. To measure this behavior a much better statistics at short times is required compared to the previous simulations. Here, no self averaging over time is possible and therefore only short simulation runs are practical where around 80000 repetitions of the particle motions over 1500 steps are recorded. At low temperatures one observes a strong increase of the velocity directly after the switch-on of the force which is shown in the first plots of fig. 7.1. Directly after the switch on the first increase is proportional to the applied force and linear in time. It reaches a maximum at around $t = 0.25$ then followed by a

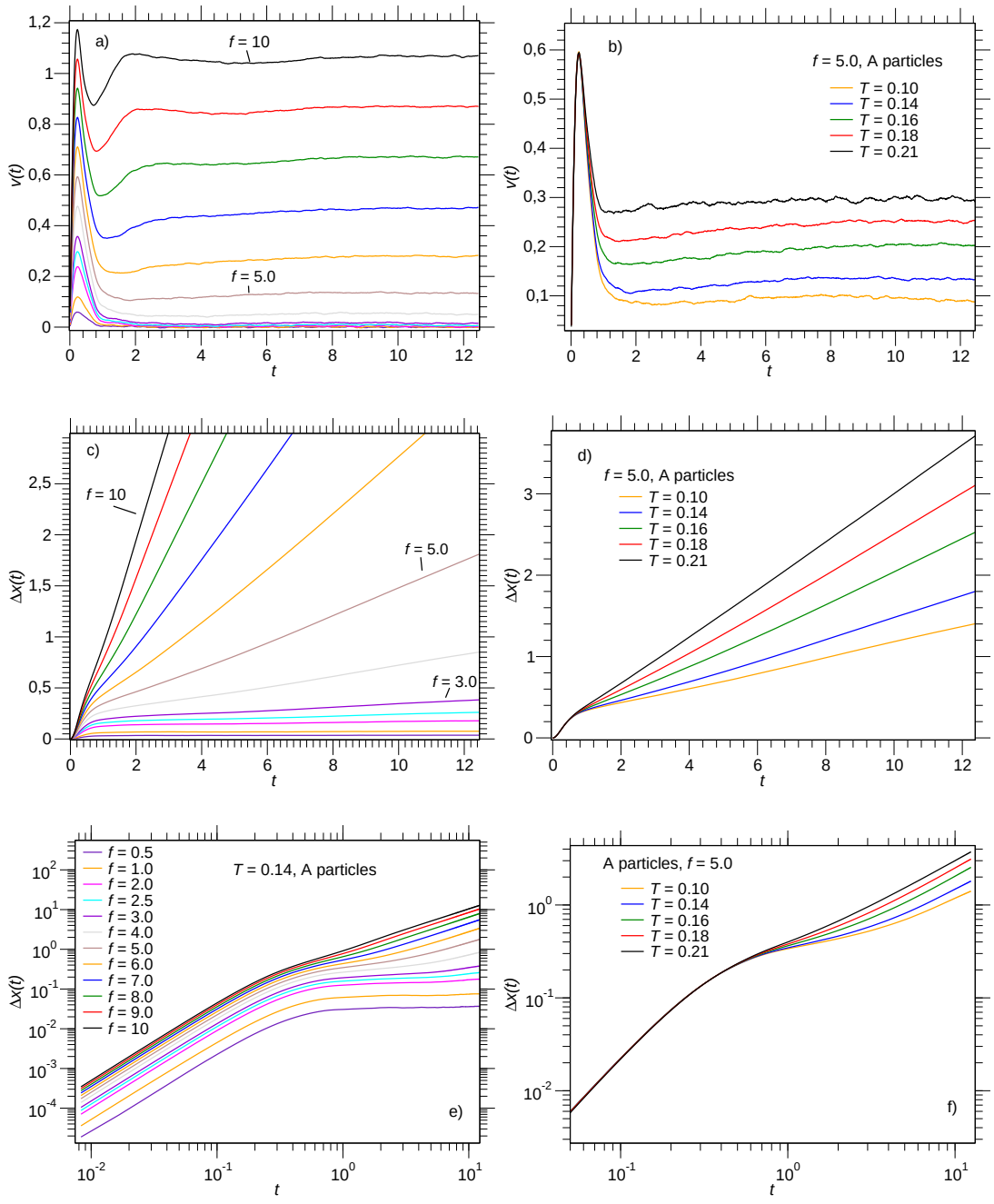

Figure 7.1 – Behavior of the pulled A particles after switching on the external field. First plots show the velocity in dependence of time, middle and lower plots show the particle displacement (linear scale and on log-log scale). Left plots show the behavior at $T = 0.14$ for different forces and right plot for $f = 5.0$ and different temperatures.

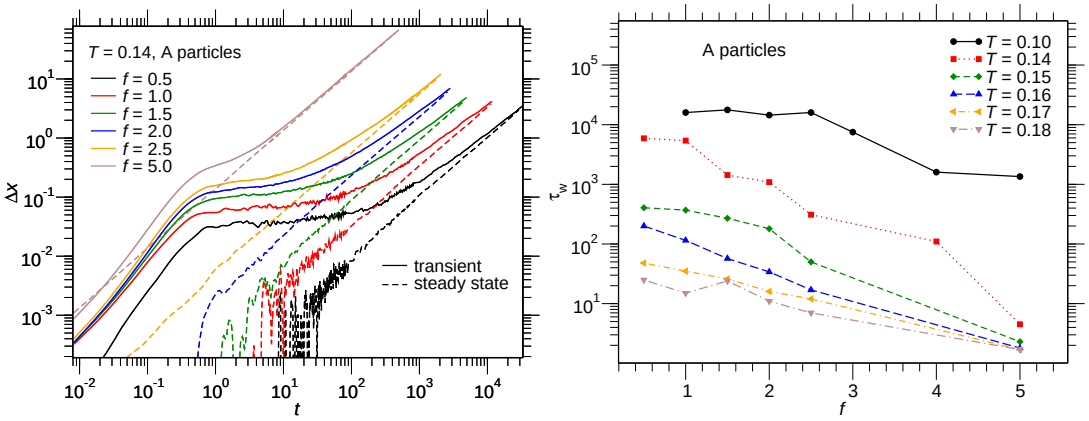

Figure 7.2 – Left plot shows displacements of A particles at $T = 0.14$ and different forces (straight lines show transient behavior and dashed lines steady state behavior). Right plot shows time until the particle has approximately reached the steady state from the transient measurements (criteria is the time from where on the deviation between transient and steady state curve is less than 25%).

strong decrease which results from the influence of the surrounding particles that lead to a constant friction and therefore to a reduction of the probe velocity. Interestingly, one does not observe a monotonous decrease to the steady state velocity from here on. At low temperatures and high forces a dip to velocity below the steady state value is found and only from there the velocity increases to the steady state value. At the highest force $f = 10$ at $T = 0.14$ one even finds a second smaller dip in the velocity. In the middle and lower plots of fig. 7.1 the displacements for the same particles are shown. At the first sight the displacements shown in e) and f) on the log-log scale look quite similar to the mean squared displacement in the steady state with a quadratic behavior at short times, a plateau at intermediate and a linear increase at long times. But here in contrast to the MSD measurement, where it is the steady state behavior, it is a transient behavior. If the displacements are measured in the steady state they only show a linear increase with time. This can be seen in fig. 7.2, where the displacements from the long simulation runs are shown. From this comparison one can extract a timescale that describes how long it takes until the particle has reached the steady state after the switch on. Here, this point is defined as the time from where on the difference between both curves is less than 25%. As one can see, this timescale increases strongly with lower temperatures and shows an exponential increase at low forces. Therefore, the transient behavior of the displacements gives a false perspective on the dynamics of the probe particles. Hence, from the velocities one sees that the particles reach the steady state quite fast at around $t = 10$ which is a few decades faster. Thus, the plateau in the transient measurement of the displacement is a consequence of the velocity overshoot at short times after the switch on. For low temperatures the height of this overshoot, compared to the steady state velocity, increases strongly and therefore the

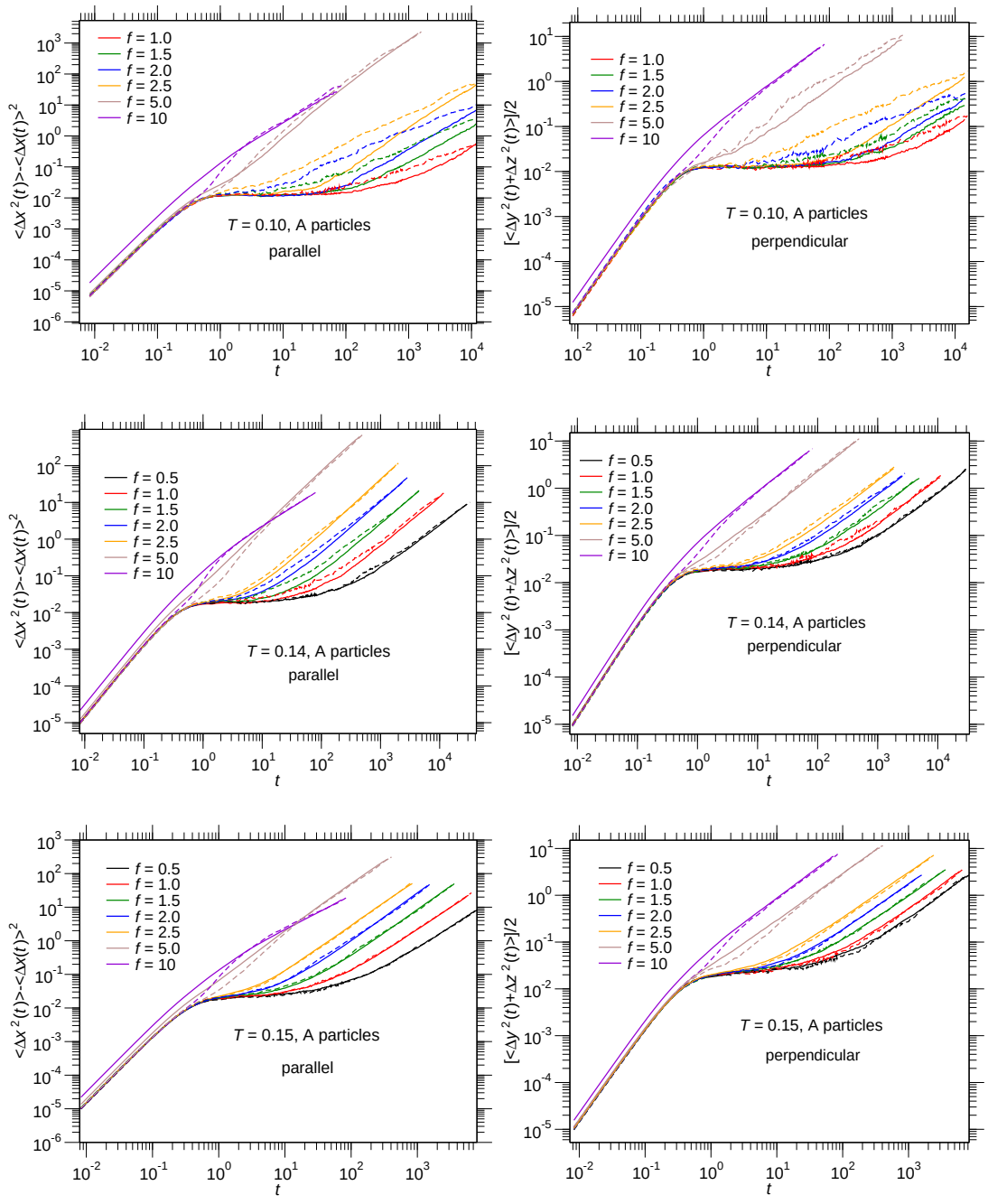

Figure 7.3 – Comparison of steady state (straight lines) and transient (dashed lines) measurements of the mean-squared displacement for different forces at $T = 0.10, 0.14, 0.15$. Left plots show parallel and right plots perpendicular direction for pulled A particles.

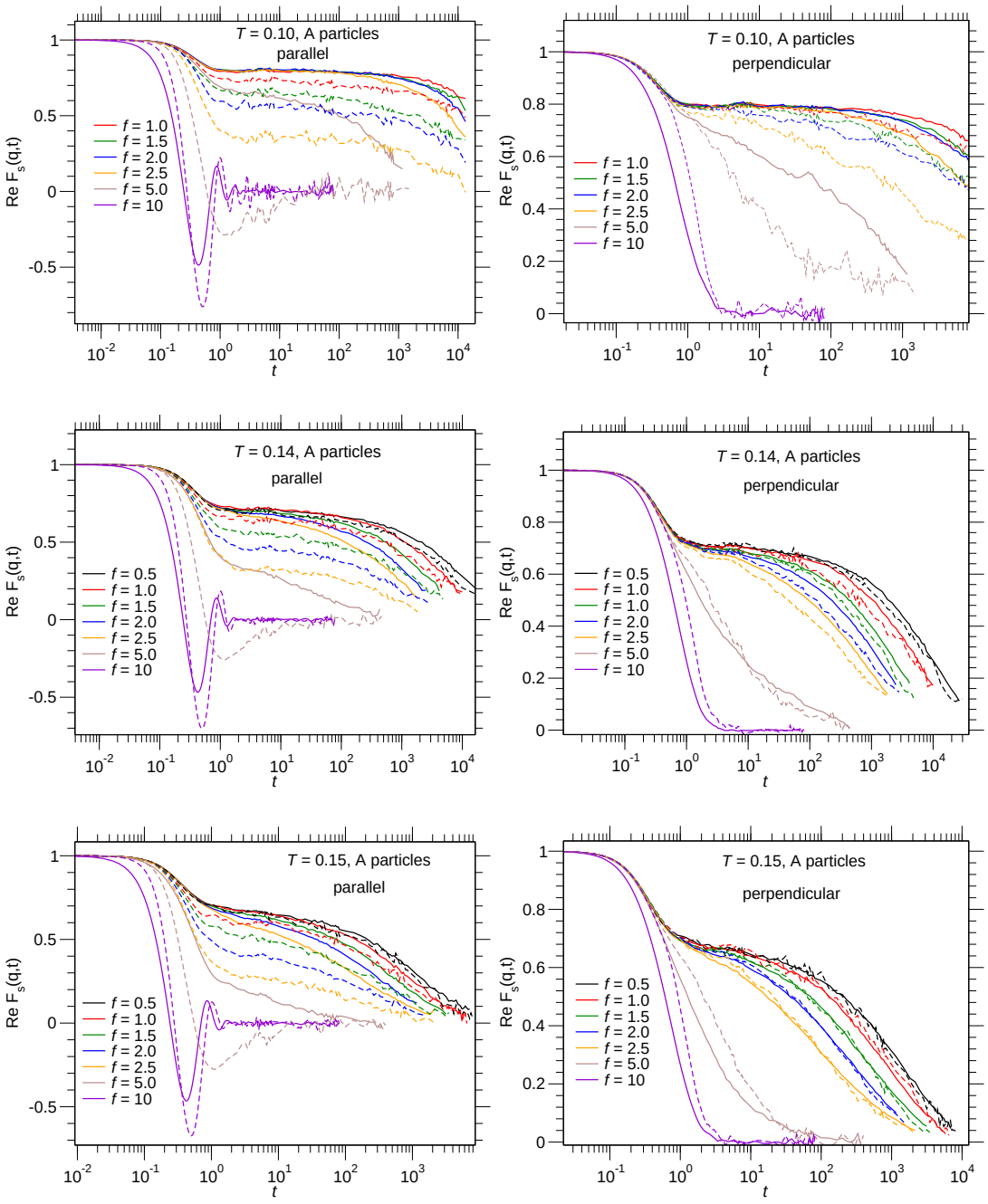

Figure 7.4 – Comparison of steady state (straight lines) and transient (dashed lines) measurements of the incoherent scattering function $F_s(q,t)$ for different forces at $T = 0.10, 0.14, 0.15$ and $q = 6.14$. Left plots show parallel and right plots perpendicular direction.

plateau in the log-log plot increases by orders of magnitude. But the steady state is reached much faster.

From these measurements it is also possible to calculate the diffusive motion of the particles during the onset of the force. In fig. 7.3 a direct comparison of the mean squared displacements at different temperatures and both directions for A particles is shown. One finds that for temperatures $T \geq 0.15$ the transient and the steady state curves in both directions converge quite fast against each other. Only for the highest forces one finds that the transient curves (dashed lines) at short and intermediate times show a deviation from the steady state motion. This results from the heating up of the probe particles that are at rest at the beginning of the simulation. That behavior can be observed at all investigated temperatures and in both directions. For temperatures $T \leq 0.14$ a second effect can be found. Here, at intermediate and long times one observes that the transient motion in both directions is much faster than the steady state motion. In the glass at $T = 0.10$ that effect is strongly pronounced over up to 4 decades in time. For these temperatures the diffusion at intermediate times is strongly increased after the switch on of the field. The same can also be seen in the incoherent scattering functions shown in fig.7.4 where the relaxation is strongly increased in both directions as the correlation functions decay much faster. Here, one even finds a strong direction dependence that results from the drift which is not subtracted in the parallel direction. Shortly after the switch on the velocity of the particles is higher then in the steady state and therefore leads to the strong decay of the scattering functions. These effects can be compared to the behavior under shear where one also observes an accelerated motion [5, 43]. Here, the effect after the switch on differs strongly. After the switch on of the shear field one also observes an accelerated diffusion and relaxation. But in contrast to the single particle behavior the curves move away from the equilibrium to the steady state behavior. For the pulled probes the relaxation after the switch on is even faster than in the steady state. Thus, one observes for short times a strong increase of the diffusion and relaxation with a maximum and then a decrease to the steady state behavior. Whereas in the sheared case one finds a monotonously increasing behavior. The difference of both cases could be a result of the different type of forces. In the sheared case the system was driven with a constant velocity that leads to a fluctuating stress in the system. In this work the probe particles are pulled with a constant force which leads to a fluctuating probe velocity. Thus, it could be that the observed behavior results from the pulling with a constant external force and it might be that by pulling the probe with a constant velocity the behavior changes.

As a direct comparison the behavior after the switch off can be investigated. In this experiment the force is switched of at time t' after it was initially switched on at $t = 0$. One can expect that the resulting switch off behavior strongly depends on t' until the particle has reached the steady state. In fig. 7.5 a) the behavior of the velocity is shown after the external force is switched off at time t'. Here, it is found that the response increases with longer waiting times. At short times one finds a behavior that

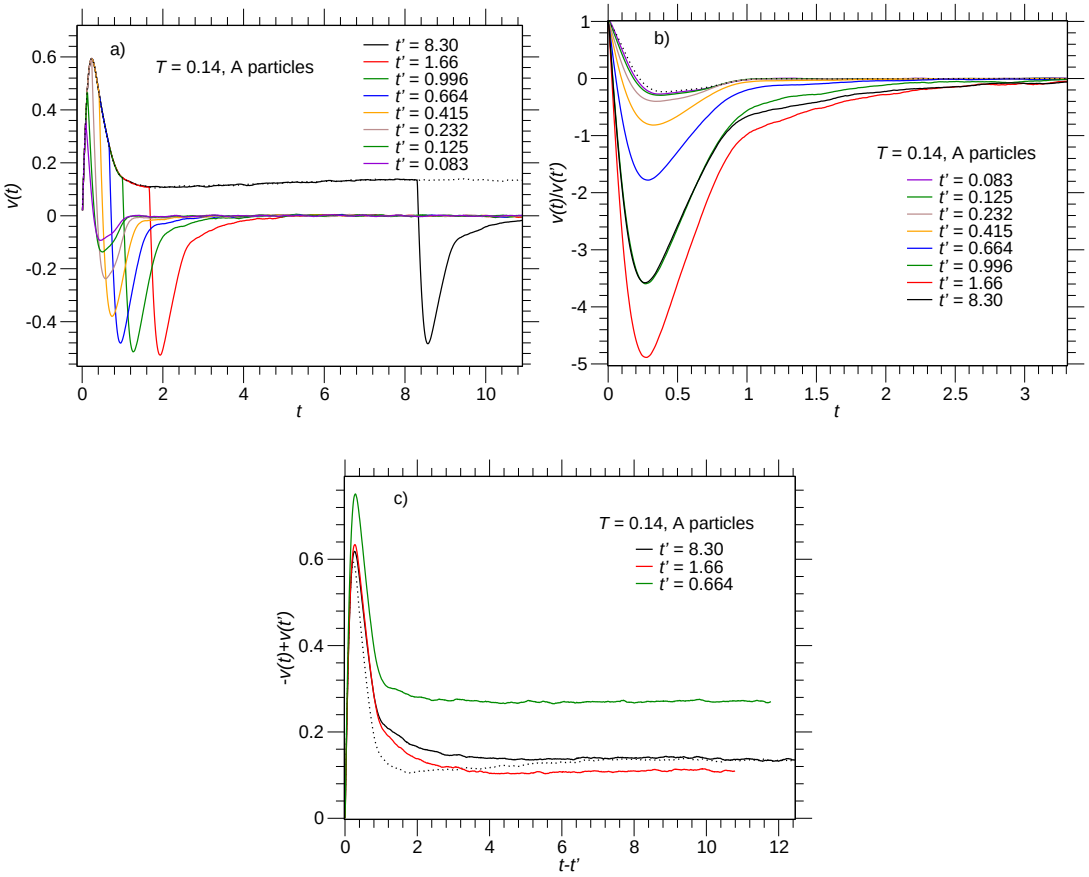

Figure 7.5 – c) Behavior of the velocities for pulled A particles with the external force switched off at time t'. Dotted line shows the behavior of the steady state motion. b) $v(t)/v(t')$ is shown to compare the behavior at short times with the equilibrium velocity autocorrelation function (dotted line). c) $-v(t) + v(t')$ is shown to compare the response at long times with the switch-on behavior (dotted line).

is similar to the velocity autocorrelation function in the equilibrium system. This can be better seen in b), where $v(t)/v(t')$ is displayed. Already for the shortest waiting time $t' = 0.083$ (10 integration steps) the response shows a slight deviation from the equilibrium velocity autocorrelation function (dotted line). Thus, the response here is only in the limit $t' \mapsto 0$ the equilibrium velocity autocorrelation function. With longer waiting times the magnitude of the response increases until it is similar to the inverse switch-on behavior. This is illustrated in fig. 7.5 c) where $-v(t) + v(t')$ is shown for long times t' against the switch-on behavior (dotted lines). In the steady state (straight black curve) the long-time and short-time regimes are identical and only at intermediate times both curves differ from each other. There, the response from the switch off shows a continuous decay to the long time value where the switch on curve has a dip with a minimum.

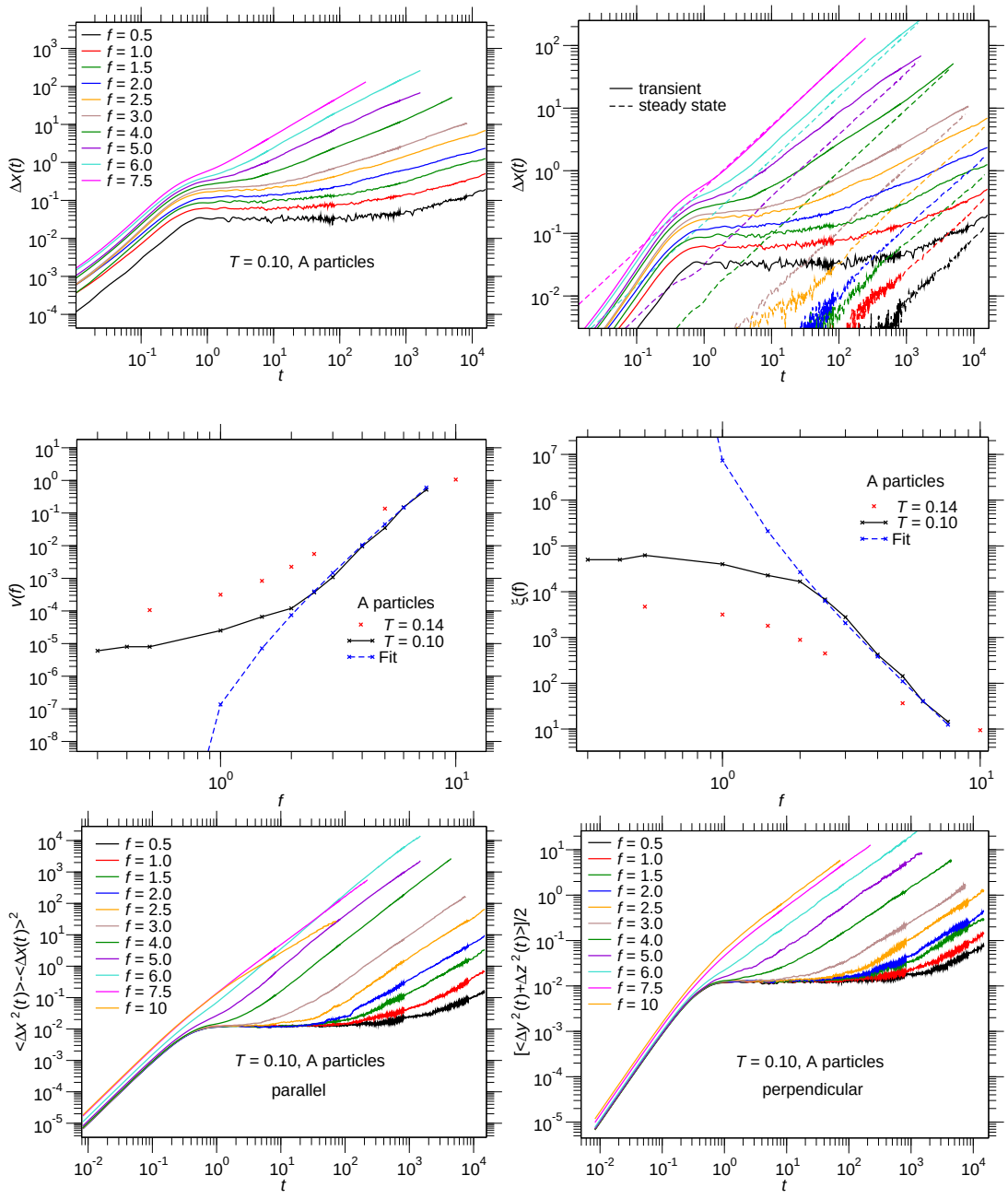

Figure 7.6 – Upper plots show displacement of the pulled A particles at $T = 0.10$ and different forces. Right plot shows transient measurements (straight lines) compared to the steady state measurements (dashed lines). Middle plots show the calculated steady state velocities and friction coefficients in the glass in dependence of the external force f. Lowest plots show steady-state measurements of the mean-squared displacement in the glass at $T = 0.10$ of pulled A particles and different forces f. Left plot shows parallel and right perpendicular direction.

7.2 The glass state

Having studied the steady-state behavior in the liquid and the switch on case the glass state can now be investigated. At temperatures $T < 0.14$ the equilibrium dynamics freeze on timescales accessible in the simulations. Thus, one does not observe a long time diffusive regime and also no relaxation to zero in the incoherent scattering functions. An interesting question that arises in this case is how particles under the influence of an external force behave at these temperatures. One can expect that for high forces the glass melts and that the particles move through the system. Here, it is interesting to check if even for small forces a steady state motion can be reached or if the particle is completely trapped for forces below a critical force f_0. In the upper plots of fig. 7.6 the transient displacements of A particles at $T = 0.10$ and different forces are shown and in the right plot in direct comparison the steady state displacements. Even at long times a strong difference between both curves is present and therefore the particle does not reach the steady state in the transient displacements. Here, the overshoot of the velocities at short times is too strong and consequently it completely hides the steady state motion. Nevertheless, it is present and it is reached as can be seen from the dashed lines where even at the lowest force $f = 0.5$ the average particle moves the distance $\Delta x \approx 0.1$ and the displacement shows a linear behavior. This observation is in contrast to previous results [13, 54, 69] where a freezing at low forces was found. Also the MCT predicts that below the glass transition a threshold force f_0 exists. Below this force the particles are completely arrested, the velocity is zero and the friction coefficient is infinity. Only for forces $f > f_0$ it is expected that the cages are destroyed and the particles move with a constant velocity through the system. Close to that critical force it was found that the particle velocity can be described by a power law which is given by

$$\begin{aligned} v &= v_0 \cdot \left(\frac{f}{f_0} - 1 \right)^{\alpha} && , \quad f > f_0 \\ &= 0 && , \quad f \leq f_0. \end{aligned} \tag{7.1}$$

This behavior was also found in experiments [13, 69, 70] where the predicted curves could be fitted against the measured values as is shown in fig. 7.7. There, the experimentally measured velocities in dependence of the applied force are shown for different volume fractions of the colloidal PMMA suspension. For the shown curves the volume fraction increases from left to right with the values $\phi = 0.29, 0.45, 0.50, 0.52, 0.53, 0.55$ but is always below the glass transition value of $\phi_g = 0.58$. Experimentally it is challenging to apply small external fields and therefore the particles could only be pulled at velocities in the intermediate and high force regime for temperatures below T_c. This is easier in computer simulations where the force can be set to an arbitrary small value and only the required statistics is a limiting factor. In the middle plots of fig. 7.6 the measured velocities and friction coefficients at $T = 0.10$ are shown. Indeed one finds

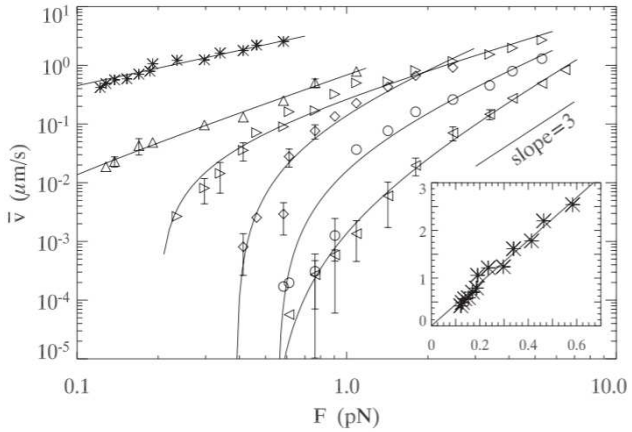

Figure 7.7 – Experimental values obtained for the velocities of the tracer particles in dependence of the applied force from [13].

that at intermediate forces the behavior of the velocity can be described by such a power law which is shown by the blue fit curve. The values for the extracted fit parameters are $\alpha = 6.55$, $f_0 = 0.03$ and $v_0 = 1.1 \cdot 10^{-16}$. Compared to the experiments the exponent α is much higher where $\alpha \approx 2.5$ was found and the obtained value for the threshold force is more than a factor of 10 smaller than the lowest investigated force and therefore not easily accessible with the present computational resources. Nevertheless, even for these much higher forces a strong deviation from the power law behavior is found that has not been observed in previous measurements. For small forces the friction coefficient seems to converge against a plateau value which is in contrast to the expected diverging behavior. Here, it is found that the particle motion is comparable with the liquid state, but only for a cooler system with a slower particle motion. A reason for that behavior could be the additional relaxation processes in the simulation that are not present in the theory such as the hopping terms or aging processes. The same behavior can also be observed for the diffusion and relaxation of the probe. In the lowest plots of fig 7.6 the mean-squared displacements for A particles at $T = 0.10$ in both directions are shown. There, the external force leads to an acceleration of the diffusion and the particles are able to reach the diffusive regime in the perpendicular direction on a timescale accessible in the simulation. For the parallel direction it is found that at long times the motion at small and intermediate forces is again superdiffusive and also the transition to the diffusive behavior at high forces can be observed. In fig 7.8 the incoherent scattering functions for the same particles are shown and they also shows a strong decrease of the relaxation times with increasing force. These observations are in contrast to the predictions from the theory. The MCT predicts a type A transition for the transition in dependence of the external force. There, the plateau in the glass is constant even for long times and continuously decreases to zero with increasing force, whereas in the simulations, even at low forces, a decay of the correl-

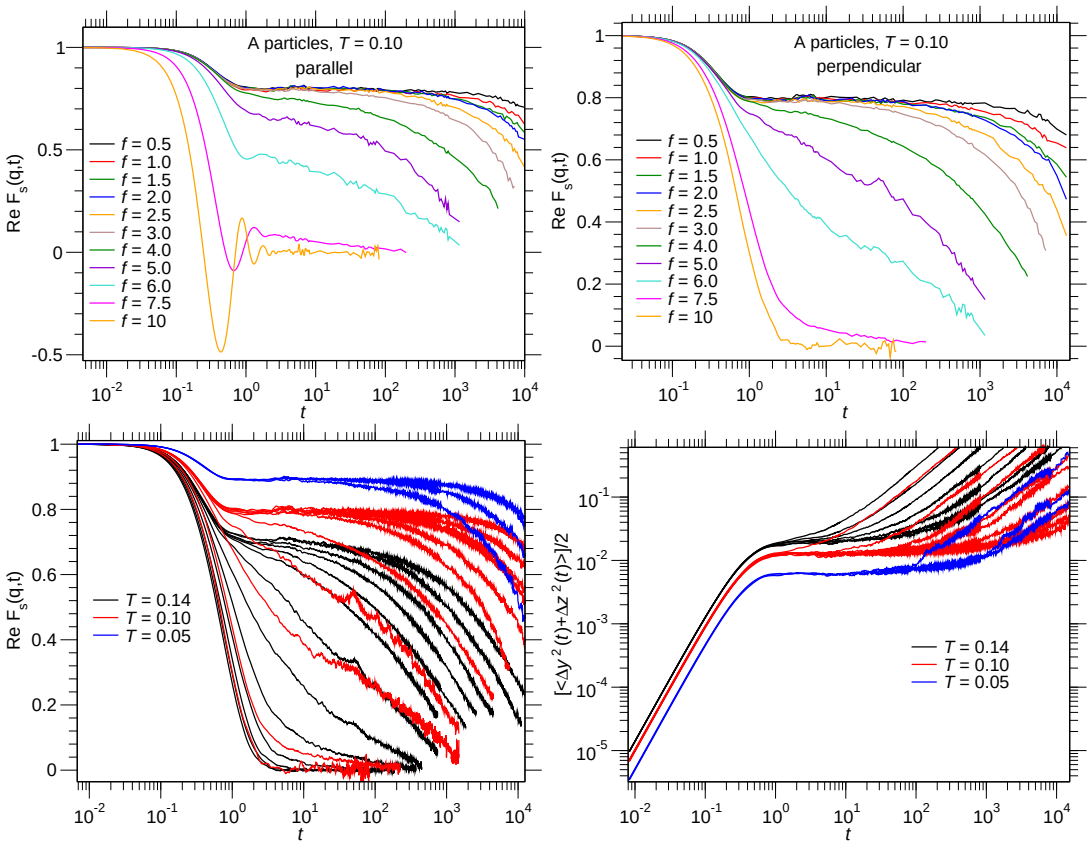

Figure 7.8 – Upper plots show steady-state incoherent scattering function $F_s(q,t)$ of pulled A particles in the glass at $T = 0.10$ for different forces f with $q = 6.14$. Left plot shows parallel and right perpendicular direction. Lower plots show left) $F_s(q,t)$ for $q = 6.14$ and right) mean-squared displacements in the perpendicular direction of A particles at temperatures $T = 0.14, 0.10, 0.05$. In the glass it is found that the height of the plateau shows a temperature dependence.

ation function to zero at long times is observed. Furthermore, the height of the plateau seems to be independent of the force as can be seen in fig. 7.8 where the scattering functions and the mean-squared displacements at $T = 0.14, 0.10, 0.05$ are directly compared with each other. There, the height of the plateaus changes with decreasing temperature but they are independent of the force. This is the typical behavior for a transition of type B. As a last point the behavior of the van Hove correlation functions is investigated in the glass. For the forces $f = 2.5$ and $f = 4.0$ at $T = 0.10$ they are shown in fig. 7.9 for the direction parallel to the force. Here, the behavior is also comparable to the behavior in the liquid at $T = 0.14$ with a strong peak at $x = 0$ and a long stretched tail in the force direction and also the second and third order peaks are visible.

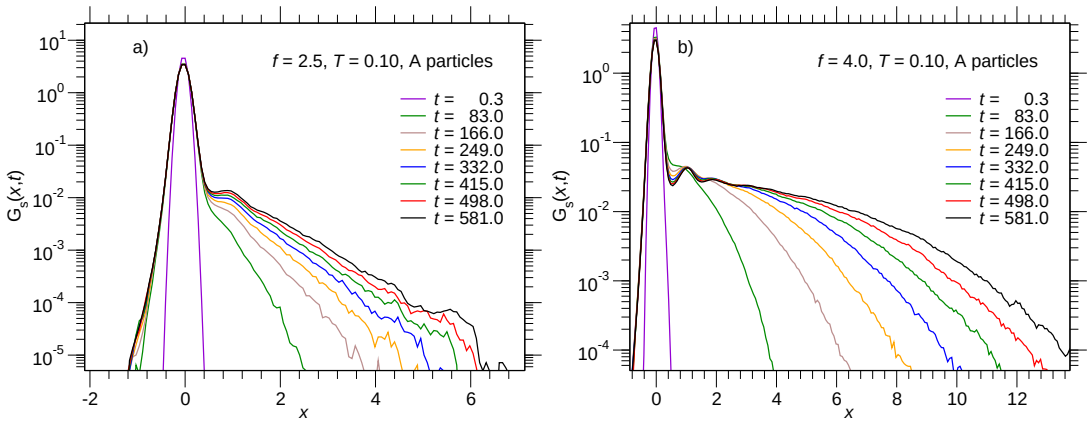

Figure 7.9 – Van Hove correlation functions $G_s(x,t)$ in the parallel direction for pulled A particles in the glass at $T = 0.10$ for a) $f = 2.5$ and b) $f = 4.0$.

7.3 Summary

First in this chapter the behavior of the particles after the switch on of the force was discussed. It was found that for short times an overshoot in the velocity appears where the particles move faster than in the steady state. That behavior influences the behavior of the displacements for a long time and leads to a plateau value that can be misinterpreted as a trapping region whereas the particle has already reached the steady state for a long time. This overshoot in the velocity also leads to a faster diffusion and relaxation at the beginning of the simulation. As a second part the behavior after the switch off was investigated and it is found that the response depends on the waiting times between the switch on and the switch off. In the last part of this chapter some measurements in the glass state were shown. There, it is found that the particle behavior in the glass is similar to the liquid case and that it reaches a steady state even for small forces. This finding is in contradiction to previous experimental results and predictions by the MCT where a threshold force is predicted and that expects that the whole dynamics is frozen for forces below this force. Furthermore, the observed transition seems to be of a different type. Here, a type B transition in dependence of the external force is observed, whereas the MCT predicts a type A transition. These differences could be a result from the fact that the system in these simulations is not in the equilibrium any more and therefore the behavior shows a dependence on the waited time before the particles were pulled.

With this chapter the investigation of the forced particle in the supercooled liquid in this work ends and the next chapter presents the results of the anisotropic critical behavior found in the Ising model.

Chapter 8

The Ising model under shear

The behavior of systems close to their critical point has been studied for a long time [74, 75, 76, 77]. For many equilibrium systems the important properties as the value of the critical point and of the critical exponents are known or can be calculated. The calculation of these informations in computer simulations is not always a simple task. Especially close to a critical point it is not straight forward to obtain the right informations about the system. In this region one observes a strong increase of the relaxation times and of the correlation lengths that complicates the work. It leads to an effective reduction of the system size which causes a smoothening of the phase transitions and thus an inaccurate measurement of the observables. For the equilibrium measurement the behavior of these finite systems is understood and a method known as finite-size scaling has been developed that solves the problem. There, from scaling arguments of the observables the true values can be calculated [32, 75]. Unfortunately, until now the critical behavior is only understood for the equilibrium case and only in parts for the non-equilibrium case. It has been investigated in recent years in different simple models as the driven lattice gas [78, 79] or the driven binary mixture [80]. Also a fluid under shear in the critical region was investigated by Kawasaki and Onuki [29, 30, 31] and many properties of the system as the behavior of the critical temperature T_c in dependence of the applied shear rate or the values of the critical exponents were calculated. Most of these predictions could be experimentally verified [81, 82] but up to now it is not completely understood how these systems can be treated in computer simulations and thus how the finite-size scaling has to be done. In the following the behavior of the Ising model under shear is investigated and a way is presented how the anisotropic finite-size scaling in the steady-state can be done.

8.1 The model

The model which is used in this work is the two-dimensional Ising model on a square lattice with $L_x \times L_y$ spins and nearest-neighbor interactions, so that all spins have 4 direct neighbors. All spins can flip from the state $+1$ to -1 and back and are coupled to their neighbors via the coupling constant $-J$. The Hamiltonian for this model is

$$\mathscr{H} = -J \sum_{<i,j>} \sigma_i \sigma_j \quad (\sigma_i = \pm 1). \tag{8.1}$$

This model is well understood and has been studied for a long time in the equilibrium. There, it was solved analytically in two dimensions by Onsager [83] who showed that the system has a critical point at the temperature $T_c = 2.269$. For simplification in this work temperatures are given in units of k_B/J with k_B the Boltzmann constant. In this part of the work this system under the influence of shear is studied. Therefore, it is not a good idea to simply apply the normal periodic boundary conditions here (that were presented in chapter 2 and used in the microrheology simulations). These would lead to surface effects at the borders where the system would feel a drastically increased shear which disturbs and complicates the measurements and hence are not wanted. Therefore, Lees-Edwards type periodic boundary conditions [84] are applied, that prevent these effects. With their help one has a bulk system that is completely homogeneous and feels the same shear rate at every point in the system. The implementation of these modified periodic boundary conditions is rather simple. All that is required is one counter that keeps track of the number of row shifts in the bulk system. Later on, in the energy calculation for the lowest and uppermost rows the direct neighbors, not the directly next neighbors are chosen. Instead the, by this counter shifted, neighbors are used to counteract the shift of the whole system. For a better understanding these boundary conditions are illustrated in fig 8.1 for a single shear step.

8.1.1 The sampling step

Here, the Metropolis step is used as the sampling step. It is an often used sampling step in the study of equilibrium statistical mechanics [85]. There the probability P_i for a given state i at time $\hat{t}$ is

$$P_i(\hat{t}) = \frac{1}{Z} \exp(-\beta E_i). \tag{8.2}$$

where, Z is the partition sum for the investigated system. The development of the probability is given by a master equation

$$\frac{\partial P_i(\hat{t})}{\partial t} = \sum_j P_j(\hat{t}) w_{ji} - \sum_j P_i(\hat{t}) w_{ij}, \tag{8.3}$$

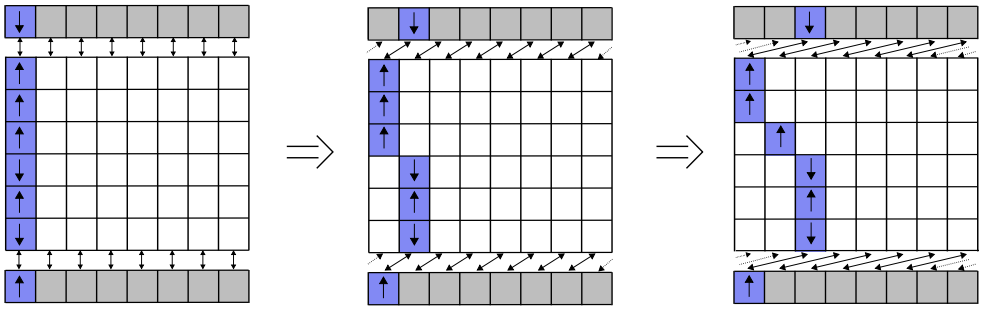

Figure 8.1 – Illustration of the shear step with Lees-Edwards type boundary conditions. Left is at the beginning before the first shear step, middle after the first step and right after the second step. Upper gray layer is a copy of the lowest row and lowest gray layer a copy of the first row to highlight the behavior of the boundary conditions that needs to keep track of the numbers of shifts to prevent surface effects.

with $P_i(\hat{t})$ the probability of finding the system in state i at time $\hat{t}$ and w_{ij} the transition rate from state i to state j. For the equilibrium system the left side is zero and then one obtains the following equition

$$\sum_j P_j w_{ji} = \sum_i P_i w_{ij}. \tag{8.4}$$

For the case that

$$P_j w_{ji} = P_i w_{ij} \tag{8.5}$$

is fulfilled, the system preserves detailed balance. By inserting (8.2) in (8.5) one obtains the expression for the transition rate

$$\frac{w_{ij}}{w_{ji}} = \frac{P_j}{P_i} = \exp(-\beta \Delta E), \tag{8.6}$$

in the case for $\Delta E = E_j - E_i > 0$. This is the Metropolis criterion for the change from one configuration to the next. In the case $\Delta E < 0$ the acceptance rate is 1 and the move is always accepted. Here, the sampling step is implemented in the following way. Randomly one lattice position is chosen and the difference ΔE between the present configuration i and the configuration with the flipped spin j at that position is calculated. If $\Delta E > 0$ a random number [86] between 0 and 1 is drawn and it that number is smaller than $\exp(-\beta \Delta E)$ the spin is flipped. If $\Delta E < 0$ the spin is directly flipped. That whole procedure is repeated $N = L_x \cdot L_y$ times until the sampling step is completed.

This sampling step can also be used in non-equilibrium systems. There, it is important to note that in contrast to the equilibrium case, the result of the simulation depends on the chosen sampling step. By using a different acceptance rate, for example the Glauber-sampling step [87], the heat dissipation changes and the system behaves different. A direct comparison showed that the Glauber dynamic leads to less heat dissipation under shear and therefore to less cooling of the system [88].

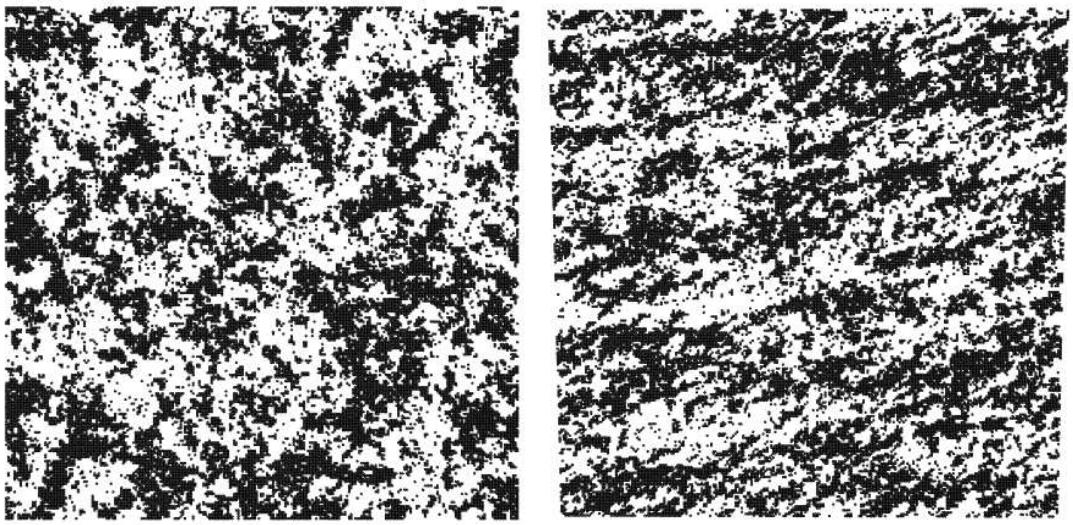

Figure 8.2 – Typical configuration snapshots at temperature $T = 2.45$. Left picture shows the unsheared equilibrium system with $\dot{\gamma} = 0.0$ and right the sheared system with $\dot{\gamma} = 0.3$. In the sheared system one observes a strong anisotropic behavior with strongly increased fluctuations in the shear direction. Here, black points showing up spins and white down spins on a $L_x = L_y = 250$ lattice.

8.1.2 The shear step

Sampling the system only with the Metropolis step leads to the equilibrium behavior which is of no interest here. To reach a sheared steady state a second step is required that drives the system out of equilibrium. In this work this is done by a shear step which follows after each sampling step and brings the anisotropy into the system. Here, a shear algorithm is used that was first presented in [89] for the study of nucleation under shear. The strength of the applied shear is set by the shear rate $\dot{\gamma}$ which depends on the two parameters M_s and P_s via $\dot{\gamma} = M_s \cdot P_s$. Here, P_s is the acceptance probability for each single row shift and M_s defines how often the shift is tried on average for each row. Each single row step contains the following steps:

- Draw a random number between 0 and 1. If that number is smaller than P_s, then go on. Else stop this row-shift step.
- Choose a lattice row $1 \leq n \leq L_y$ and shift all spins in rows from n to L_y by one lattice position into the positive x direction.
- Adjust the periodic boundary conditions to take the shear displacement into account (increase the counter by one).

This row-shift step is repeated $l = M_s L_y$ times. After l such steps the shear step is completed and the next relaxation step follows. Note, that the characteristic parameter

of the system behavior is the shear rate $\dot{\gamma}$ and that the behavior is independent of the explicit choice of M_s and P_s. Therefore, all results presented here depend only on $\dot{\gamma}$.

In fig. 8.2 some typical system configuration snapshots are shown. There, a direct comparison of the two systems with and without shear at $T = 2.45$ can be seen. One finds that the shearing strongly influences the behavior of the order parameter fluctuations. In the equilibrium system one has an isotropic behavior of the fluctuations. Switching on the shear leads to a strong anisotropy in these fluctuations. Here, it is found that the fluctuations in the direction parallel to the shear are much stronger than in the perpendicular direction. Furthermore, one can conclude only by looking at these snapshots that the correlation length of these two directions differs and is not isotropic any more.

8.1.3 Isotropic finite-size scaling

In equilibrium it is found that one observes a diverging correlation length ξ in the system close to a critical point. In finite systems this leads to a smoothening of the phase transition and to a strong system size dependence of the measured properties. Thus, a formalism is required to obtain the wanted informations as the exact value of the critical point or of the critical exponents. Here, the finite-size theory comes into play. For a finite system it is found that the behavior of the observables separates into a part that depends only on the length scale ξ and a second part that depends only on the system size L. One can therefore describe the system behavior in dependence of a universal scaling variable $x = tL^{1/\nu}$ with $t = (T/T_c - 1)$. For the singular part of the free energy of the system it is found [32, 77] that it scales as

$$F(L,T) = L^{-(2-\alpha)/\nu}\mathcal{F}(tL^{1/\nu}) \tag{8.7}$$

for a given temperature T and system size L. This function leads to expressions for the other observables. For the magnetization M follows

$$M(L,T) = L^{-\beta/\nu}\mathcal{M}(tL^{1/\nu}) \tag{8.8}$$

and for the susceptibility χ

$$\chi(L,T) = L^{\gamma/\nu}\chi(tL^{1/\nu}). \tag{8.9}$$

For higher moments in k-th order of the magnetization the expression (8.8) can be generalized to

$$\langle |M|^k \rangle = L^{-k\beta/\nu}\mathcal{M}_k(tL^{1/\nu}). \tag{8.10}$$

With the help of these scaling relations one has access to a simple method for calculating the critical point in the system. There, the fraction of the second and fourth moment needs to be calculated

$$U(t) = 1 - \frac{\langle M^4 \rangle}{3\langle M^2 \rangle^2} = \tilde{U}(tL^{1/\nu}). \tag{8.11}$$

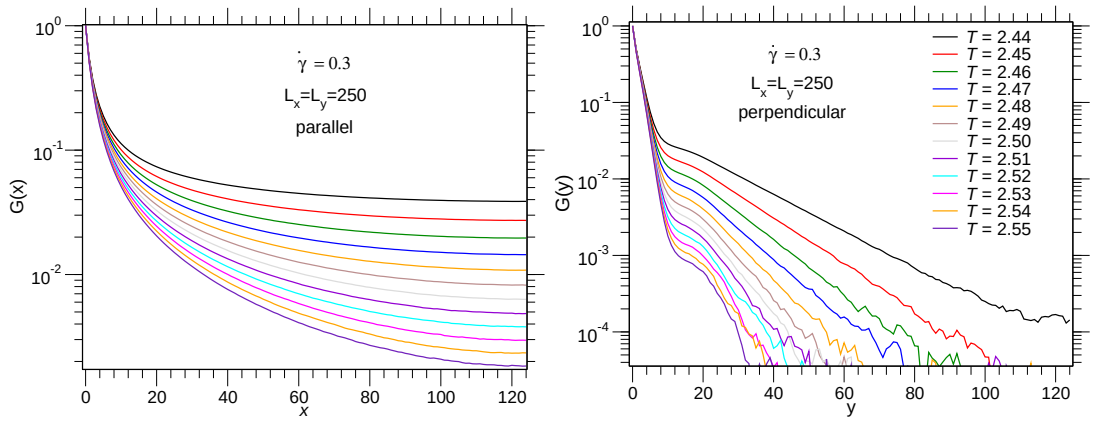

Figure 8.3 – Correlation function $G(\mathbf{r})$ for $L_x = L_y = 250$ systems at $\dot{\gamma} = 0.3$ and given temperatures for a) parallel and b) orthogonal to the shear direction.

Here, the dependence on the system size L cancels out and the fraction only depends on the universal scaling variable x. Direct at the critical point this variable is independent of the system size $x = 0$ and therefore the cumulants $U(t)$ for different system sizes all have an intersection point at T_c. Note, that this method requires that the system is large enough to be in the scaling regime and that these predictions are not fulfilled for too small systems.

8.1.4 The correlation length

One characteristic property of a critical point is the diverging correlation length ξ that follows a power law according to

$$\xi \propto t^{-\nu} \tag{8.12}$$

with the exponent ν. In the unsheared system this quantity can be measured from the behavior of the correlation function $G(r)$ between two spins at the distance r. Here, the system is isotropic and thus $G(r)$ only depends on the magnitude of $\mathbf{r}$

$$G(r) = \langle \sigma(0)\sigma(r) \rangle. \tag{8.13}$$

There, it is found that the correlation function in d dimensions has the Ornstein-Zernike form [32, 76] and behaves as

$$G(r) \propto r^{-(d-1)/2} \exp\left(-r/\xi\right) \tag{8.14}$$

It is interesting to investigate the behavior of this quantity for the sheared system and to check which differences can be observed. In fig. 8.3 $G(r)$ for the sheared system with $\dot{\gamma} = 0.3$ at different temperatures is shown. The first difference to the equilibrium is that the pair correlation function shows a strong anisotropic behavior. This is in agreement with the previous observations from the snapshots in fig. 8.2. In the direction

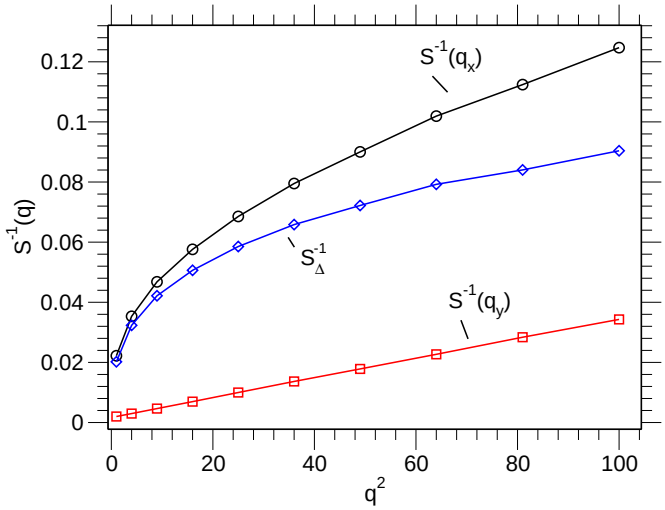

Figure 8.4 – Direction dependence of the inverse structure factor $S^{-1}(q)$ against q^2 at $T = 2.44$ for $\dot{\gamma} = 0.3$ and $L_x = L_y = 250$ geometry. Black line is parallel and red orthogonal to the shear direction. Blue line shows the difference between both directions.

perpendicular to the shear one finds a behavior that is in agreement with the Ornstein-Zernike behavior (8.14). There, an exponential decay at long distances is observed that, at least in principle, allows to measure a correlation length. In the parallel direction the case is different. Here, the behavior is strongly influenced by the shear and shows a different behavior. Even at the largest distances no exponential decay can be observed and therefore the algebraic behavior cannot clearly be identified. A second important observation that can be made is the shift of the critical temperature under shear. For the equilibrium case the critical temperature is $T_c = 2.269$ which is quite a bit away from the presented temperatures. Thus, one would not expect such a strong increase of the correlation length at these temperatures. Principally, it is possible to extract the correlation length from these measurements (at least in the perpendicular direction) but unfortunately in this presented case the fluctuations and finite-size effects are too strong for a direct measurement and therefore a different way is chosen.

8.1.5 The structure factor

It is found that the structure factor $S(q)$ [90] of the system is a useful quantity for the understanding of the finite-size scaling of the system

$$S(q) = \frac{1}{N}\Big\langle \rho(q)\rho(-q) \Big\rangle = \frac{1}{N}\Big\langle \Big| \sum_i \sigma_i e^{iqr_i} \Big|^2 \Big\rangle. \tag{8.15}$$

Previous work on a theoretical binary fluid model under shear [29, 30, 31] and experiments [81, 82] found that $S(q)$ shows a strong anisotropy for $q \to 0$ and that the

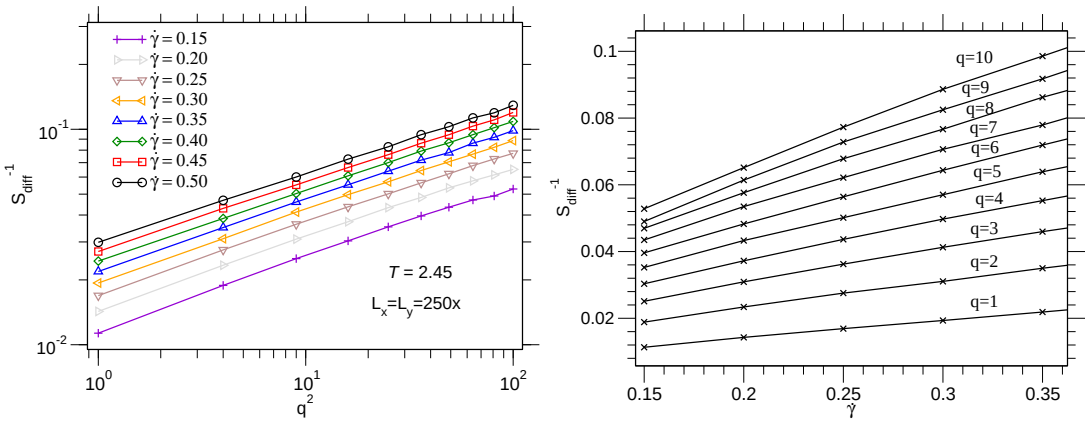

Figure 8.5 – Left) Behavior of the difference of the inverse structure factor $S(q)^{-1}$ in dependence of q^2 for different shear rates $\dot\gamma$ at $T = 2.45$. Right) Same curves in dependence of $\dot\gamma$ for a fixed value q.

behavior of the inverse structure factor is given by

$$S^{-1}(q) = A(T - T_c)^{\gamma} + Bq_x^{\omega} + Cq^2. \tag{8.16}$$

The identity $A(T - T_c)^{\gamma} = const$ is motivated by the equilibrium behavior $S^{-1}(q) = (k_B T\chi)^{-1}(1 + q^2\xi^2)$. Then, one can write

$$S^{-1}(q) = A(T - T_c)^{\gamma}\left(1 + \frac{B}{A}(T - T_c)^{-\gamma}q_x^{\omega} + \frac{C}{A}(T - T_c)^{-\gamma}q^2\right). \tag{8.17}$$

Generally wave numbers q scale as inverse length and therefore one can assume that the following relations

$$\xi_y^2 = \frac{C}{A}(T - T_c)^{-\gamma} = \hat{\xi}_y^2(T - T_c)^{-2\nu_\perp} \tag{8.18}$$

and

$$\xi_x^{\omega} = \frac{B}{A}(T - T_c)^{-\gamma} = \hat{\xi}_x^{\omega}(T - T_c)^{-\omega\nu_{||}} \tag{8.19}$$

hold. Inserting these expressions into (8.15) leads to

$$S^{-1}(q) = A(T - T_c)^{\gamma}(1 + (\xi_x q_x)^{\omega} + (\xi_y q)^2). \tag{8.20}$$

with the following exponents

$$\nu_{||} = \frac{\gamma}{\omega} \tag{8.21}$$

and

$$\nu_\perp = \frac{\gamma}{2}. \tag{8.22}$$

Both correlation length are therefore related via

$$\xi_x \propto \xi_y^{2/\omega} = \xi_y^{\nu_\perp/\nu_{||}}, \tag{8.23}$$

with $\omega/2 = \nu_\perp/\nu_{||}$. The important consequence is that by calculating the anisotropic structure factor one has found a way to measure the anisotropy exponent ω. This exponent plays an important role in the anisotropic finite-size scaling as is shown in the following sections. From the structure factor the value of ω can be calculated by taking the difference of both directions

$$\Delta S(q)^{-1} = S(q_x)^{-1} - S(q_y)^{-1} = B q_x^{\omega}. \tag{8.24}$$

In dependence of q the difference behaves as a power law with the wanted exponent. In fig. 8.4 the calculated structure factor for a system with $\dot{\gamma} = 0.3$ at $T = 2.44$ is shown. As is seen, the behavior of $S(q)$ in the perpendicular direction is $\propto q^2$ and in the parallel direction more complex. Also shown here in blue is the difference between both directions. The difference $\Delta S(q)^{-1}$ shows a power law behavior that can be seen in fig. 8.5 where only the difference in a log-log plot at $T = 2.45$ and different shear rates is shown. There, one finds that this method is quite robust as it shows no dependence on the shear rate and thus one can conclude that the value of this exponent is constant in the investigated region. To check how strong the following results are influenced by the value of this exponent the following calculations are done with two different exponents $\omega = 0.64$ and $\omega = 2/3$ that are both in agreement with the simulation results. From fig. 8.5 also the behavior of the prefactor in dependence of the shear rate can be studied and it is found that $\Delta S(q)^{-1} \propto \dot{\gamma} q_x^{\omega}$.

8.2 Anisotropic finite-size scaling

After a short introduction of the basic system properties in the last chapter, the anisotropic finite-size scaling for this system shall be presented here. For these systems the finite-size scaling behavior differs drastically from the equilibrium cases. There, the system shows an anisotropic behavior and therefore both directions have a different correlation length. Furthermore, even the temperature dependence in the different directions is not the same and thus one expects two or more different exponents for the correlation length. In this chapter an approach for the anisotropic finite-size-scaling is presented that generalizes the isotropic methods to the anisotropic case.

8.2.1 Finite-size scaling theory

The measured exponent ω plays a crucial role for the finite-size-scaling in the anisotropic system under shear. Close to the critical point the k-th moment of the order

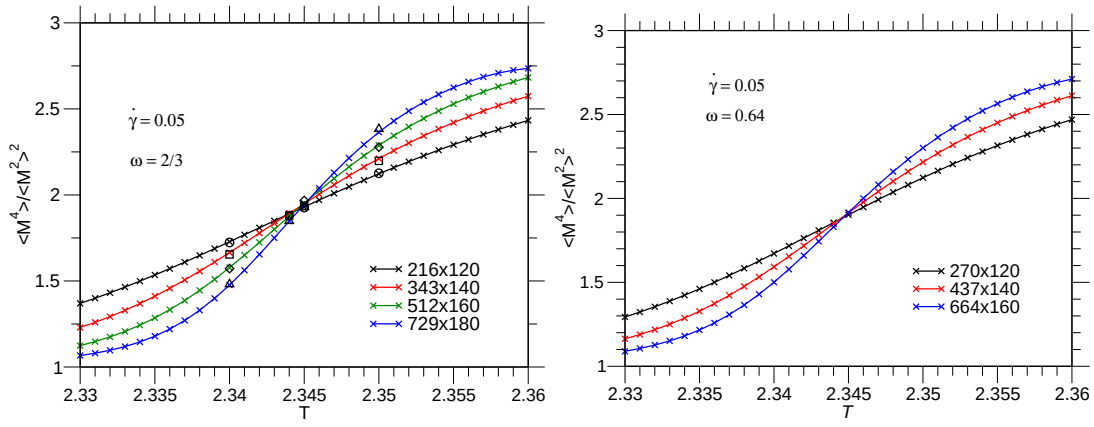

Figure 8.6 – Cumulant intersection points at shear rate $\dot{\gamma} = 0.05$. Left plot shows geometries with $\omega = 2/3$ and $c = 20$. Right plot with $\omega = 0.64$ and $c = 20$. Single black symbols are results from simulations and continuous colored lines from interpolation.

parameter is given [91, 92] by

$$\langle |M|^k \rangle = |1 - T/T_c|^{k\beta} \, \mathcal{M}_k(L_x/\xi_x, L_y/\xi_y) \tag{8.25}$$

Now, the scaling function depends on both directions. By taking a factor $(L_x/\xi_x)^{-k\beta/\nu_\parallel}$ out of the scaling function $\tilde{\mathcal{M}}_k$ one gets

$$\begin{aligned} \mathcal{M}_k(L_x/\xi_x, L_y/\xi_y) &= (\xi_x/L_x)^{k\beta/\nu_\parallel} \tilde{\mathcal{M}}_k(L_x/\xi_x, L_y/\xi_y) \\ &= L_x^{-k\beta/\nu_\parallel} |1 - T/T_c|^{-k\beta} \tilde{\mathcal{M}}_k(L_x/\xi_x, L_y/\xi_y). \end{aligned} \tag{8.26}$$

Here, the appearing prefactor was absorbed in the scaling function and (8.19) was inserted for ξ_x. This leads to the expression for the k-th moment

$$\langle |M|^k \rangle = L_x^{-k\beta/\nu_\parallel} \tilde{\mathcal{M}}_k(L_x/\xi_x, L_y/\xi_y). \tag{8.27}$$

In a second redefiniton step the temperature dependence in the second argument is removed and one obtains the scaling function $\tilde{\tilde{\mathcal{M}}}_k$

$$\begin{aligned} \tilde{\mathcal{M}}_k(L_x/\xi_x, L_y/\xi_y) =& \tilde{\tilde{\mathcal{M}}}_k \left((L_x/\xi_x)^{1/\nu_\parallel}, (L_y/\xi_y)/(L_x/\xi_x)^{\nu_\perp/\nu_\parallel} \right) \\ =& \tilde{\tilde{\mathcal{M}}}_k \left(t L_x^{1/\nu_\parallel}, L_y/L_x^{\nu_\perp/\nu_\parallel} \right). \end{aligned} \tag{8.28}$$

As the final expression for the k-th moment of the magnetization one obtains

$$\langle |M|^k \rangle = L_x^{-k\beta/\nu_\parallel} \, \tilde{\tilde{\mathcal{M}}}_k \left(t L_x^{1/\nu_\parallel}, L_y/L_x^{\nu_\perp/\nu_\parallel} \right). \tag{8.29}$$

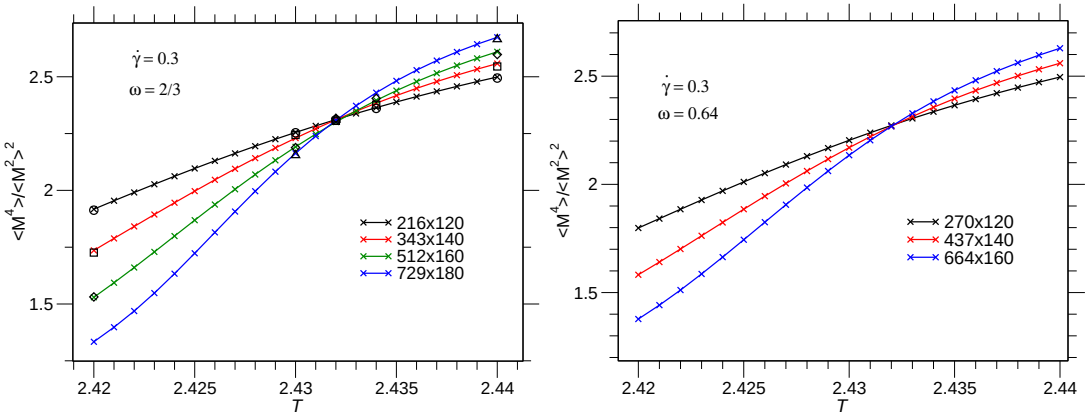

Figure 8.7 – Cumulant intersection points at shear rate $\dot{\gamma} = 0.3$. Left plot shows geometries with $\omega = 2/3$ and $c = 20$. Right plot with $\omega = 0.64$ and $c = 20$. Single black symbols are results from simulations and continuous colored lines from interpolation.

As in the isotropic case (8.11), the fourth-order cumulant [91] can now be defined by

$$U_{L_x,L_y}(t) = 1 - \frac{\langle M^4 \rangle}{3\langle M^2 \rangle^2} = \tilde{U}(tL_x^{1/\nu_\parallel}, L_y/L_x^{\nu_\perp/\nu_\parallel}) \tag{8.30}$$

Again, one has $t = 0$ at the critical point and $U_{L_x,L_y}(0) = \tilde{U}(0, L_y/L_x^{\nu_\perp/\nu_\parallel})$. The big difference to the isotropic case is that the cumulant still depends on the relation $L_y/L_x^{\nu_\perp/\nu_\parallel}$. To obtain a clear intersection point of $U_{L_x,L_y}(0)$ one needs to keep this relation constant which is fulfilled by scaling the systems according to $L_x = cL_y^{\omega/2}$. In this work for the two measured values of ω the chosen system sizes are $L_x \times L_y = 216 \times 120,\ 343 \times 140,\ 512 \times 160,\ 729 \times 180$ for $\omega = 2/3$ and $L_x \times L_y = 270 \times 120,\ 437 \times 140,\ 664 \times 160$ for $\omega = 0.64$. In both cases these correspond to the choice of $c = 20$. From the strongly enhanced fluctuations in the shear direction follows that the size L_x has to be chosen quite big with $L_x > 200$ to prevent unwanted strong finite-size effects.

Interpolation method A helpful method to calculate the cumulants at the different temperatures in the equilibrium case is the histogram extrapolation method [32, 93]. With this method it is possible to calculate histograms at temperatures that are close to the original simulated one from the same simulation. Thus, it is usually possible to reduce the fluctuations of the cumulants close to T_c without additional computational effort. As that method is based on the theory of equilibrium mechanics [94] it is therefore not expected to work in the steady state. Nevertheless, here it was empirically found that one can interpolate from one histogram to another in a similar way. In the canonical ensemble the probability for a configuration S at temperature T is given by

$$P_T(S) = \frac{1}{Z_T} e^{-\beta E} \tag{8.31}$$

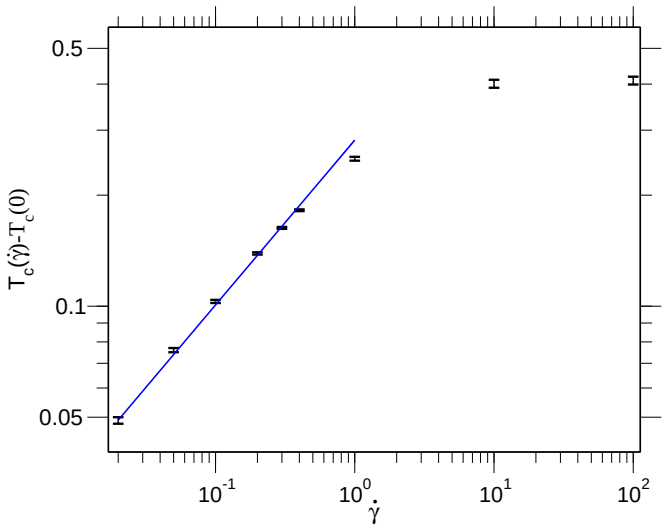

$\dot\gamma$	$T_c(\dot\gamma)$
0.02	2.318
0.05	2.345
0.1	2.372
0.2	2.408
0.3	2.432
0.4	2.451
1.0	2.520
10	2.670
100	2.678

Figure 8.8 – Shift of the critical temperature T_c in dependence of the shear rate $\dot\gamma$. Blue straight line shows a power-law fit for low shear rates with $\dot\gamma^\phi$ with $\phi = 0.44 \pm 0.01$.

Therefore, one can write for the fraction of the two probabilities of the same configuration and different temperatures

$$\frac{P_{T'}(S)}{P_T(S)} = \frac{Z}{Z'} e^{-(\beta'-\beta)E} \Leftrightarrow P_{T'}(S) = \frac{Z}{Z'} P_T(S) e^{-(\beta'-\beta)E}. \tag{8.32}$$

As a consequence one can calculate the histogram of the system at a different temperature T' by weighting every configuration by the factor $e^{-(\beta'-\beta)E}$ instead of 1. Here, it is found that for the sheared system a similar reweighting can be applied. In that case the weights have to be chosen as

$$\exp\left((\beta - \beta')\, E + c_\gamma \left(\frac{1}{\beta'} - \frac{1}{\beta} \right) E \right). \tag{8.33}$$

In fig. 8.6 and 8.7 the calculated cumulants for $\dot\gamma = 0.05$ and $\dot\gamma = 0.3$ are shown. As can be seen one finds a good agreement over the whole temperature range of the simulated values (black symbols) and the extrapolated values (colored lines). Thus, by using this method it is possible to extract the values of the critical points with a much higher precision. Furthermore, one can even calculate the derivatives at the critical point that are important for the calculation of the critical exponents. These calculations of the cumulants were done for a range of shear rates. All the obtained values for the critical temperatures in dependence of the shear rate are presented in fig. 8.8. As one sees, the critical temperature is shifted to higher values with increasing $\dot\gamma$. For small shear rates the critical temperatures follow a power law behavior according to $T_c(\dot\gamma) - T_c(0) \propto \dot\gamma^\phi$ with $\phi = 0.44 \pm 0.01$ (straight blue line). This is in agreement with the results found in [29, 82] where also a power-law shift of T_c was observed. For

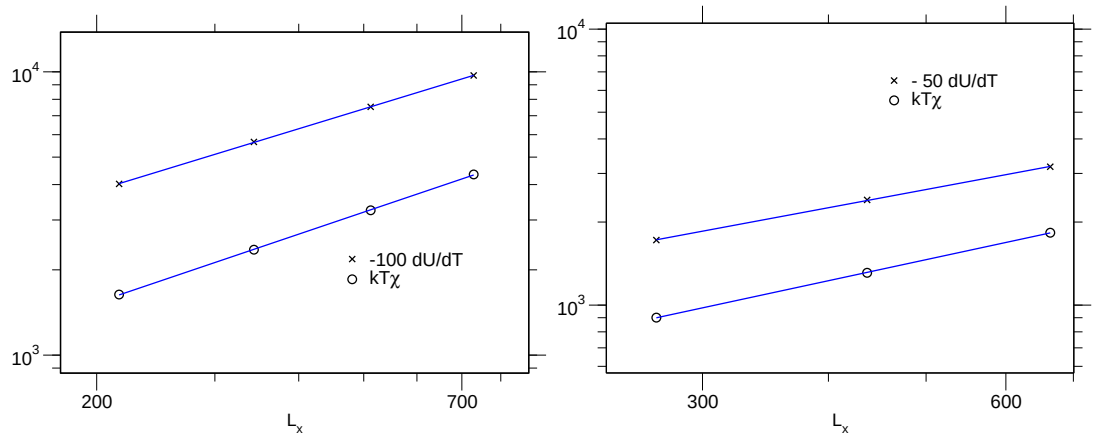

Figure 8.9 – Plots show derivative $\frac{\partial U}{\partial T}$ of the cumulant and the susceptibility χ in dependence of the system size L_x with constant ratio $L_y/L_x^{\nu_\perp/\nu_\parallel}$. Left plot is for $\dot{\gamma} = 0.05$ at $T = T_c = 2.345$ with $\omega = 2/3$ and $c = 20$. Right plot for $\dot{\gamma} = 0.3$ at $T = T_c = 2.432$ with $\omega = 0.64$ and $c = 20$. Second moments are scaled by a factor of 2 to fit into the same plots.

extremely high shear rates one observes a saturation of the critical temperature and it converges against the value $T_c \approx 2.68$. It is found that the values of the critical points are stable against small deviations of ω as can be seen in fig. 8.6 and 8.7 where a direct comparison for both values is shown.

8.2.2 Evaluation of the critical exponents

After the critical temperatures are determined it is much easier to calculate the critical exponents of the observables. Here, not only the single values of these exponents are of interest. Furthermore, it is interesting to check if a shear rate dependency exists or if they are independent of $\dot{\gamma}$. Knowing that the k-th moment scales according to (8.29) it follows that at T_c with $t = 0$ and fixed $L_y/L_x^{\nu_\perp/\nu_\parallel}$ the first and second moments of the magnetization scale as

$$\langle |M| \rangle \propto L_x^{-\beta/\nu_\parallel} \tag{8.34}$$

and

$$\langle M^2 \rangle \propto L_x^{-2\beta/\nu_\parallel}. \tag{8.35}$$

In an analogous manner it follows that the susceptibility $k_B T\chi = L_x L_y(\langle M^2 \rangle - \langle |M| \rangle^2)$ at T_c behaves as

$$\chi \propto L_x^{\gamma/\nu_\parallel}. \tag{8.36}$$

If $\nu_\parallel$ is known it is possible to calculate the values of β and γ from these relations. The value $\nu_\parallel$ can be obtained from the derivative of the cumulant [32, 95]. In the first order

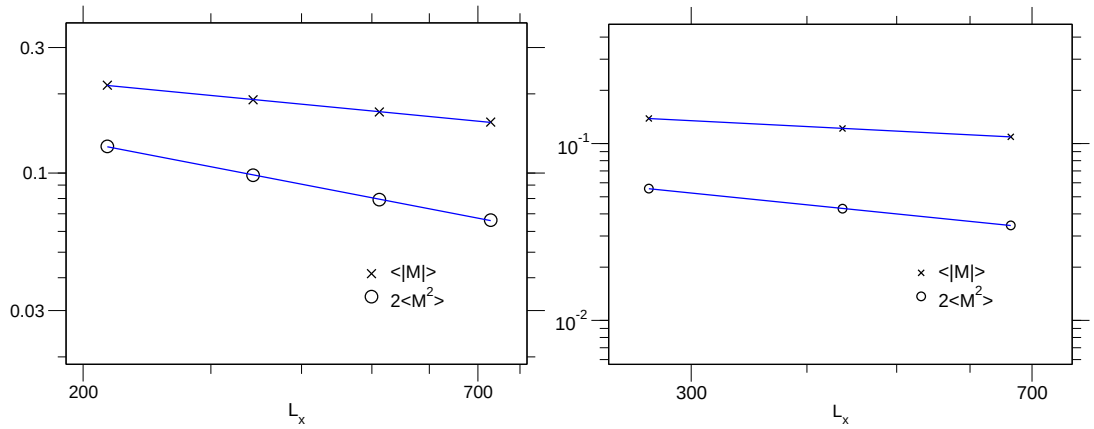

Figure 8.10 – Plots show first and second moment of the magnetisation $\langle |M| \rangle$ and $\langle M^2 \rangle$ in dependence of the system size L_x with constant ratio $L_y / L_x^{\nu_\perp / \nu_\parallel}$. Left plot is for $\dot{\gamma} = 0.05$ at $T = T_c = 2.345$ with $\omega = 2/3$ and $c = 20$. Right plot for $\dot{\gamma} = 0.3$ at $T = T_c = 2.432$ with $\omega = 0.64$ and $c = 20$. Second moments are scaled by a factor of 2 to fit into the same plots.

the derivative with a constant ration of $L_y / L_x^{\nu_\perp / \nu_\parallel}$ varies according to

$$\frac{\mathrm{d}U_{L_x,L_y}(t)}{\mathrm{d}T} \propto L_x^{1/\nu_\parallel}. \tag{8.37}$$

From this behavior the value of $\nu_\parallel$ can be extracted. In fig. 8.9 the behavior of the derivative and of the susceptibility are shown for $\dot{\gamma} = 0.05$ and $\dot{\gamma} = 0.3$. For the same systems in fig. 8.10 the first and second moment of the magnetization at T_c are shown. There, all properties show a power-law behavior over the investigated region of system sizes and therefore the exponents can be measured. The obtained critical exponents in dependence of the shear rate and both values of ω are presented in tab. 8.1. Here, no dependence on the shear rate for the investigated values of $\dot{\gamma}$ is observed but a slight dependence on ω is found.

For high shear rates it can be expected that the system behaves like a mean field system

Table 8.1 – Measured critical exponents of the system

$\dot{\gamma}$	ω	$\nu_\parallel$	$\nu_\perp$	β	γ
0.05	2/3	1.38	0.46	0.37	1.11
0.1	2/3	1.38	0.46	0.35	1.23
0.3	2/3	1.37	0.46	0.38	1.07
0.05	0.64	1.45	0.48	0.38	1.17
0.1	0.64	1.46	0.49	0.36	1.21
0.3	0.64	1.47	0.49	0.39	1.16

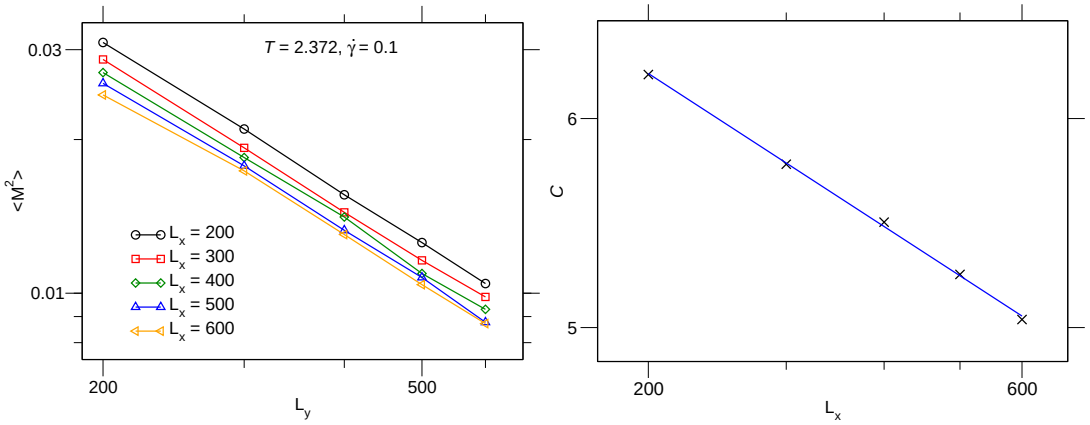

Figure 8.11 – Left) Second moment $\langle M^2 \rangle$ in dependence of L_y fo fixed L_x at $T = T_c = 2.372$ for $\dot{\gamma} = 0.1$. Right) Calculated prefactor C in dependence of L_x.

with an infinite shear rate. In this limit the system can be solved analytically [96, 97]. There, the values for the critical exponents of the correlation length are $\nu_{\parallel} = 1.5$ and $\nu_{\perp} = 0.5$ with the mean field critical point is $T_c = 3.466$. Especially the values of the exponents for $\omega = 0.64$ are not too far away from the mean field values although for the investigated region of shear rates still a strong dependence of T_c on $\dot{\gamma}$ could be observed. Thus, the system was definitely not in the mean field region. For high shear rates $\dot{\gamma} > 10$ the finite-size effects increased dramatically. There, it is required to go to even larger system sizes to obtain a realistic values for the measured properties that explains the strong difference between the measured T_c and the mean field value. At these high shear rates it is found that the behavior on ω increases strongly and therefore one needs to measure this exponent with a higher precision first before the whole finite-size scaling analysis can be done.

8.2.3 Consistency checks

In this section a consistency check for the critical exponents is presented. At the critical point the maximum size of the correlations in the finite system is given by the system size. In the x-direction the maximum correlation length is given by

$$\xi_x = L_x \tag{8.38}$$

and therefore in the y-direction by

$$\xi_y = c\xi_x^{\nu_\perp/\nu_\parallel} = cL_x^{\nu_\perp/\nu_\parallel}. \tag{8.39}$$

By choosing the system size as

$$L_y = n\xi_y \tag{8.40}$$

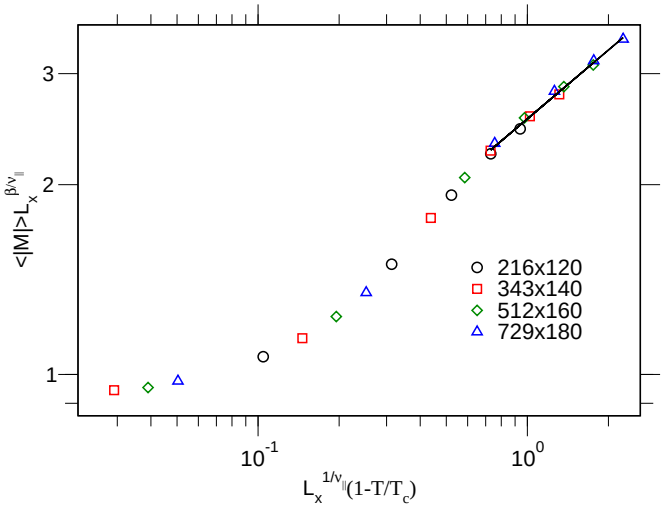

Figure 8.12 – Universal scaling behavior of $\langle|M|\rangle L_x^{\beta/\nu_\parallel}$ against $x = L_x^{1/\nu_\parallel}(1 - T/T_c(\dot{\gamma}))$ for temperatures below T_c at $\dot{\gamma} = 0.05$, $\omega = 2/3$ and $c = 20$. Black line at high values shows a fit with the exponent $\beta \approx 0.36$.

one has n uncorrelated clusters in the y-direction. Thus, one expects a scaling of for the second moment of the magnetization according to

$$\langle M^2 \rangle \propto \frac{1}{n} \propto L_y^{-1}. \tag{8.41}$$

On the other hand follows from (8.29) that

$$\langle M^2 \rangle = L_x^{-2\beta/\nu_\parallel} \, \tilde{\tilde{\mathcal{M}}}_2 \, (0, L_y/L_x^{\nu_\perp/\nu_\parallel}). \tag{8.42}$$

Combining these two relations, the following expression is found

$$\langle M^2 \rangle = C L_y^{-1} \propto L_x^{-2\beta/\nu_\parallel} L_x^{\nu_\perp/\nu_\parallel} L_y^{-1} = L_x^{\nu_\perp/\nu_\parallel - 2\beta/\nu_\parallel} L_y^{-1} \tag{8.43}$$

with

$$C \propto L_x^{\nu_\perp/\nu_\parallel - 2\beta/\nu_\parallel}. \tag{8.44}$$

By keeping L_x fixed and varying L_y one can calculate the constant C in dependence of L_x. Then, from the L_x dependence of C one obtains the value for $\nu_\perp/\nu_\parallel - 2\beta/\nu_\parallel$ and from the already known value of $\beta/\nu_\parallel$ the relation $\nu_\perp/\nu_\parallel$ can be estimated. Here, this was done for $\dot{\gamma} = 0.1$ where the system sizes were varied in the range $200 \leq L_x, L_y \leq 600$. The results for the second moments and the constant C are shown in fig 8.11. As one can see the prediction of (8.41) is fulfilled in the chosen range of system sizes. Against these curves fits with a behavior according to (8.43) were made and the constant C was measured. These calculated values are shown in the right plot of fig. 8.11. In the next step these points were fitted by a power law and the exponent was

extracted. According to (8.44) the exponent corresponds to $\nu_\perp/\nu_\parallel - 2\beta/\nu_\parallel$ which in this case has the value -0.19 ± 0.01. As a consequence $\nu_\perp/\nu_\parallel \approx 0.32 \pm 0.01$ follows that is in agreement with the previous results obtained from the structure factor.

A second consistency check is the calculation of the scaling function

$$\tilde{\tilde{\mathcal{M}}}_k\left(tL_x^{1/\nu_\parallel}, L_y/L_x^{\nu_\perp/\nu_\parallel}\right) = \langle|M|\rangle L_x^{\beta/\nu_\parallel} \tag{8.45}$$

in dependence of the scaling variable $x = L_x^{1/\nu_\parallel}(1 - T/T_c(\dot{\gamma}))$. For the right geometries the values for the different measurement should collapse onto the same universal curve. Here, the previously calculated exponents $\nu_\parallel$ and β are required. For $\dot{\gamma} = 0.05$ with $\omega = 2/3$ this universal scaling is shown in fig. 8.12. There, all values of the different measurements collapse nicely onto the same universal scaling curve and therefore the scaling properties are fulfilled. For high values of x the scaling function should behave asymptotically as the infinite-lattice critical behavior. Therefore, in this regime $\tilde{\tilde{\mathcal{M}}}_k \approx x^\beta$ should hold [98]. This is checked by a power law fit against the highest values (black line) which gives the value $\beta \approx 0.36$ that is in agreement with the previous measurement.

8.3 Summary and outlook

In this chapter the finite-size scaling of the Ising model under shear was investigated. It was found that by an additional shear step a strong anisotropy is brought into the system which leads to two different correlation lengths, parallel and perpendicular to the shear direction. As a consequence an anisotropic finite-size scaling of the system is required. The finite-size scaling can be accomplished by scaling both system sizes with a fixed ratio, that is given by an exponent. With the help of the structure factor that exponents could be measured. In the following the critical points in dependence of the shear rate were measured and it is found that the critical point shifts to higher temperatures. From the scaling relations in addition the critical exponents $\beta, \gamma, \nu_\parallel$ and $\nu_\perp$ could be calculated.

Chapter 9

Final remarks

In this work two different slowly relaxing model systems under the influence of external forces were studied. The first system was a binary soft-sphere mixture that shows a glassy dynamics at low temperatures. There, the active non-linear microrheology was investigated. In the second part of the work the behavior of the Ising model under shear close to the critical point was studied and a method was presented how the finite-size scaling can be accomplished in this anisotropic case.

Soft-sphere mixture: Here, the behavior in the non-linear response was of interest which could easier be studied in a slowly relaxing system. Therefore the binary Yukawa mixture was chosen where at low temperatures a glass transition with strongly increasing relaxation times is observed. By comparably low external forces the system can be driven into the non-linear regime. In dependence of the applied force three different regimes can be identified. For the lowest forces the particle motion is still in the linear-response regime where the particle properties are given by the equilibrium properties. This can be seen from the constant plateau in the friction coefficient at low forces and higher temperatures. At lower temperatures on observes that at intermediate forces the particle motion deviates from the linear-response behavior and the velocity increases superlinearly. Thus, the friction coefficient decreases with increasing force. In that regime one finds a strongly anisotropic particle motion which is superdiffusive in the force direction. Furthermore, a universal scaling regime is found that allows to scale the perpendicular diffusion constants, the relaxation times and the friction coefficients in dependence of temperature onto the corresponding equilibrium properties. Therefore, the important properties of the particle in the non-linear regime behave as in equilibrium but at a different temperature. This has lead to the definition of an effective temperature which is found to scale quadratic with the applied force. At higher forces a third regime was observed where the motion in the force direction is diffusive again and the anisotropy of the motion reduces with increasing force. These results are characteristic for a system with glassy dynamics that has a frozen structure which prevents a backflow in the system and leads to a separation of the time scales between

the motion of the pulled particle and the surrounding environment. The behavior of the pulled particles can be understood with the help of two theoretical models. A simple directed trap model shows the behavior of superdiffusivity. In that model the strength of the behavior depends on the external force and first leads to an increase and then to a decrease at higher forces which is also found in this work. Also the transition to the diffusive motion at high forces is found but it clearly misses a lot of important properties such as the equilibrium dynamics and the influence of the pulled particle on the surrounding. Therefore, it can only be seen as a first starting point for the understanding of the particle behavior in a glassforming liquid. The second model is a much more sophisticated model, a schematic model in the framework of the mode coupling theory. This model succeeds in describing a big part of the equilibrium dynamics of the system and thus gives the correct low force limits in the liquid. Here, the problem is in the superdiffusive motion that cannot be described with that model. A problem with these predictions is that the used model is a reduced schematic model which takes only one q-value into account. Therefore, one cannot expect that it describes the whole dynamics correctly as effects that result from multiple modes are excluded. Here, these simulation results should motivate further investigations on the theoretical and experimental side to improve the present models and measure the particle behavior with a higher precision. For further work from the simulation side it would be interesting to investigate the behavior in the superdiffusive regime with a higher precision and longer simulation runs. There, it would be interesting to study the behavior in a different system for example in the Weeks-Chandler-Andersen (WCA) mixture [99] that can be simulated more efficiently and allows longer simulation runs. Thus, one has access to a better statistics and could therefore gain more precise results about the effective temperatures and their behavior. Here, it would be interesting to definitely answer the question if one observes different effective temperatures for the different observables or if it is the same for all quantities. Furthermore, it would also be interesting to investigate the behavior in the glass in more details. There, one interesting question that one could investigate is the effect of aging on the particle behavior where it could be that with increased waiting times the behavior of the particles approaches the theoretical predicted behavior with a threshold force and frozen particles for forces below that threshold. In that case one could expect that the friction coefficient increases with longer waiting times and converges against the predicted power law behavior.

Ising model under shear: The second part of the work was a preliminary study to understand the behavior of a system under shear. Here, the anisotropic finite-size scaling in the Ising model under shear was investigated which is a simple model system for a liquid system under shear. With the help of that model a way was found to accomplish the finite-size scaling in the anisotropic system. Shearing the Ising model also leads to a strong anisotropic behavior close to the critical point and the usual finite-size scaling breaks down. In this work it was shown that the relation between the two exponents of the correlation length is crucial for the scaling and that this value can be obtained from the structure factor of the system. With that exponent known the scaling can be

extended to the anisotropic case and the critical points and exponents could be identified. Here, it was found that the critical exponents change from the equilibrium values towards the mean-field values of the system. In a future work it would be interesting to check if this method can be applied in a continuous model as the AO model or the binary liquid and if one can verify the theoretical predictions for these models. There, also the influence of the hydrodynamic interactions would be of interest as it is predicted that they lead to a shift of the critical temperatures into the opposite direction as in the Ising case. Furthermore, it would be interesting to study the effect of shear on additional properties such as the interface tensions and on the capillary waves also far away from the critical point. In principle here one could start again with these measurements in the sheared Ising model and later move on to a more realistic continuous model.

List of Figures

Bibliography

[1] M. E. Cates and M. R. Evans, *Soft and fragile matter: Nonequilibrium dynamics, metastability and flow*, (Institute of Physics Pub., London), copublished by (Scottish Universities Summer School in Physics, 2000).

[2] W. B. Russel, D. A. Saville and W. R. Schowalter, *Colloidal dispersions*, (Cambridge University Press, Cambridge, 1989).

[3] W. Poon, *Colloids as big atoms*, Science **304**, 830 (2004).

[4] R. G. Owens and T. N. Phillips, *Computational rheology*, (Imperial College Press, London, 2002).

[5] J. Zausch, Dissertation: *Dynamics, rheology and critical properties of colloidal fluid mixtures*, http://ubm.opus.hbz-nrw.de/volltexte/2009/1911/ (2008).

[6] N. J. Wagner and J. F. Brady, *Shear thickening in colloidal dispersions*, Physics Today **62**, 27 (2009).

[7] T. A. Waigh, *Microrheology of complex fluids*, Rep. Progr. Phys. **68**, 685 (2005).

[8] T. M. Squires and T. G. Mason, *Fluid mechanics of microrheology*, Annu. Rev. Fluid Mech. **42**, 413 (2010).

[9] T. M. Squires and J. F. Brady, *A simple paradigm for active and nonlinear microrheology*, Phys. Fluids **17**, 073101 (2005).

[10] R. Zia and J. F. Brady, *Single-particle motion in colloids: force-induced diffusion*, J. Fluid Mech. **658**, 188 (2010).

[11] A. S. Khair and J. F. Brady, *Microrheology of colloidal dispersions: Shape matters*, J. Rheol. **52**, 165 (2008).

[12] A. S. Khair and T. M. Squires, *Active microrheology: A proposed technique to measure normal stress coefficients of complex fluids*, Phys. Rev. Lett. **105**, 156001 (2010).

[13] P. Habdas, D. Schaa, A. C. Levitt and E. R. Weeks, *Forced motion of a probe particle near the colloidal glass transition*, Europhys. Lett. **67**, 477 (2004).

[14] I. Sriram, A. Meyer and E. M. Furst, *Active microrheology of a colloidal suspension in the direct collision limit*, Phys. Fluids **22**, 062003 (2010).

[15] L. G. Wilson, A. W. Harrison, W. C. K. Poon and A. M. Puertas, *Microrheology and the fluctuation theorem in dense colloids*, Europhys. Lett. **93**, 58007 (2011).

[16] L. G. Wilson, A. W. Harrison, A. B. Schofield, J. Arlt and W. C. K. Poon, *Passive and active microrheology of hard-sphere colloids*, J. Phys. Chem. B **113**, 3806 (2009).

[17] S. R. Williams and D. J. Evans, *Linear Response Domain in glassy systems*, Phys. Rev. Lett. **96**, 015701 (2006).

[18] R. J. DePuit, A. S. Khair and T. M. Squires, *A theoretical bridge between linear and nonlinear microrheology*, Phys. Fluids **23**, 063102 (2011).

[19] K. Binder and W. Kob, *Glassy materials and disordered solids: An introduction to their statistical mechanics*, (World Scientific, Singapore, 2005).

[20] W. Kob. In: J. L. Barrat, M. Feigelman, J. Kurchan et al., *Les Houches summer school: Slow relaxations and nonequilibrium dynamics in condensed matter*, **77** 199, (2004).

[21] P. G. Debenedetti and F. H. Stillinger, *Supercooled liquids and the glass transition*, Nature **410**, 259 (2001).

[22] G. Adam and J. H. Gibbs, *On the temperature dependence of cooperative relaxation properties in glass-forming liquids*, J. Chem. Phys. **43**, 139 (1965).

[23] D. Turnbull and M. H. Cohen, *On the free-volume model of the liquid-glass transition*, J. Chem. Phys. **52**, 3038 (1970).

[24] P. Sollich and F. Ritort, *Workshop on glassy behaviour of kinetically constrained models*, J. Phys.: Condens. Matter **14**, 1381 (2002).

[25] W. Götze and L. Sjögren, *Relaxation processes in supercooled liquids*, Rep. Prog. Phys. **55**, 241 (1992).

[26] W. Götze, *Complex dynamics of glass-forming liquids: A mode-coupling theory*, (Oxford University Press, New York, 2008).

[27] S. Asakura and F. Oosawa, *Interaction between particles suspended in solutions of macromolecules*, J. Polym. Sci. **33**, 183 (1958).

[28] J. Zausch, P. Virnau, K. Binder, J. Horbach and R. L. Vink, *Statics and dynamics of colloid-polymer mixtures near their critical point of phase separation: A computer simulation study of a continuous Asakura–Oosawa model*, J. Chem. Phys. **130**, 064906 (2009).

[29] A. Onuki and K. Kawasaki, *Nonequilibrium steady state of critical fluids under shear flow: A renormalization group approach*, Ann. Phys. **121**, 456 (1979).

[30] A. Onuki, *Phase transitions of fluids in shear flow*, J. Phys.: Condens. Matter **9**, 6119 (1997).

[31] A. Onuki, *Phase Transition Dynamics*, (Cambridge Univ. Press, Cambridge, 2002).

[32] D. P. Landau and K. Binder, *A guide to Monte Carlo simulations in statistical physics*, (Cambridge University Press, Cambridge, 2005).

[33] D. Frenkel and B. Smit, *Understanding molecular simulation: From algorithms to applications*, (Academic Press, London, 2002).

[34] L. Verlet, "Computer *Experiments" on classical fluids. I. Thermodynamical properties of Lennard-Jones molecules*, Phys. Rev. **159**, 98 (1967).

[35] M. P. Allen and D. J. Tildesley, *Computer simulation of liquids*, (Oxford University Press, New York, 1991).

[36] M. P. Allen, *Introduction to Molecular Dynamics simulation*, John von Neumann Institute for Computing, NIC Series, **23**, 1 (2004).

[37] M. Tuckerman, B. J. Berne and G. J. Martyna, *Reversible multiple time scale molecular dynamics*, J. Chem. Phys. **97**, 1990 (1992).

[38] W. C. Swope, H. C. Andersen, P. H. Berens and K. R. Wilson, *A computer simulation method for the calculation of equilibrium constants for the formation of physical clusters of molecules: Application to small water clusters*, J. Chem. Phys. **76**, 637 (1982).

[39] P. Hoogerbrugge and J. M. V. A. Koelman, *Simulating microscopic hydrodynamic phenomena with Dissipative Particle Dynamics*, Europhys. Lett. **19**, 155 (1992).

[40] P. Español and P. Warren, *Statistical Mechanics of Dissipative Particle Dynamics*, Europhys. Lett. **30**, 191 (1995).

[41] E. A. J. F. Peters, *Elimination of time step effects in DPD*, Europhys. Lett. **66**, 311 (2004).

[42] C. Pastorino, T. Kreer, M. Müller and K. Binder, *Comparison of Dissipative Particle Dynamics and Langevin thermostats for out-of-equilibrium simulations of polymeric systems*, Phys. Rev. E **76**, 026706 (2007).

[43] J. Zausch, J. Horbach, M. Laurati, S. U. Egelhaaf, J. M. Brader, Th. Voigtmann and M. Fuchs, *From equilibrium to steady state: the transient dynamics of colloidal liquids under shear*, J. Phys.: Condens. Matter **20**, 404210 (2008).

[44] J. Zausch and J. Horbach, *The build-up and relaxation of stresses in a glass-forming soft-sphere mixture under shear: A computer simulation study*, Europhys. Lett. **88**, 60001 (2009).

[45] H. C. Andersen, *Molecular dynamics simulations at constant pressure and/or temperature*, J. Chem. Phys. **72**, 2384 (1980).

[46] E. Donth, *The Glass Transition: Relaxation Dynamics in Liquids and Disordered Materials*, (Springer, Berlin, 2001).

[47] H. Vogel, Phys. Z. **22**, 645 (1921).

[48] G. S. Fulcher, *Analysis of recent measurements of the viscosity of glasses*, J. Amer. Ceram. Soc. **8**, 339 (1925).

[49] G. Tammann and W. Z. Hesse, *Die Abhängigkeit der Viscosität von der Temperatur bei unterkühlten Flüssigkeiten*, Anorg. Allg. Chem. **156**, 245 (1926).

[50] C. A. Angell, P. H. Poole and J. Shao, *Glass-forming liquids, anomalous liquids, and polyamorphism in liquids and biopolymers*, Il Nuovo Cimento D **16**, 993 (1994).

[51] R. Kohlrausch, *Ueber das Dellmann'sche Elektrometer*, Ann. Phys. (Leipzig) **11** 393 (1847).

[52] G. Williams and D. C. Watts, *Non-symmetrical dielectric relaxation behaviour arising from a simple empirical decay function*, Trans. Faraday Soc. **66**, 80 (1970).

[53] M. Fuchs and M. E. Cates, *A mode coupling theory for Brownian particles in homogeneous steady shear flow*, J. Rheol. **53**, 957 (2009).

[54] I. Gazuz, A. M. Puertas, T. Voigtmann and M. Fuchs, *Active and nonlinear microrheology in dense colloidal suspensions*, Phys. Rev. Lett. **102**, 248302 (2009).

[55] I. Gazuz, Dissertation: *Active and passive particle transport in dense colloidal suspensions*, http://nbn-resolving.de/urn:nbn:de:bsz:352-opus-66299 Konstanz (2008).

[56] M. V. Gnann, I. Gazuz, A. M. Puertas, M. Fuchs and T. Voigtmann, *Schematic models for active nonlinear microrheology*, Soft Matter **7**, 1390 (2011).

[57] M. V. Gnann, Diplomarbeit: *Analysis of schematic models of mode-coupling theory for colloids in external fields*, Konstanz (2009).

[58] J. P. Bouchaud, A. Comtet, A. Georges and P. Le Doussal, *Classical diffusion of a particle in a one- dimensional random force field*, Ann. Phys. **201**, 285 (1990).

[59] J. P. Bouchaud and A. Georges, *Anomalous diffusion in disordered media: Statistical mechanisms, models and physical applications*, Phys. Rep. **195**, 127 (1990).

[60] Y. G. Sinai *The limiting behavior of a one-dimensional random walk in a random medium*, Theory Probab. Appl. **27**, 256 (1983).

[61] J. P. Hansen and I. R. McDonald, *Theory of simple liquids*, (Academic Press, London, 2005).

[62] F. Penna, J. Dzubiella and P. Tarazona, *Dynamic density functional study of a driven colloidal particle in polymer solutions*, Phys. Rev. E **68**, 061407 (2003).

[63] C. Harrer, D. Winter, J. Horbach, M. Fuchs and T. Voigtmann, *Force-induced diffusion in microrheology*, J. Phys.: Condens. Matter **24** (2012).

[64] A. Einstein, *Über die von der molekularkinetischen Theorie der Wärme geforderte Bewegung von in ruhenden Flüssigkeiten suspendierten Teilchen*, Annalen der Physik **322**, 549 (1905).

[65] I. Santamaria-Holek and A. Pérez-Madrid, *Mean-field "temperature" in far from equilibrium systems*, J. Phys. Chem. B **115**, 9439 (2011).

[66] K. Vollmayr-Lee, *Single particle jumps in a binary Lennard-Jones system below the glass transition*, J. Chem. Phys. **121**, 4781 (2004).

[67] J. Horbach, T. Voigtmann, F. Höfling and T. Franosch, *Localization phenomena in models of ion-conducting glass formers*, Eur. Phys. J. ST **189**, 141 (2010).

[68] R. L. Jack, D. Kelsey, J. P. Garrahan and D. Chandler, *Negative differential mobility of weakly driven particles in models of glass formers*, Phys. Rev. E **78**, 011506 (2008).

[69] M. B. Hastings, C. J. Olson Reichhardt and C. Reichhardt, *Depinning by fracture in a glassy background*, Phys. Rev. Lett. **90**, 098302 (2003).

[70] C. Reichhardt and C. J. Olson Reichhardt, *Directional locking effects and dynamics for particles driven through a colloidal lattice*, Phys. Rev. E **69**, 041405 (2004).

[71] A. Fiege, M. Grob and A. Zippelius, *Dynamics of an intruder in dense granular fluids*, Granular Matter **14**, 247 (2012).

[72] J. Horbach and W. Kob, *Relaxation dynamics of a viscous silica melt: The intermediate scattering functions*, Phys. Rev. E **64**, 041503 (2001).

[73] H. H. Wensink and H. Löwen, *Rhythmic cluster generation in strongly driven colloidal dispersions*, Phys. Rev. Lett. **97**, 038303 (2006).

[74] J. Zinn-Justin, *Precise determination of critical exponents and equation of state by field theory methods*, Phys. Rep. **344**, 159 (2001).

[75] K. Binder and E. Luijten, *Monte Carlo tests of renormalization-group predictions for critical phenomena in Ising models*, Phys. Rep. **344**, 179 (2001).

[76] M. E. Fisher, *The theory of equilibrium critical phenomena*, Rep. Prog. Phys. **30**, 615 (1967).

[77] M. E. Fisher, in *Critical phenomena*, edited by M. S. Green, (Academic Press, London, 1971).

[78] S. Katz, J. L. Lebowitz and H. Spohn, *Phase transitions in stationary nonequilibrium states of model lattice systems*, Phys. Rev. B **28**, 1655 (1983).

[79] K. T. Leung, *Finite-size scaling of driven diffusive systems: Theory and Monte Carlo studies*, Phys. Rev. Lett. **66**, 453 (1991).

[80] G. Gonnella and M. Pellicoro, *Critical temperatures in driven binary mixtures with conserved and non-conserved dynamics*, J. Phys. A: Math. Gen. **33**, 7043 (2000).

[81] D. Beysens, M. Gbadamassi and L. Boyer, *Light-scattering study of a critical mixture with shear flow*, Phys. Rev. Lett. **43**, 1253 (1979).

[82] D. Beysens and M. Gbadamassi, *Shear-induced effects on critical concentration fluctuations*, Phys. Rev. A **22**, 2250 (1980).

[83] L. Onsager, *Crystal statistics. I. A two-dimensional model with an order-disorder transition*, Phys. Rev. **65**, 117 (1944).

[84] A. W. Lees and S. F. Edwards, *The computer study of transport processes under extreme conditions*, J. Phys. C **5**, 1921 (1972).

[85] N. Metropolis, A. W. Rosenbluth, M. N. Rosenbluth, A. H. Teller and E. Teller, *Equation of state calculations by fast computing machines*, J. Chem. Phys. **21**, 1087 (1953).

[86] S. Kirkpatrick and E. Stoll, *A very fast shift-register sequence random number generator*, J. Comp. Phys. **40**, 517 (1981).

[87] R. J. Glauber, *Time-dependent statistics of the Ising model*, J. Math. Phys. **4**, 294 (1963).

[88] D. Kadau, A. Hucht and D. E. Wolf, *Magnetic friction in Ising spin systems*, Phys. Rev. Lett. **101**, 137205 (2008).

[89] R. J. Allen, C. Valeriani, S. T. Nicola, P. R. T. Wolde and D. Frenkel, *Homogeneous nucleation under shear in a two-dimensional Ising model: Cluster growth, coalescence, and breakup*, J. Chem. Phys. **129**, 134704 (2008).

[90] M. C. Tringides, I. Kwon, C. M. Soukoulis and G. S. Grest, *Structure factor of the random field Ising model*, J. Phys. Colloques **49**, C8-1215 (1988).

[91] K. Binder and J. S. Wang, *Finite-size effects at critical points with anisotropic correlations: Phenomenological scaling theory and Monte Carlo simulations*, J. Stat. Phys. **55**, 87 (1989).

[92] J. S. Wang, *Anisotropic Finite-size scaling analysis of a two-dimensional driven diffusive system*, J. Stat. Phys. **82**, 1409 (1996).

[93] A. M. Ferrenberg and R. H. Swendsen, *Optimized Monte Carlo data analysis*, Phys. Rev. Lett. **63**, 1195 (1989).

[94] D. Chandler, *Introduction to modern statistical mechanics*, (Oxford University Press, New York, 1987).

[95] K. Binder, *Finite size scaling analysis of ising model block distribution functions*, Z. Phys. B **43**, 119 (1981).

[96] A. Hucht, *Nonequilibrium phase transition in an exactly solvable driven Ising model with friction*, Phys. Rev. E, **80**, 061138 (2009).

[97] A. Hucht, *Strongly anisotropic nonequilibrium phase transition in Ising models with friction*, Phys. Rev. E **85**, 051120 (2012).

[98] D. P. Landau, *Finite-size behavior of the Ising square lattice*, Phys. Rev. B **13**, 2997 (1976).

[99] J. D. Weeks, D. Chandler and H. C. Andersen, *Role of repulsive forces in determining the equilibrium structure of simple liquids*, J. Chem. Phys. **54**, 5237 (1971).